Université d'Ottawa · University of Ottawa

Université d'Ottawa · University of Ottawa

FACULTÉ DE ÉTUDES SUPÉRIEURES ET POSTDOCTORALES

FACULTY OF GRADUATE AND POSTDOCTORAL STUDIES

Sylvain HUBERT

AUTEUR DE LA THÈSE - AUTHOR OF THESIS

Ph.D. (Physics)

GRADE - DEGREE

Department of Physics

FACULTÉ, ÉCOLE, DÉPARTEMENT - FACULTY, SCHOOL, DEPARTMENT

TITRE DE LA THÈSE - TITLE OF THE THESIS

Theoretical Study of Polymers : Flow-Induced Deformation in Nanochannels and Reptation Dynamics in Heterogeneous Gels

G. Slater

DIRECTEUR DE LA THÈSE - THESIS SUPERVISOR

CO-DIRECTEUR DE LA THÈSE - THESIS CO-SUPERVISOR

EXAMINATEURS DE LA THÈSE - THESIS EXAMINERS

B. Joos

P. Kalyniak

I. L'Heureux

A-C. Shi

J.-M. De Koninck, Ph.D.

LE DOYEN DE LA FACULTÉ DES ÉTUDES SUPÉRIEURES ET POSTDOCTORALES

DEAN OF THE FACULTY OF GRADUATE AND POSTDOCTORAL STUDIES

Theoretical Study of Polymers: Flow-Induced Deformation in Nanochannels and Reptation Dynamics in Heterogeneous Gels

by

Sylvain Hubert

A thesis presented to the University of Ottawa
in fulfilment of the thesis requirement for the degree of
Doctorate of Science in Physics

Ottawa, Ontario
May 11, 2004

Your file Votre référence
ISBN: 0-494-01711-2
Our file Notre référence
ISBN: 0-494-01711-2

Acknowledgments

I would like to give special thanks to my supervisor, Dr. Gary Slater, for introducing me to the physics of polymers in the summer of 1993 while I was an undergraduate student at the University of Ottawa. His guidance and his understanding have always been a great source of inspiration. I also appreciate the great amount of time he spent helping me during all those years.

I would like to give my sincere gratitude to Dr. Ivan L'Heureux, Dr. Benoit Dionne and Dr. Yves Bourgault for all those delightful discussion and for helping me with my thesis.

Thanks to my family: Jean-Claude, Miriam, Manon, Chantal, Stéphane and Mario for always believing in me and giving me their support. Thanks to my friends and colleagues: Céline Paquet, Fabrice Rapold, Vincent Allain, Ros Salvador, Grant I. Nixon, Frédéric Tessier, Martin Kenward, Jean-François Mercier for always been there when I needed them. I also thank FCAR, NSERC and the University of Ottawa for their scholarships and for offering me a chance to pursue my studies in polymer physics.

Finally, I would like to give my deepest thanks to my wife Jessica and my son Gabriel for their endless support, patience and love.

Sommaire

En 1992, B. Smith, L. Finzi et C. Bustamante furent les premiers à directement observer le comportement d'une molécule d'ADN à l'aide de la vidéo microscopie de fluorescence. Leurs résultats ont permis d'améliorer notre compréhension des propriétés statiques et dynamiques d'une chaîne (polymère) isolée qui représentent la base de la physique des polymères. Plusieurs modèles théoriques et résultats expérimentaux ont suivi le travail effectué par Smith et al. Ces théories utilisent plusieurs techniques d'analyse afin d'étudier les polymères: analyse thermodynamique, théorie des champs, lois d'échelle, théorie du groupe de renormalisation et simulations par ordinateur. Au chapitre 2, nous présentons une étude de la dynamique moléculaire d'un polymère attaché et tiré à vitesse constante à l'intérieur de nanotubes. Nos résultats sont comparés aux prédictions théoriques et aux résultats expérimentaux courants.

Nous pouvons également se poser des questions sur le comportement des polymères en solutions diluées ou même en solutions concentrées tel qu'un gel où les intéractions entre les polymères deviennent importantes. Par exemple, l'électrophorèse en gel (EG) est devenu un outil analytique populaire en biologie. Depuis son introduction en 1937, la biologie moléculaire a grandie substantiellement. L'EG est maintenant une excellente méthode de séparation de molécules d'ADN car en solution libre, la mobilité électrophorétique de l'ADN est indépendente de sa masse. À cause de cela, la plupart des dévelopements théoriques ont eu pour but l'amélioration des procédures de séparation de la molécule d'ADN.

En 1993, Zimm et Lumpkin ont proposé un nouveau modèle de reptation afin d'expliquer l'électrophorèse dans un gel irrégulier. Suivant le travail de Zimm et Lumpkin, nous suggérons au chapitre 3 un modèle plus détaillé de ce problème où les effets connus de mémoire dans la théorie standard de la reptation sont pris en considération. Nos résultats sont en accord qualitatif avec les résultats expérimentaux disponibles et en désaccord avec ceux prédit par Zimm et Lumpkin.

Au chapitre 4, nous examinons la reptation dans un milieu où les intéractions énergétiques sont aléatoires, statiques et corrélées sur une distance λ, basé sur l'agorithme développé au chapitre 3. Nos résultats diffèrent de ceux obtenus au chapitre 3 et sont également comparés à ceux de Zimm et Lumpkin.

Summary

In 1992, B. Smith, L. Finzi and C. Bustamante were the first to directly observe the behaviour of a single DNA molecule with the help of video fluorescence microscopy. Their results greatly improved our understanding of the static and dynamic properties of a single isolated chain which represents the foundation of polymer physics. A series of experimental results and theoretical models followed the work of Smith et al. Current theoretical approaches to study polymers involve many techniques: thermodynamic analysis, field theory, scaling, renormalization group theory and computer simulations. In Chapter 2, we present a Molecular Dynamics study of the effect of strong lateral confinement on the properties of a tethered polymer pulled at constant velocity. Our results are compared with recent theoretical predictions and experimental results.

One can also ask questions about the behaviour of dilute polymer solutions, or even concentrated solutions such as melts or gels, where the interactions among the polymers are important. For instance, gel electrophoresis (GE) is one of the most common analytical tools used in biology. Since the introduction of GE in 1937, molecular biology has grown substantially. Indeed, GE has shown to be an excellent separation method for DNA molecules since in free solution, the electrophoretic mobility of a DNA molecule is independent of its size. Because of that, most of the theoretical developments in the field have been aimed at improving DNA electrophoretic separation tools.

In 1993, Zimm and Lumpkin proposed a new reptation model to explain gel electrophoresis of polyelectrolytes in irregular matrices. Following this work, we propose in Chapter 3 a more detailed model of this problem where the well-known memory effects of the standard reptation theory are taken into account. Our results are in qualitative agreement with available experimental results and disagree with those of Zimm and Lumpkin.

In Chapter 4, we examine the reptation of a polymer in a static environment with quenched random energies that are correlated over a finite length scale λ based on the algorithm detailed in Chapter 3. The results obtained differ from our previous model (Chapter 3) and are compared with those of Zimm and Lumpkin.

This thesis is dedicated to my wife Jessica and son Gabriel for all those nights that I was not able to spend with them. They have showed me endless support and love.

Contents

List of Figures

List of Tables

Chapter 1 Introduction

The human body is made of a variety of proteins which defend us against viruses, metabolize food, and perform other important structural and metabolic tasks. Their structure is determined by the genetic information contained inside genes, more precisely within very long polymeric strands of deoxyribonucleic acid also called DNA. The DNA inside each human cell can encode about 100,000 distinct genes. This DNA is partitioned into 46 chromosomes, 23 from each parent. The DNA is built up from a set of four nucleotides or bases: adenine (A), cytosine (C), guanine (G) and thymine (T). The sequential arrangement of the bases defines our genetic information. Average human chromosomes contain a hundred million of these nucleotides, whereas the entire human genome is composed of about three billion bases. The goal of the Human Genome Project [1], launched in 1988, is to determine and decode this sequence information. This task is a huge challenge and will lead to many new insights into the functions of genes and proteins. It also raised important ethical issues about how the information will be used.

The DNA molecule is composed of two strands of polymerized nucleotides twisted into a right-handed helix, as discovered by James Watson and Francis Crick in 1953. The two strands complement each other in the sense that instead of having either random or identical sets of nucleotides in the two strands, an A in one strand is always associated with a T on the other strand. Similarly, a C in on strand is always associated with a G in the complementary strand.

Today, even the best technology cannot sequence more that one thousand DNA bases at a time; DNA strands need to be broken into small pieces in order to be sequenced. Once broken and sequenced, the information is put back together to obtain the entire genetic information. The first step is to isolate each chromosome using an instrument called a flow cytometer. The chromosomes are labelled using two different fluorescent dyes which are squeeze between the A-T and C-G bases. The fluorescence of each chromosome allow a

particular chromosome to be isolated.

We have mentioned earlier that chromosomes have one hundred million bases; this is far too large to be sequenced directly by present technologies. The isolated chromosomes still need to be broken into smaller pieces. Since chromosomes are rather fragile, they can be broken up by forcing them through a syringe needle. The shear forces will break the DNA into fragments. The size distribution of the DNA fragments is controlled by adjusting the flow rate and the diameter of the needle. The DNA can be broken down into fragments of about 500-1000 bases.

Each DNA fragment is then replicated to obtain a solution of identical DNA strands. An enzyme is added to the solution to synthesize a complementary strand to each of the strands in solution. These complementary strands continue to grow along the DNA fragment until the replication is stopped by a chain-terminating nucleotide. The result is a population of fragments that are generated, each one beginning with the same primer and ending with a chain-terminating nucleotide. Some fragments are short because they happen to incorporate a terminator soon after growth starts, while others are much longer, and the whole population is called a sequencing ladder. Terminators can be synthesized to be A, T, G or C nucleotides, in order to generate four sequencing ladders. This technique has been developed by Sanger in 1977 [2].

Once the DNA sequencing ladders have been produced, the individual fragments need to be distinguished. Gel electrophoresis is arguably the main technique for the separation of biologically relevant polyelectrolytes. Electrophoresis is simply the movement of charged molecules under the influence of an electric field, and the gel has the effect of separating (or sieving) the molecules according to their size. Small fragments travel through the gel more quickly than large ones. Note that a sieving polymer matrix is normally needed to obtain size separation of polyelectolytes such as DNA. Indeed, the mobility of DNA fragments is generally size independent in free solution. In this situation, one cannot simply consider the total electric force acting on the monomers (which scales as the length of the polymer) and the friction force retarding the randomly coiled polymer. The effect of the counter-ions has to be taken into account since they produce a flow in the opposite direction which cancels exactly the long-range component of the hydrodynamic forces acting on the polymer. Therefore, the friction coefficient of the polymer will be that of a long rod (which also scales

as the length of the polymer) rather than that of a spherical object (which would be the case for mechanical forces applied to a polymer coil). This explains the well-known size independence of the electrophoretic mobility of uniformly charged polyelectrolytes in free solution (this is often called the "free-draining" property of polyelectrolytes).

Individual fragments are thus separated using a technique called gel electrophoresis. The apparatus can be quite simple, consisting of two glass plates about 40 cm long and 30 cm wide separated by a 200 μm spacer. The gap between the plates is filled with a polyacrylamide or agarose gel, prepared using an aqueous buffer, and the buffer is treated to ensure that DNA remains single stranded. The solution containing the fragments is placed at the top of the gel and an electric field, typically about 50 Vcm^{-1}, is applied across the plate to drive the negatively charged DNA through the gel. Four different fluorescent labels are used, one for each sequencing ladder, which means that a single electrophoresis lane can be used to separate all of the fragments. The identity of each fragment is determined by the fluorescence spectrum of its band, rather than by the presence of a band in a particular lane.

Sequencing the entire human genome requires single base resolution. Because of this, the Human Genome Project has driven the development of a variety of new analytical instruments, methods, and reagents for nucleic acids analysis. One method that is now becoming prominent for DNA sequencing is capillary electrophoresis (CE). CE is an attractive technique for DNA analysis because the capillaries provide high speed and high resolution separations. CE increases the separation efficiency (as compared to standard slab gels) and it is easy to automate gel and sample loading. The use of CE for DNA sequencing was first demonstrated in 1990, when sequencing separation of 350 bases were obtained in cross-linked gels in about 80 minutes [3, 4, 5]. Considerable progress has been made in the past years, and sequencing read-lengths of more than 800 bases can now be obtained in less than 80 minutes using replaceable linear polyacrylamide gels [6].

Remarkably, Barron et al. [7] demonstrated that capillary electrophoresis separation of nucleic acids can also be achieved in unentangled, ultra-dilute polymer solutions of hydroxyethyl cellulose (HEC). DNA fragments up to 23kbp were separated in less than 20 minutes which is an enormous improvement in speed compared with gel electrophoresis. Most of these experiments were performed using uncoated capillaries for two reasons: the

resolution of the separation is superior in uncoated capillaries because the electro-osmotic flow increases the DNA residency time in the capillary, and uncoated capillaries are far less complicated to use. Since no sieving network exists below the polymer overlap concentration c^*, neither the Ogston [8] nor the reptation [9] model can explain the existence of this novel separation process. Indeed, these standard models actually predict no sieving and hence no separation whatsoever for polymer concentrations below c^*. Barron et al. [7] proposed a new transient entanglement coupling separation mechanism based on temporary entanglements between the DNA molecule and the uncharged HEC chains it sometimes drag along during the electrophoretic drift. A theoretical model based on that mechanism was derived later which successfully described the DNA electrophoresis data of Barron et al. for short-chain HEC [10]. However, this quantitative model is not valid for long-chain HEC because it assumed that the DNA and the HEC both remain undeformed during the collisions. Therefore, a complete understanding of the deformation of polyelectrolytes under external forces such as a flow or an electric field is needed to improve the electrophoresis separation of DNA in ultra-dilute polymer solutions.

The study of the deformation of tethered polymers subjected to a flow in nanochannels is presented in the first part of this thesis in order to understand and improve the separation mechanism of DNA molecules or more generally of polyelectrolytes using capillary electrophoresis in ultra-dilute polymer solutions. We will see how the chain deformation affects its drag force using molecular dynamics simulations. The second part of this thesis presents the study of the reptation dynamics of polyelectrolytes in random energy landscapes to provide insight to recent experimental results of DNA slab gel electrophoresis where the electrophoretic mobility and the diffusion coefficient decrease faster than what current theories predict. This will be achieved using the Monte-Carlo algorithm. The study of these two subjects will help us better understand the main mechanisms behind the DNA separation processes of electrophoretic devices and will allow us to improve them.

The two sections below provide a short summary of current theoretical and experimental works related to the above subjects, following by a brief introduction to the thesis.

1.1 Deformation of a Single Polymer in a Flow

Light scattering and birefringence measurements of polymeric solutions have been used to study the dynamics of polymer chains [11, 12, 13, 14, 15]. Although these traditional methods of experimentation have given much insight, they have a natural disadvantage, i.e., the properties of a single chain are calculated indirectly from measurements averaged over a large number of chains. In addition, the polymers used are not always monodisperse. Finally, in most hydrodynamic flow experiments, the measurement time must be short since the particular volume of interest (sample) is rapidly carried away by the flow.

In the last ten years, the ability to observe and study the static and dynamic properties of single polymers has been achieved by many groups. In 1992, Smith et al. [16] measured the elasticity of a DNA molecule using video fluorescence microscopy where the DNA was chemically attached at one end to a glass surface and at the other end to a magnetic bead. Although a DNA molecule cannot be directly manipulated with optical tweezers [17], a micrometer sized bead attached to the end of the DNA can be controlled quite easily. Using optical tweezers, Perkins et al. [18] measured DNA relaxation after single DNA chains were stretched to full extension in a flow.

Note that optical trapping exhibits important experimental limitations such as cumbersome calibration procedures and heating effects at high laser power which can limit the range of applied forces. To overcome these limitations, Wirtz proposed the attachment of a small magnetic bead at the end of a fluorescent labelled DNA pulled by a calibrated magnetic force through a solution of unlabelled DNA chains to monitor the transport coefficients of the chain [19].

Other interesting experimental results include:

- The study of the effect of confinement on the transient extension and relaxation of single DNA molecules as they interact with obstacles in a specially designed thin slit by Bakajin et al. [20].

- The study of the relaxation measurements of a fluorescent DNA chain stretched by a Poiseuille flow in a capillary vessel by Manneville et al. [21].

- The study of the dynamics of a single polymer tethered to a solid surface in a shear

flow [22].

- The study of single polymer stretching using atomic force microscopy [23, 24, 25].

These experimental results helped to develop a better understanding of the fundamental physics behind the deformation of single polymers. Another tool used to study the relaxation and stretching of polymers is computer simulations [26, 27, 28, 29, 30, 31] such as Molecular Dynamics [32, 33, 34].

If forces $\pm f$ are applied to the two ends of a polymer chain, its end-to-end distance h increases. Each segment of the chain tends to orient in the direction of the force like a dipole. The exact solution to this problem for a free-jointed-chain is well-known [35]. For small extensions, the scaled force ($F = fb/k_BT$ where b is the Kuhn length [1], k_B is the Boltzmann constant and T is the temperature) follows the power law $F \sim H$ whereas for large extensions we get $F \sim 1/(1-H)$ where $H = h/h_{max}$ is the scaled chain extension and h_{max} is the maximum extension of the chain or its contour length. In the case of a worm-like chain, the most used force-extension law is the interpolation formula derived by Marko and Siggia [36],

$$F(H) = 2H - \frac{1}{2} + \frac{1}{2(1-H)^2} \cdot \tag{1.1}$$

Other interesting theories have been proposed to explain the stretching of tethered DNA chains in shear flows [37] or the partial draining properties of a tethered polymer in a flow [38]. Brochard-Wyart participated in the development of the scaling theory for the deformation of a tethered chain in strong flows [39].

Industrial applications are numerous and include polymer coating, lubrification, and extrusion. In biology and medicine, the diffusion constant of an individual molecule governs its gel electrophoresis and potential gene-therapy properties. The transport coefficients of an individual bio-molecule dictate its dynamic conformations and also its inter-membrane and transmembrane transport properties. Deformation and diffusion are often two coupled phenomena and one must understand both to get a complete picture.

Chapter 2 gives a detailed Molecular Dynamics study of the fundamental problem of a single tethered polymer pulled at constant velocity inside a nanotube. Our results are

[1] The Kuhn length can roughly be considered as the length scale beyond which all "persistence" or "stiffness" is lost.

compared with current theories and available experimental results. We will see that our simulation results of a tethered freely-jointed chain subjected to a hydrodynamic flow does not follow theoretical prediction. The fact that we recover the correct FJC prediction when both ends of our FJC chains are pulled, and the WLC predictions for both mechanical and hydrodynamic forces, suggests that our FJC results are indeed due to effects that are missing in current theories. A self-consistent model of FJC stretching in a flow is thus needed.

1.2 Gel Electrophoresis

The idea of separating charged particles in solution using electric fields was first proposed by Tiselus in 1937 [40]. Performing the separation in a gel (which is a solution of crosslinked polymers) provided the biology community with an analytical tool for biomolecules [41]. A gel is now commonly used as a separation matrix for electrophoresis of linear polyelectrolytes. We can also use an entangled solution of uncrosslinked polymers as a separation matrix. In this case, we talk about concentrated solutions instead of gels.

We use a gel for the electrophoresis of polyelectrolytes for two main reasons: 1) the rigidity and the density of the gel help reduce the effect of convection and diffusion caused by the electric field, and 2) the gel allows the sieving of several poly-ions that cannot be achieved in free solution. A high number of hydrophilic gels have been employed for gel electrophoresis (GE) [42] but the most popular gels still remain polyacrylamide for relatively small pore sizes ($\sim$ 10 nm) and agarose for larger pore sizes ($\sim$ 100 nm).

Early applications of GE involved small polyelectrolytes such as proteins in their native state. It was then claimed that the ratio of the mobility μ to the free solution mobility μ_0 was given [43] by

$$log(\mu/\mu_0) \sim -cR^2 \tag{1.2}$$

where c is the gel concentration and R is the radius of analyte. Rodbard and Chrambach [44] developed a model to interpret the results based on previous work by Ogston [8] and Morris [45]. Optimal separation is expected in this model when the particle of size R is comparable to the average pore size $\bar{a}$ of the gel. This model has also been applied to

flexible polymers where the polyelectrolyte effective radius R is taken to be the polymer radius of gyration R_g. According to this model, linear polyelectrolytes with a radius of gyration greater than the average pore size should have a mobility that decays very rapidly with R. In fact, the opposite behaviour was found [46, 47, 48, 49, 50, 51].

Lumpkin et al. [52] and Lerman et al. [53] were the first groups to propose a theoretical understanding of the migration process of linear polyelectrolytes inside a gel (when $R_g > \bar{a}$). These authors remarked that the polymers must be threading their way in the gel like a snake in thick grass by a "reptation in a tube" process similar to the model proposed by DeGennes [9] for entangled polymers. The idea of a field-induced orientation of the polymers was then introduced in the "reptation" model by Lumpkin et al. [54]. Slater et al. [55, 56, 57, 58, 59] recognized the problems raised by the use of thermodynamic averages over the chain conformations and provided a numerical solution for the biased reptation master equations.

The biased reptation model (BRM) predicts a mobility μ that decreases as $1/M$ for small polymers or low field intensities and becomes independent of the chain molecular size M for larger polymers or higher field intensities. Slater et al. [56] were able to predict a minimum in the mobility versus size dependence, which was subsequently observed experimentally [60].

Presently, agarose gel electrophoresis of DNA fragments ranging from 2 to 40 kbp requires 1-4 hours of separation time. The upper limit of slab gel electrophoresis is about 40 kbp for DNA molecules. This limit can be increased if one uses pulsed fields instead of a steady fields. Typical separation times in pulsed-field gel electrophoresis (PFGE) is 12-48 hours for molecules up to about 5000 kbp. Separation beyond this size has yet to be achieved.

There is still the problem of the existing heterogeneity of the gel. It is impossible to prepare a gel solution where all pores are energetically equivalent. Zimm and Lumpkin [61] were the first to propose a theoretical model of electrophoresis of polyelectrolytes inside an irregular matrix following the experimental results of Calladine, Collis, Drew and Mott [62]. These results differ from those predicted by the standard approaches such as the Ogston and the biased-reptation models. Chapter 3 gives a brief description of the new approach used by Zimm and Lumpkin as well as our new model. We will see our how the dynamic

properties of polyelectrolytes are modified inside random energy landscapes.

1.3 Presentation of the Thesis

The work presented in this thesis describes and uses two new computer simulation algorithms to study (i) the deformation of a single tethered polymer subjected to a flow in a nanochannel and (ii) the reptation dynamics of polyelectrolytes in random energy landscapes (annealed and quenched). The first algorithm is based on Molecular Dynamics while the second is based on Monte Carlo methods.

In Chapter 2, we will derive and describe the Molecular Dynamics algorithm that we will use to study the deformation of a tethered polymer pulled at constant velocity in nanochannels. A brief review of the current theoretical background regarding polymer deformations will also be provided and compared with our simulation results. This Chapter will further discuss the effects of confinement on polymer dynamics and the predictions obtained by other groups.

Chapter 3 will introduce our new modified biased-reptation model to study the reptation dynamics of polyelectrolytes in annealed energy landscapes. The reptation dynamics of polyelectrolytes in quenched energy landscapes with long range correlations will discuss in Chapter 4. We will examine the zero-field limit ($\epsilon = 0$) as well as reptation in the presence of an electric field ($\epsilon > 0$). The general conclusion of this thesis is found in Chapter 5. Appendix A provides a list of notations (symbols) used throughout this thesis with a short description.

Chapter 2 Deformation of Tethered Polymers: A Study using Molecular Dynamics Simulations

2.1 Introduction

In recent years, scientists have been able to directly observe the behaviour of single polymer molecules in dilute solutions with the help of video-microscopy. For instance, the extension and relaxation of DNA chains in a flow were measured using optical tweezers [18, 21, 63], magnetic fields [19] or Poiseuille flows [21] (inside capillaries). Furthermore, the "trumpet" and "stem and flower" regimes described by Brochard-Wyart [39, 64] were directly observed by pulling a small magnetic bead attached at one end of a DNA chain in a solution of unlabelled DNAs (see Figure 2.1). The effect of confinement on the dynamic and static properties of DNA during electrophoresis was studied by Bakajin et al [20]. These authors showed that the characteristics of the polymer were modified when it was confined in a thin slit between planar surfaces (with distances as small as $0.09\mu m$) and suggested that it was a consequence of various hydrodynamic screening effects.

Consequently, many experiments have been performed on single polymer chains to try to understand their behaviour and characteristics under flow. It is important that a good theoretical background be developed. Such knowledge would help us to understand the dynamics of a polymer molecule entangled around an obstacle or under confinement; this is required to optimize and improve the performance of the separation process exploited by capillary DNA electrophoresis in ultra dilute polymer solutions where the main mechanism is based on temporary polymer entanglements. End-Labeled Free-Solution Electrophoresis (ELFSE), electro-hydrodynamic stretching of DNA in confined environments or sequencing in nanofabricated arrays are other examples that would also benefit from such a theoretical background.

Numerical algorithms such as Brownian Dynamics and Monte-Carlo have been developed to explain the complex behaviour of polymers submitted to a flow or uniaxial tension

[38, 65, 66, 67]. These numerical methods either do not take hydrodynamics interactions into account at all, or use the Oseen tensor [120] or Stoke's law [68] to approximate the hydrodynamics interactions. In such approximations, the momentum transport through the solvent is not modelled properly. Nonetheless, these studies provide useful information on the relaxation and the extension of neutral and charged polymer chains. Although published theoretical results seem to adequately describe the experimental data of Perkins et al. [63], current theories do not take into account excluded volume or confinement effects.

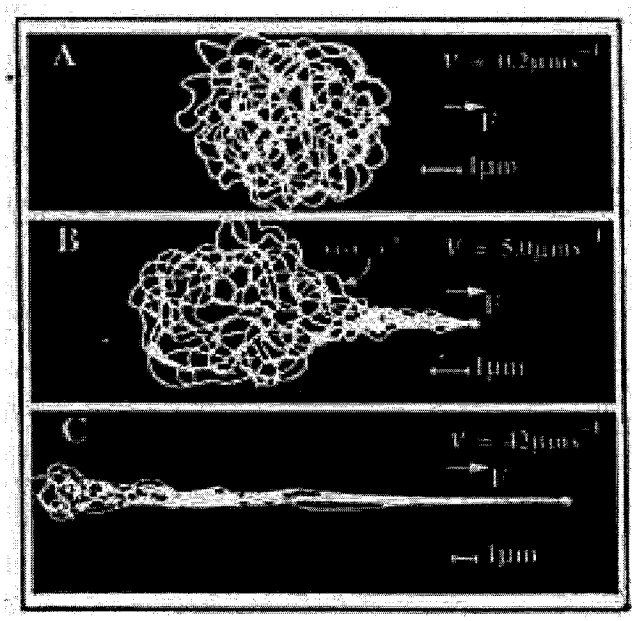

Figure 2.1: DNA chains pulled by one end by a magnetic bead at different velocities. (a) At low velocity, the chain stays unperturbed. (b) At intermediate velocity, the chain extends into a trumpet shape. (c) At higher velocity, the trumpet disappears and the chain stretches into a sticklike (or stem-and-flower) shape. Reproduced from ref. [19]

Recently, Cheon et al. [34] have investigated the stretching of a polymer in a uniform flow using Molecular Dynamics (MD) simulations [69, 70, 71, 72, 73, 74]. In spite of the short length of the polymers simulated, their results agree with the qualitative features of recent DNA experiments and the predictions of the theory of wormlike chains (WLC).

Using extensive Molecular Dynamics simulations, we have studied the properties of a tethered polymer pulled at constant velocity inside a tube (with a square cross-section).

Consequently, we reproduce the main properties of a laminar and non-Poiseuille flow by pulling the tethered polymer. If the flow were generated by adding a constant force to the solvent particles, we would have obtained a Poiseuille-like flow due to the non-slip boundary conditions at the walls of the tube [76]. On the other hand, one can reproduce such a non-Poiseuille flow *in vivo* by using a tethered polyelectrolyte in an electric field or with optical tweezers. The hydrodynamic interactions are implicitly taken into account by simulating all of the solvent particles. Furthermore, by varying the inner diameter of the tube or the length of the polymer, we are able to measure the effect of strong confinement on the polymer chain. Based on the algorithm described below, this chapter shows that Molecular Dynamics is of great help in studying and understanding such polymer behaviour.

2.2 Molecular Dynamics

Molecular Dynamics simulations generate a numerical solution of Newton's equations of motion for a set of interacting particles. The Hamiltonian function $\mathcal{H}(\mathbf{r},\mathbf{p})$ for a system of N particles is defined in terms of the kinetic ($\mathcal{K}$) and potential ($\mathcal{U}$) energies and of the generalized coordinates $\mathbf{r}$ and momenta $\mathbf{p}$:

$$\mathcal{H}(\mathbf{r},\mathbf{p}) = \mathcal{K}(\mathbf{p}) + \mathcal{U}(\mathbf{r}), \tag{2.1}$$

Usually, the kinetic energy $\mathcal{K}$ takes the form

$$\mathcal{K} = \sum_{i=1}^{N} \sum_{\alpha} \mathbf{p}_{i\alpha}^2 / 2m_i \tag{2.2}$$

where m_i is the mass, p_i is the particle momentum and the index α is for the different (x,y,z) components of the momentum of particle i. The potential energy may be divided into terms that depend on the coordinates of individual particles, pairs, triplets etc.

$$\mathcal{U} = \sum_{i} u(\mathbf{r}_i) + \sum_{i} \sum_{j>i} u(\mathbf{r}_i,\mathbf{r}_j) + \sum_{i} \sum_{j>i} \sum_{k>j} u(\mathbf{r}_i,\mathbf{r}_j,\mathbf{r}_k) + \ldots \tag{2.3}$$

The first term represents the effect of an external field. The second term, the pair potential, is generally the most important one. The remaining terms are assumed to be small in comparison to $u(\mathbf{r}_i)$ and $u(\mathbf{r}_i,\mathbf{r}_j)$ and are rarely included in computer simulations.

If we consider a system of particles, with Cartesian coordinates $\mathbf{r}_i$, Eq. 2.1 and Hamilton's equations of motion lead to

$$m_i \ddot{\mathbf{r}}_i = -\nabla_{\mathbf{r}_i} \mathcal{U} = \mathbf{f}_i \tag{2.4}$$

where $\mathbf{f}_i$ is the total force on particle i. The most widely used method for the integration of the equations of motion is the one adopted by Verlet [75] and attributed to Störmer [77]. This method provides a direct solution of the second-order differential equation 2.4. The method is based on positions $\mathbf{r}(t)$, accelerations $\mathbf{a}(t)$, and the positions $\mathbf{r}(t-\delta t)$ from the previous integration step:

$$\mathbf{r}(t+\delta t) = 2\mathbf{r}(t) - \mathbf{r}(t-\delta t) + \delta t^2 \mathbf{a}(t) \ . \tag{2.5}$$

Note that the velocities are not needed to compute the trajectories of particles (they have been eliminated by summing equations obtained through a set of Taylor expansions). The velocities $\mathbf{v}$ are still needed to estimate the kinetic energy and the system total energy and are calculated using the following equation:

$$\mathbf{v}(t) = \frac{\mathbf{r}(t+\delta t) - \mathbf{r}(t-\delta t)}{2\delta t} \ . \tag{2.6}$$

The positions given by Eq. 2.5 are subject to errors of order δt^4 while the velocities are subject to errors of order δt^2. The algorithm is reversible in time and is guaranteed to conserve linear momentum with conservative forces. This method has also been shown to have excellent energy-conserving properties even with relatively long time steps [72].

Modified Verlet schemes have been proposed to tackle the issue of some velocity deficiencies [78, 79, 80]. The 'velocity Verlet' algorithm, proposed by Swope et al [80], minimizes round-off errors and stores positions, velocities, and accelerations at time t to solve the equations of motion:

$$\mathbf{r}(t+\delta t) = \mathbf{r}(t) + \delta t \ \mathbf{v}(t) + \frac{1}{2}\delta t^2 \mathbf{a}(t) \tag{2.7}$$

$$\mathbf{v}(t+\delta t) = \mathbf{v}(t) + \frac{1}{2}\delta t[\mathbf{a}(t) + \mathbf{a}(t+\delta t)] \tag{2.8}$$

The algorithm works as follow: Firstly, the new positions at time $t+\delta t$ are calculated using Eq. 2.7. The velocities at mid-step are computed using

$$\mathbf{v}(t+1/2\delta t) = \mathbf{v}(t) + \frac{1}{2}\delta t \ \mathbf{a}(t) \tag{2.9}$$

The forces and accelerations at time $t+\delta t$ are then computed, and the velocity calculation is completed using

$$\mathbf{v}(t+\delta t) = \mathbf{v}(t+\frac{1}{2}\delta t) + \frac{1}{2}\delta t\ \mathbf{a}(t+\delta t) \tag{2.10}$$

The above equation is identical to Eq. 2.8. At this point the kinetic energy and the potential energy at time $t+\delta t$ are available. The potential energy will have been evaluated in the force calculation.

In MD, the Lennard-Jones 12-6 potential provides a useful approximation of the potential energy between two particles [81, 82, 83, 84] for computer simulations:

$$U_{lj}(r) = 4\varepsilon((\sigma/r)^{12} - (\sigma/r)^{6}) \tag{2.11}$$

where r is the distance between the two particles. The parameters ε and σ provide the scaling for energies and distances. This potential has a long tail of the form $1/r^6$, a negative well of depth ε at $r = 2^{1/6}\sigma$, and a steeply rising repulsive wall at distances less than $r \cong \sigma$. For liquid argon, $\varepsilon/k_B \approx 120K$ and $\sigma \approx 0.34nm$ [72].

When calculating the total potential energy and force for a specific particle (using Eq. 2.11 for our potential interactions), we note that the largest contribution comes from those particles closest to the particle of interest. Therefore, applying a spherical cutoff means a substantial saving in computer time. MD simulations (of liquids) often use a purely repulsive 'modified' Lennard-Jones potential [85], i.e., the long range interactions of the potential is removed with a cutoff at $r_c = 2^{1/6}\sigma$. This value corresponds to the minimum of the Lennard-Jones potential. The value of r_c controls the number of interacting neighbours of a given particle, and the time needed to search for these and evaluate their force contribution. A small value means fewer interactions and a faster computation. The resulting truncated and shifted potential is:

$$U_{tlj}(r) = \begin{cases} 4\varepsilon\left(\left(\frac{\sigma}{r}\right)^{12} - \left(\frac{\sigma}{r}\right)^{6} + \frac{1}{4}\right) & \text{for } r < 2^{1/6}\sigma \\ 0 & \text{for } r \geq 2^{1/6}\sigma\ . \end{cases} \tag{2.12}$$

This function is continuous for $U_{tlj}(r_c)$ and $\nabla U_{tlj}(r_c)$ (see Figure 2.2). Note that the solvent mainly exists to transport momentum in our simulations, i.e., we need particles with a short-range strong repulsive interaction. The attractive tail may be included, but is not necessary. For the case where $r_c > 2^{1/6}\sigma$ (an attractive tail is included), the particles

tend to stay closer to each other which increases the viscosity of the solution. We expect our results to be qualitatively the same with and without an attractive tail for the simulation parameters used in this Chapter.

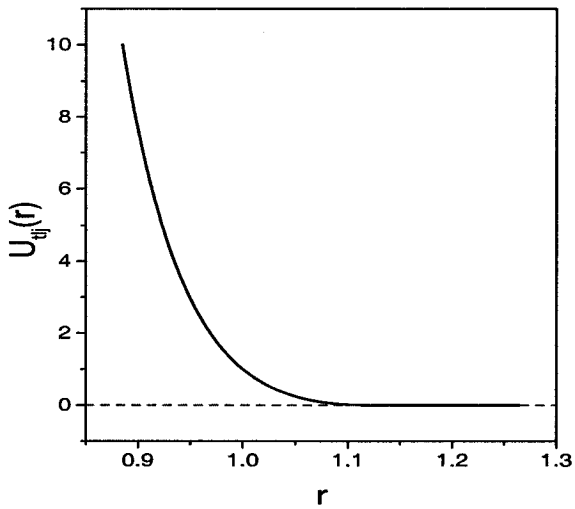

Figure 2.2: The truncated Lennard-Jones potential.

The cell index method [86, 87] is normally used to keep track of particles during the MD simulations. The cubic simulation box is divided into n smaller cubic cells of size L_c greater than the cutoff distance r_c of the potential. There are usually only a few particles per cell. To calculate the forces among the particles, the following steps are performed:

1. We choose a cell in the simulation box.
2. We first calculate the forces among the particles within the chosen cell.
3. We then calculate the forces between the particles of the chosen cell and those of the neighbouring cells.

These steps are repeated for all cells in the simulation box. Using the cell index method only requires to compute $13.5NN_c$ interactions for a three dimensional system, $N_c = N/n$ being the average number of particles per cell and N the total number of particles in the

simulation, compared to the traditional N^2 calculations to obtain the force and potential for each particle. The pre-factor comes from the fact that each cell has 26 neighbours (for a three-dimensional system) plus itself and that the force between cell A and cell B is the same as the force between cell B and cell A (27 divided by 2). Using the cell index method means another substantial saving of simulation time.

The first part of the method consists of sorting all particles into their appropriate cells. This process is fast and may be performed at every time step. During the sorting process, two arrays are created, HEAD and LIST. The first array, HEAD, contains one element for each cell, that is, the identification number of one of the particles sorted into that particular cell. This number also refers to an element in the second array, LIST. That element in the LIST array contains the number of the next particle in that cell, and so on. Eventually, we will reach an element which will be zero. This indicates that there are no more particles in that cell, and we move on to the next element of the HEAD array for the next cell. To illustrate this, imagine a simulation of 5 particles in two cells. Particles 3 and 4 in cell one and 5, 2 and 1 in cell two. The HEAD and LIST arrays look like:

position:	1	2	3	4	5
HEAD:	4	5			
LIST:	0	1	0	3	2

Table 2.1: Cell index example.

One of the major obstacles that MD is facing is the large fraction of particles that lie on the surface of the system; e.g., for a system of 1000 particles arranged in a 10x10x10 cube, about 488 particles appear on the cube faces. The problem of surface effects has been overcome (to some extent) by implementing periodic boundary conditions [88]. In this approach, the system (cubic box) is replicated throughout space to form an infinite lattice. In the course of the simulation, as a particle moves out of the system, the same particle re-enters the system through the opposite face. For a fluid of Lennard-Jones particles, it should be possible to perform a simulation in a cubic box of side as small as $L \approx 6\sigma$, without a particle being able to directly feel the symmetry of the periodic lattice.

For a micro-canonical ensemble (fixed energy, volume and number of particles), MD simulations are usually weakly coupled to a heat bath to keep the temperature from drifting due to numerical roundoff errors. A simple method for fixing the kinetic temperature of a

system in MD is to rescale the magnitude of the velocities at a specific interval by a factor of $(T/\mathcal{T})^{1/2}$ where T is the desired thermodynamic temperature and $\mathcal{T}$ is the current kinetic temperature. For a constant temperature system, the Nosé-Hoover thermostat [89, 90] is often used in MD. In this procedure, each particles is coupled to a heat bath, where the friction coefficient is adjusted to drive the temperature to the desired value.

MD simulations have also been used to study the static and dynamic properties of polymers. The potential between two consecutive monomers is a combination of a purely repulsive potential (Eq. 2.12) and a purely attractive potential (FENE) [91]

$$U_F(r) = -\frac{k_F}{2} R_F^2 \, \ell n \left(1 - \frac{r^2}{R_F^2}\right) \tag{2.13}$$

where k_F is a constant, R_F is the maximum extension of the link and r is the length of the link. Note that without any additional potentials, the polymer is modelled as a freely jointed chain (FJC). Figure 2.3 shows a schematic representation of the potential energies involved between monomers and solvent particles.

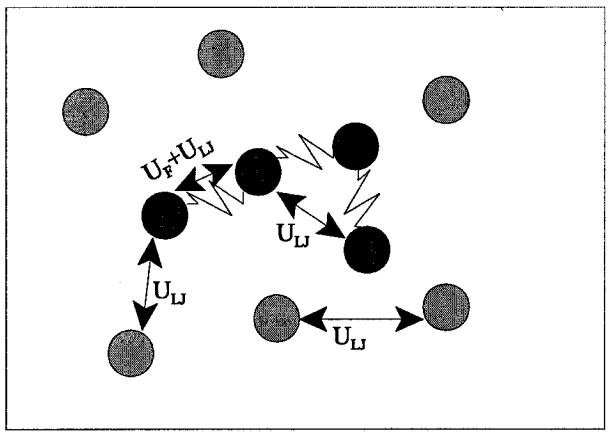

Figure 2.3: Schematic representation of the various potentials involved. The light circles represent the solvent particle whereas the dark circles represent the monomers.

2.3 Methodology of the Simulation

The following section describes the algorithm used for our computer simulations of a tethered polymer under constant solvent flow and strong lateral confinement. The model di-

rectly includes the hydrodynamic interactions between the polymer segments as well as the excluded-volume interactions. There is no need for an approximation like the Oseen tensor.

All particles in our system (including the monomers) are identical in size and interact with each other via the purely repulsive truncated Lennard-Jones potential, Eq. 2.12. Apart from simplifying the simulation program, this feature removes the effect of the theta transition in which the solvent becomes poor and the polymer collapses. The solvent obtained is ideally good. The polymer chain studied in this simulation is modelled as beads connected by stiff springs which is a combination of the Lennard-Jones potential and the finitely extensible nonlinear elastic (FENE) potential 2.13. For all simulations, we used $R_F = 1.5\sigma$ and $k_F = 30\varepsilon/\sigma^2$. The values of k_F and R_F were chosen so that the maximum extension of the chain bond was always less than 1.2σ for the chosen conditions, making bond crossing impossible. However, k_F was also small enough so that we could use an integration time step Δt comparable to what one would use for a fluid of Lennard-Jones particles. Increasing k_F would reduce the maximum extension further but would require a reduction in Δt. Note that our polymer is thus modelled as a freely jointed chain with excluded volume effects in a good solvent since there is no special interaction between our polymer and the solvent.

When using a combination of the Lennard-Jones and FENE potentials for a polymer under a flow, we notice an average fluctuation in the bond length of approximately 3% during the course of the simulation. The combination of two Lennard-Jones 12-6 potentials to model the interaction between two consecutive monomers has been used by Radzyner et al. [32] in order to increase the rigidity of the bond at the expense of a larger Δt.

The flexibility of the chain can also be changed by introducing a bending potential to compare with the worm-like chain (WLC) model,

$$U_{wlc} = k_{wlc}\ cos\ \theta \tag{2.14}$$

where k_{wlc} is the strength of the interaction and θ is the angle between two consecutive links. We used a value of $k_{wlc} = 10.0\varepsilon$ to simulate stiff polymers when needed.

The systems are simulated at a number density of $\rho = 0.85\sigma^{-3}$ and a temperature of $T = 1.0\varepsilon/k_B$. Such a combination is selected to obtain a dense system while keeping it above the glass transition [69].

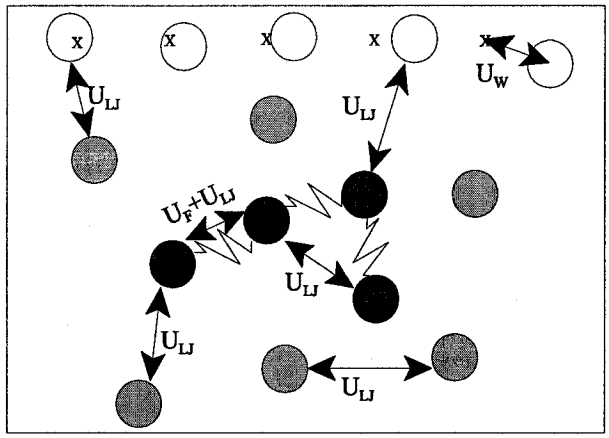

Figure 2.4: Schematic representation of the various potentials involved for a simulation with walls. The light grey circles represent the solvent particle, the dark grey circles the monomers, the white circles the wall particles and the 'x' symbol the fcc lattice position.

The simulations used the "velocity Verlet" algorithm (see Eq. 2.7-2.8) to integrate the equations of motion with a time step Δt taken to be as large as possible while keeping the integration stable. We used $\Delta t = 0.003 - 0.006\tau$, where $\tau = \sigma(m/\varepsilon)^{1/2}$. We present our results in reduced units in which $\sigma = \varepsilon = m = 1$ and the Boltzmann constant $k_B = 1$. As an example, one can examine the well studied case of liquid argon; the distance and energy scales are then $\sigma = 3.4\mathring{A}$ and ε/k_B=120K, the natural time is $\tau = 2.16 \times 10^{-12}$ sec, and the molecular mass $m = 40$ a.u.

The simulation system is initially created by placing all particles at equal distance from each other with the appropriate density. We then connect M solvent particles together to form a polymer chain with the appropriate bond length. The system is then brought to equilibrium before applying a flow. This method is different from earlier versions of our simulation program where the particles were initially placed in a very diluted system and then compressed to the desired density (this method was not efficient for large systems of over 1000 particles).

The confinement is created by restricting the motion of the polymer and the solvent inside a capillary of square cross-section leaving only one direction with periodic boundary condition. A number of different schemes for representing walls in MD have been imple-

mented in the literature. The method chosen initially places the particles that make the wall of the capillary on an fcc lattice, whose spacing is chosen to obtain the desired density. The initial velocities of the wall particles are then randomly assigned subject to a fixed temperature. During the simulation, the wall particles are held at their lattice sites by a simple harmonic spring, i.e.,

$$U_w = \frac{1}{2} k_w \Delta r^2 \tag{2.15}$$

where k_w ($= 400\varepsilon/\sigma^2$ in our simulations) is a spring constant and Δr is the extension of the spring. Such a potential is used to obtain non-slip conditions at the wall. Further, the density of the wall (same as the entire system, $\rho = 0.85\sigma^{-3}$) does not allow any solvent particles or monomers to exit the confinement of the model capillary. Figure 2.4 shows a schematic representation of the potential energy involved in the interactions between monomers, solvent and wall particles.

There are two ways to simulate a flow around the polymer. The first and most widely used method is to apply a constant force (in the direction of the flow) to the fluid particles at every time step. Because we are dealing with very small systems and short times, some care must be taken when defining the applied forces. Typical velocities and forces used in MD simulations are of order 10^1 (using our reference units ε, σ, m) whereas typical laboratory gravity would be of order 10^{-13}.

We tested the above method by using our MD simulation program. In our test, the system is composed of solvent and wall particles (9728 particles in total) inside a rectangular capillary ($16.9 \times 16.9 \times 40.1$). Only the periodic boundary condition in the axial direction remained. A force $F_v = 0.1$ is applied to all solvent particles to generate a flow. Figure 2.5 shows the velocity profile of the Poiseuille-like flow obtained inside the capillary. We observed that the velocity of the solvent V is zero close to the wall and increases to a maximum value of $V \approx 0.63$ in the middle of the capillary. The no-slip condition has emerged naturally in our simulation. Note that the temperature of the wall particles is kept constant by periodically rescaling their velocities.

The second method to simulate a solvent flow around the polymer is to pull the tethered polymer along the tube principal axis at constant velocity V to mimic a plug flow. There are other methods in the literature to mimic such a flow, e.g., imposing a concentration

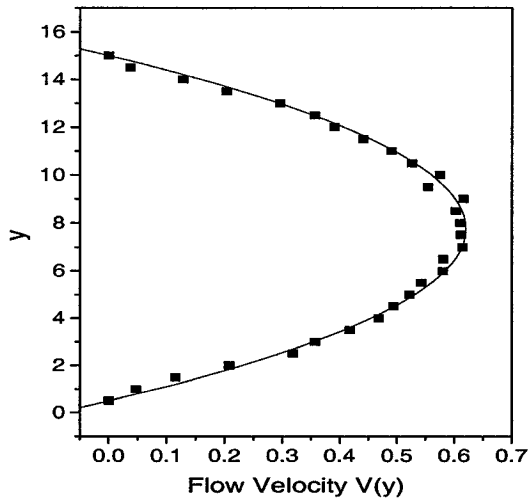

Figure 2.5: Velocity profile of a Poiseuille flow with $F_v = 0.1$ fitted to a parabolic function.

gradient. Pulling the polymer is a much simpler model and gives the desired plug flow. The effect of a Poiseuille flow on the dynamic and static properties of a polymer would have added to the complexity of the problem. The algorithm is implemented as followed: 1) we introduce a phantom particle which interacts only with the first monomer of the polymer chain through our FENE potential (Eq. 2.13); and 2) we then apply a constant velocity to that particle along the tube axis. The average stress in the phantom spring gives us the mean drag force generated by the entire polymer chain. Figure 2.6 gives a good schematic representation of the simulation system. Similarly, we could have pulled the polymer at constant force. The final results would have been similar, except perhaps for short chains.

Motion of the solvent particles occur in all of the methods to simulate a relative flow, meaning that work is being done on the system. This will tend to increase the temperature and give a net momentum to the solvent particles. However, we expect this increase in temperature to be fairly small in our algorithm. To eliminate such momentum and energy drifts, we renormalize the magnitude and the direction of the velocities of solvent particles far from the polymer periodically during the course of the simulation. In other words, we

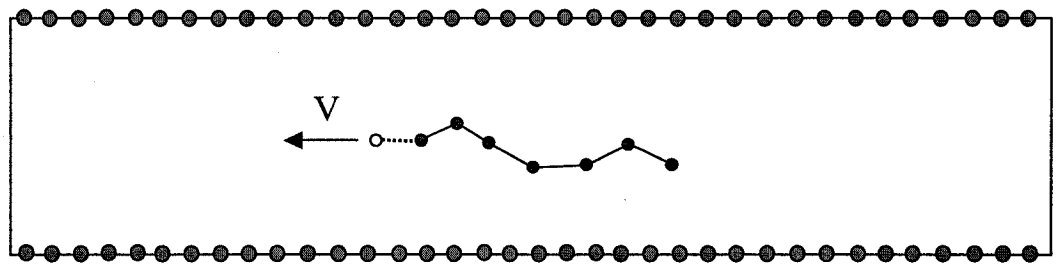

Figure 2.6: Polymer pulled at constant velocity inside a capillary. The phantom particle moving at constant velocity V is represented by the empty monomer.

separate the tube into two sections: 1) solvent particles which are hydrodynamically close to the polymer; and 2) solvent particles which are hydrodynamically far from the polymer. Figure 2.7 provides a picture of this scheme.

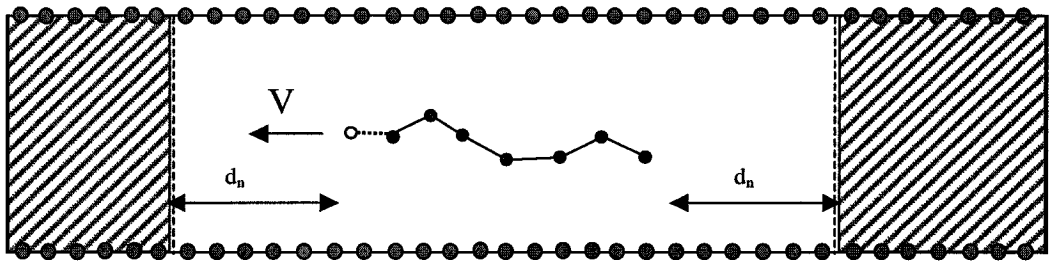

Figure 2.7: Normalization regions for the velocity of solvent particles.

Table 2.2 shows the effect of different rescaling distances d_n on the mean end-to-end distance $\langle h_x \rangle$ and the mean drag force $\langle F_x \rangle$ in the direction of the tube axis (x-direction) for a polymer of length M=20 and a pulling velocity of V=0.1 inside a capillary. We notice that the end-to-end distance is not affected and that the largest variation of the drag force is about 2%. During the course of our simulation, the normalization distance d_n is fixed between 10 and 15.

When carrying out the simulation in a capillary, only one direction remains for the periodic boundary condition. The algorithm described above allows us to study the effect of confinement on the polymer. It also allows us to study the characteristic of the flow of solvent particles around the polymer and along the walls. Such a study will be the content of this chapter.

distance d_n (σ)	$\langle h_x \rangle$ (σ)	$\langle F_x \rangle$ (ε/σ)
5	18.739 ± 0.001	8.79 ± 0.06
10	18.738 ± 0.001	8.84 ± 0.06
15	18.736 ± 0.001	8.76 ± 0.06
15	18.739 ± 0.001	8.87 ± 0.08
20	18.738 ± 0.001	8.92 ± 0.06

Table 2.2: Effect of the normalization distance d_n on the polymer properties.

Figure 2.8 gives a representation of our simulation program:

1. The simulation program first reads the initial parameters of the simulation such as the thermodynamic temperature, the density of the system, the total number of particles, the size of the system, etc.

2. We create the system or read an old system file for the initial positions of the particles and their velocities.

3. We sort the particles into two arrays that compose the cell index structure.

4. We evaluate the force and potential energy on each particle.

5. We start the main loop of the simulation. We calculate the new positions of all particles and their mid-step velocities.

6. Since the particles have moved, we update the two arrays that compose the cell index structure model.

7. We evaluate the force and potential energy on each particle again.

8. We calculate the velocities of all particles and the total kinetic energy. We go back to step 5.

9. After a certain number of steps, the system kinetic temperature is renormalized to the thermodynamic temperature.

10. We perform some analysis on the system and output the results of the simulation. We go back to step 5.

11. We output the positions and velocities of all particles to be able to re-start the simulation if needed.

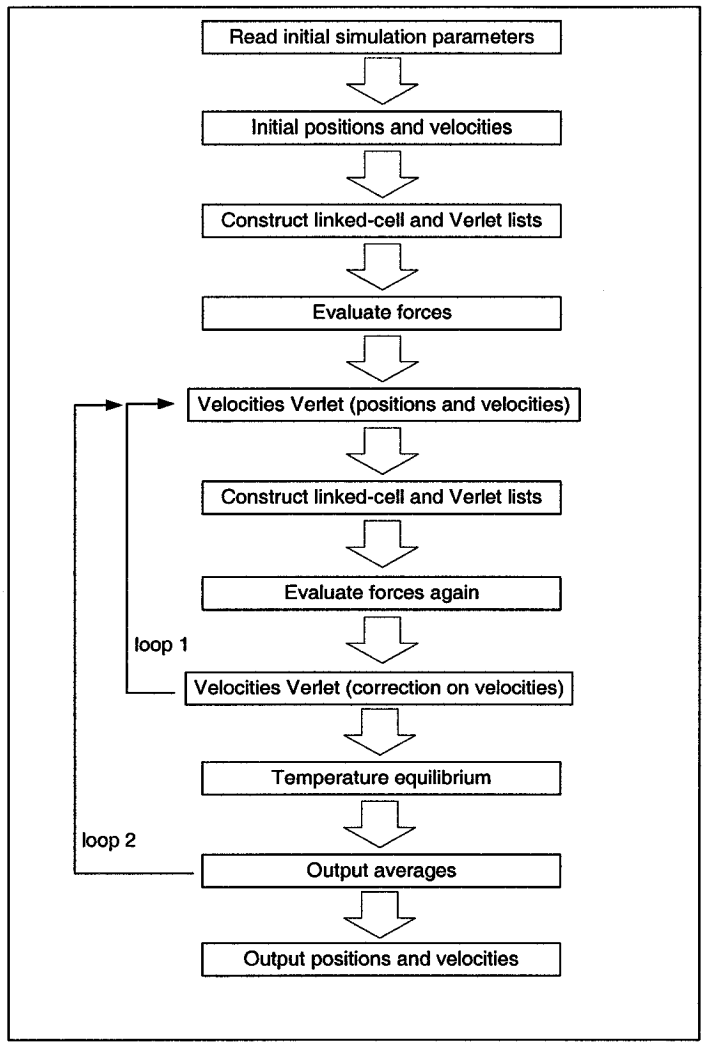

Figure 2.8: A flow-chart of our MD simulation program.

2.3.1 Test 1: Dynamics of Entangled Linear Polymer Melts

In this section, we present MD simulation results for a bead-spring model of a melt of linear polymers. These simulations are not intended to study the dynamics of such a system but

to validate our MD simulation program with known results. Our results are compared with those obtained by Kremer and Grest [69].

The systems are simulated at a number density $\rho = 0.85\sigma^{-3}$ and a temperature $T = 1.0\varepsilon/k_B$ in a cubic box of size L with periodic boundary conditions in all three cartesian directions (no walls). The interaction potential has two parts. The first part is the modified Lennard-Jones potential which acts between all monomers in the system (see Eq. 2.12). Along the backbone of the chains, we added a FENE potential (see Eq. 2.13). We used $\Delta t = 0.006\tau$.

The simulation system composed of N_m polymers of length M was prepared in a semi-dilute state and then slowly compressed to the desired density $\rho = 0.85\sigma^{-3}$. We then let the system equilibrate until the chains moved several chain lengths. Table 2.3 shows a summary of the simulation results.

$N_m : M$	$\langle R_g^2 \rangle / \sigma^2$	$6D \times 10^3 (\tau/\sigma^2)$	L/σ
50:5	0.92 ± 0.01	90 ± 2	6.65
25:10	2.20 ± 0.02	39 ± 1	6.65
30:20	4.90 ± 0.05	20 ± 1	8.90
32:25	6.31 ± 0.07	16.0 ± 0.8	9.80
16:50	13.2 ± 0.2	5.4 ± 0.5	9.80

Table 2.3: Radius of gyration R_g and diffusion coefficient D for some polymer melts.

The mean-square radius of gyration is calculated using the definition

$$\langle R_g^2(M) \rangle = \frac{1}{M} \left\langle \sum_{i=1}^{M} (\mathbf{r}_i - \mathbf{r}_{cm})^2 \right\rangle \tag{2.16}$$

where $\mathbf{r}_{cm} = \frac{1}{M} \sum_i \mathbf{r_i}$ is the position of the center of mass of the chain. The diffusion coefficient D of the polymer chain is simply given by

$$D(M) = \frac{\langle (\mathbf{r}_{cm}(t) - \mathbf{r}_{cm}(0))^2 \rangle}{6t} \,. \tag{2.17}$$

Our simulation results are also plotted against those of Kremer and Grest in Figures 2.9 (a) and (b). These figures demonstrate that our MD simulation program is able to reproduce, with excellent agreement, these standard and well established numerical results.

Figure 2.9 (a) gives the mean square radius of gyration versus M for $5 \geq M \geq 50$. We observe that $\langle R_g^2 \rangle$ scales as $M^{1.07 \pm 0.06}$, in good agreement with the expected prediction of $M^{1.0}$ for long ideal chains with screened excluded volume interactions. As for the diffusion coefficient (Figure 2.9 (b)), we expect the diffusion D to scale as M^{-2} for large polymers (reptation model) and M^{-1} for short ones (Rouse model). The polymer lengths used in our simulations were too small to observe the second regime. Nonetheless, our results agree well with those of Kremer and Grest up to $M = 50$.

(a) (b)

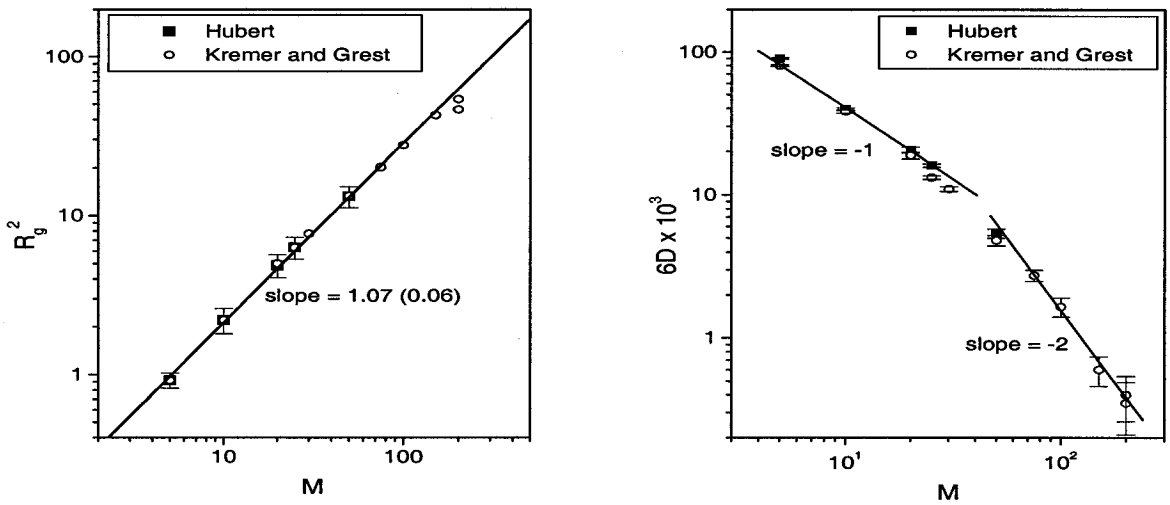

Figure 2.9: (a) Mean square radius of gyration square R_g^2 versus polymer length M. (b) Diffusion coefficient D versus polymer length M.

Using the bond length b between two consecutive monomers on the chain, the persistence length ℓ_p was estimated from the mean square end-to-end distance $\langle h^2 \rangle$ of the polymer chains (i.e., $\langle h^2(M) \rangle \equiv \langle (\mathbf{r}_1 - \mathbf{r}_M)^2 \rangle = 2b\ell_p(M-1)$ with $\mathbf{r}_1$ and $\mathbf{r}_M$ being the coordinates of the chain ends [69]):

$$\begin{aligned} b &= 0.965 \pm 0.002 \\ \ell_p &= 1.32 \pm 0.02 \, . \end{aligned} \tag{2.18}$$

These values were found to be independent of chain length and are similar to the ones obtained by Kremer and Grest [69]. The fact that $\ell_p \simeq b$ indicates that we indeed have a FJC.

2.3.2 Test 2: Static and Dynamic Properties of a Dilute Polymer Solution

We also tested our MD simulation program against known results for the effect of periodic boundary conditions on the static and dynamic properties of a dilute polymer solution, i.e., a system of one polymer surrounded by solvent particles. More specifically, we looked at the radius of gyration and the diffusion coefficient of the polymer. In this case, we expect large effects due to the long range of hydrodynamic interactions which were screened in the polymer melt studied in Section 2.3.1.

We used the same MD simulation program as in the previous sub-section. The system is now composed of $N-M$ particles of solvent and M monomers (only one polymer chain). Figure 2.10 shows the effect of the system size L on the mean square radius of gyration $\langle R_g^2 \rangle$. We observed that $\langle R_g^2 \rangle$ is not affected by the presence of periodic boundary conditions for $L \gg \langle R_g^2 \rangle$, in agreement with other simulations [92, 93]. Figure 2.11 gives the average diffusion coefficient D vs the inverse of the length of the system cell, $1/L$. In this case, the diffusion coefficient is greatly influenced by the size of the system. One can extrapolate the diffusion coefficient for an infinite system size with a simple linear fit as shown in Figure 2.11. The periodic boundary conditions do affect the dynamic properties of a polymer chain in a dilute solution such as the diffusion. Note that the effect of the periodic boundary conditions on the scaling of the radius of gyration and the diffusion coefficient has been extensively studied by many authors [92, 93]. The product of the diffusion coefficient and the radius of gyration should give a constant value, i.e., $D \times R_g = constant$, because $D \sim 1/R_g$ in the Zimm model. In our case, we obtain $D \times R_g = 167 \pm 7$ and 172 ± 15 for $M = 15$ and 25 respectively, in agreement with theoretical predictions. Note that these simulations were carried out solely to validate our simulation code.

2.3.3 The Cheon et al. Model

Recently, Cheon at al. have investigated the stretching of a polymer in a uniform flow using MD simulations [34]. All fluid particles and monomers interact with each other through the modified Lennard-Jones potential (Eq. 2.12). In addition, the polymer has a FENE potential that acts only between monomers along the chain (Eq. 2.13). Their simulation use $k_F = 30\varepsilon/\sigma^2$ and $R_F = 1.5\sigma$ like us.

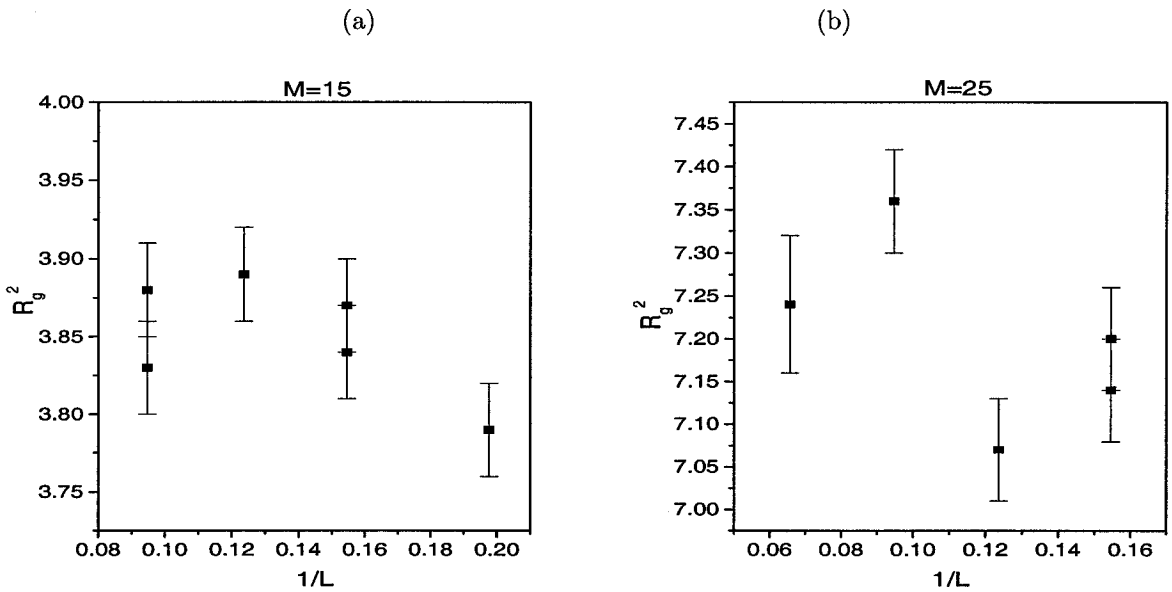

Figure 2.10: Mean square radius of gyration versus the inverse of the length of the system cell, $1/L$, for polymers of length (a) $M = 15$ and (b) $M = 25$.

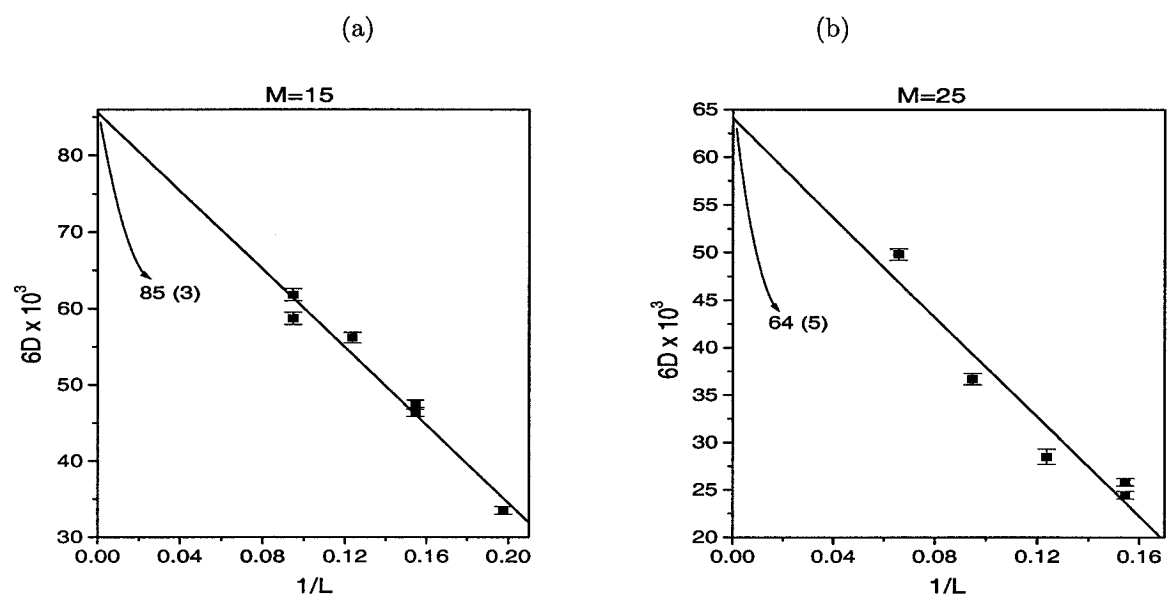

Figure 2.11: Diffusion coefficient D versus the inverse of the length of the system cell $1/L$ for polymers of length (a) $M = 15$ and (b) $M = 25$.

The fifth-order predictor-corrector method is used to integrate the equations of motion. The fluid flow velocity and its temperature are maintained at the desired values using simple rescaling. A temperature $T = 1.2\varepsilon/k_B$ is maintained during the course of the simulation using a thermostat which rescales velocities. A uniform flow is incorporated by adding a constant force at every time step to all fluid particles.

Cheon et al. use two different methods to carry out the rescaling of the velocities. The first consists in rescaling the velocities of all the fluid molecules. In the next method, the velocities of the fluid molecules outside an inner box surrounding the tethered chain molecule are rescaled while leaving the inner molecules untouched. They show that for a chain length of $M = 30$, the end-to-end distance in the direction of the flow did not exhibit any systematic trends with the largest variation being around 2% for the smallest flow velocity studied ($V = 0.03\sigma/\tau$) when using both procedures. Furthermore, they also show that the temperature in the inner box is slightly higher than that in the outer region with the largest increase being 0.3% for the highest velocity ($V = 0.3\sigma/\tau$).

Their algorithm is similar to the one we use in our study with the exception of the periodic boundary conditions (they do not have walls) and the way they simulate the solvent flow around the polymer. Their results will be compared to ours later in this chapter.

2.4 Theory

2.4.1 Polymer Pulled at Both Ends

The freely jointed chain model (FJC) treats the polymer as a chain of statistically independent (Kuhn) segments of length b (the Kuhn length is equal to the bond length for an ideal FJC) whose orientations are uncorrelated in the absence of external forces. If a force F_x (in the x-direction) is applied to both free ends of an ideal chain, each polymer segment will tend to align with the force. Thermal agitation, however, tends to randomize the orientation of the segments. In this model, the elastic response of the molecule is purely entropic, and the exact solution to this problem is well known [35]:

$$H(F) = coth(F) - \frac{1}{F} \cong \begin{cases} \frac{1}{3}F - \frac{1}{45}F^3 + \frac{2}{945}F^5 - O(F^7) & F \ll 1 \\ 1 - \frac{1}{F} & F \gg 1, \end{cases} \tag{2.19}$$

where $F = F_x b/k_B T$ is the scaled force, $H = h_x/L_p$ is the relative end-to-end distance (in the direction of the force) and L_p is the contour length of the polymer. The above equation can be inverted using series expansion,

$$F(H) \cong \begin{cases} 3H - \frac{9}{5}H^3 + \frac{297}{175}H^5 - O(H^7) & H \ll 1 \\ \frac{1}{1-H} & 1 - H \ll 1 \,. \end{cases} \tag{2.20}$$

Equation 2.20 can be approximate using the ratio of two polynomials as an interpolation tool, i.e., a modified Pade approximant: [94],

$$F(H) \cong \frac{3H - H^3}{1 - H^2}. \tag{2.21}$$

The last expression gives a maximum relative error of 4.9%. Note that the H^3 term was added to the numerator to ensure that the expression converges to the proper limit for $1 - H \ll 1$. The Warner approximation, which is more widely used, acutally overestimates the force by 50% close to full extension.

For the case of a real chain, the solution has been derived by Pincus [95] using a scaling approach. For a large force, we can see the chain as a series of blobs of size R_p before it becomes completely stretched. Inside a blob, the perturbation due to the applied force F_x is weak. The applied force is then derived from the entropy of a blob, given $F_x \cong k_B T/R_p$. Thus, we obtain a string of independent blobs with a radius that follows the Flory exponent, i.e., $R_p \sim b M_p^{3/5}$ where M_p is the number of monomers per blob. We can rewrite M_p in term of the tension F_x as

$$M_p = \left(\frac{k_B T}{b F_x}\right)^{5/3} . \tag{2.22}$$

The total number of blobs into which the chain deforms is M/M_p. Therefore, the chain elongation h_x in the direction of the force is given by

$$h_x = \frac{M}{M_p} R_p = Mb \left(\frac{F_x b}{k_B T}\right)^{2/3} = L_p F^{2/3} . \tag{2.23}$$

When the polymer is completely stretched ($F_x \cong k_B T/b$), excluded volume can be neglected and we recover $H \sim (1 - 1/F)$, as predicted by Eq. 2.19 above.

For a worm like chain (WLC), the Kuhn length b_k is no longer equal to the bond length b because of the chain rigidity. Marko and Siggia [36] proposed a statistical mechanical treatment of the WLC model to analyze the experiments in which DNA, tethered at one end, was stretched by a mechanical force applied directly to the free end, by an electric

field, or by hydrodynamic flow. Self-interactions or excluded volume effects were considered negligible under such experimental conditions. For large forces F_x, they obtained the following approximative law for the relative extension of the polymer H [96]:

$$H(F) = 1 - 1/(2F)^{1/2} \tag{2.24}$$

where $F = F_x b_k / k_B T$ is the new scaled force. This is different from the FJC model where we had $H \cong 1 - 1/F$ for large forces [97]. For small forces $F \ll 1$, the extension increases linearly with the force, that is, $F \sim H$. Marko and Siggia thus derived an approximate interpolation force versus extension function for the WLC:

$$F(H) = 2H + \frac{1}{2(1-H)^2} - \frac{1}{2} \cong \begin{cases} 3H + O(H^2) & H \ll 1 \\ \frac{1}{2(1-H)^2} & 1 - H \ll 1. \end{cases} \tag{2.25}$$

This equation is asymptotically exact in the large and small force limits. Experimental results by Smith et al. [98] show deviations from the Marko-Siggia approximation at high extension. A modification to Eq. 2.25 has been derived by Odjik [99] that takes into account stretching of a DNA chain slightly beyond full extension,

$$F(H) = 2H + \frac{1}{2(1 - H + F/K_0)^2} - \frac{1}{2} - \frac{2F}{K_0} \tag{2.26}$$

where $K_0 = k_0 b_k / k_B T$ and k_0 is the stretch modulus.

The following equation gives the asymptotic scaling behavior for the FJC and WLC models:

$$1 - H \sim \begin{cases} F^{-1} & \text{FJC} \\ F^{-1/2} & \text{WLC.} \end{cases} \tag{2.27}$$

This will play an important role later in this chapter.

2.4.2 *Tethered Polymer Submitted to a Flow*

There has been considerable theoretical work on the conformations of a polymer chain under strong flows. Brochard-Wyart proposed that under a constant and uniform flow velocity, a flexible polymer chain will undergo three types of conformations before being completely stretched: 1) unperturbed (random coil) at low flow; 2) "trumpet", i.e., partly stretched and modelled as a sequence of increasingly larger blobs at intermediate flow; and 3) "stem and flower", with a completely stretched portion followed with a "trumpet" portion, at higher flow. These conformations can be seen in Figure 2.12.

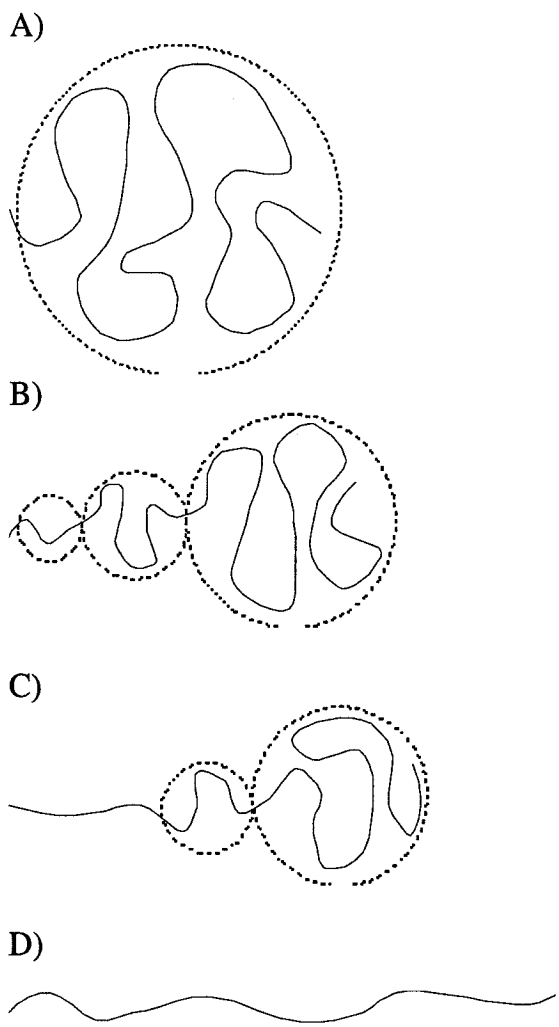

Figure 2.12: Chain conformations under a constant and uniform flow: (a) random coil, (b) trumpet, (c) stem and flower, and (d) stretched. This should be compared to Figure 2.1

In the unperturbed state, the polymer starts as a coil of size $R_g \cong M^{3/5}b$, typical for a polymer in a good solvent. Things change when the tension in the chain is comparable to the Stokes drag force in the flow,

$$\eta R_g V \approx \frac{k_B T}{R_g}, \tag{2.28}$$

where η is the solvent viscosity. The left hand side of the equation represents the drag force of a sphere (ηR_g being the friction coefficient) and the right hand side represents the entropic force. Equation 2.28 gives us the critical flow velocity at which the polymer will start deforming,

$$V_{coil} = \frac{k_B T}{\eta R_g^2} \,. \tag{2.29}$$

In the trumpet state, one can picture the chain as a series of impenetrable blobs. The drag force of the trumpet F_x is the sum of the friction force on all blobs [39],

$$F_x(h_x) = \eta V \sum_i R_{pi} = \eta V h_x \tag{2.30}$$

where R_{pi} is the size of the i-th blob. Using equation 2.23, the total extension is then given by

$$h_x(M) = M^3 b^5 \left(\frac{\eta V}{k_B T}\right)^2 \sim M^3 V^2 \,. \tag{2.31}$$

The profile (or lateral span) of the trumpet is given by the Pincus relation [95]

$$y(x) \approx k_B T / \eta V (h_x - x) \tag{2.32}$$

where x is the distance from the tethered end. Note that the trumpet regime exists only if the size of the first blob (the smallest one) is larger than the size of a monomer. This limitation corresponds to a second critical flow velocity

$$V_{trumpet} = M^{1/5} V_{coil} \,. \tag{2.33}$$

In the stem and flower regime, the chain is elongated into a stem with a diameter given by the size of a monomer and is terminated by a small trumpet. The extension of the polymer is given by

$$h_x = L_{stem} + L_{trumpet} \tag{2.34}$$

where L_{stem} is the length of the stem and $L_{trumpet}$ is the length of the remaining trumpet. The number of monomer m^* in the trumpet can be calculated using $\eta V h_x(m^*) = k_B T/b$ and Eq. 2.31:

$$m^* = M\frac{V_{trumpet}}{V}, \tag{2.35}$$

leaving $M - m^*$ monomer in the stem (or $L_{stem} = (M - m^*)b$). The total extension of the polymer is simply $h_x = (1 - (2V_{trumpet}/3V))Mb$.

The last two regimes ("trumpet" and "stem and flower") have been observed by video-microscopy by Wirtz in a melt of polymers [19] (see Figure 2.1). We will show that these conformations and properties change when the polymer chain moves in strongly confined environments.

2.4.3 Tethered Polymers Submitted to a Shear Flow

Ladoux and Doyle [22] have studied the stretching of tethered chains subject to a shear (Poiseuille or parabolic) flow similar to the one shown in Figure 2.5. They modelled the high shear rate deformation of the chain which takes into account the relationship between the transverse fluctuations of the extended chain and its nonlinear elastic properties. As the shear rate increases, the chain adopts a conformation that is closer to the surface where the flow velocity is smaller. This effect, combined with the nonlinear elasticity properties of the polymer, is what gives rise to the slow approach to full extension of sheared tethered chains.

These authors found a scaling law

$$1 - H \sim \begin{cases} \dot{\gamma}^{-2/3} & \text{FJC} \\ \dot{\gamma}^{-1/3} & \text{WLC} \end{cases} \tag{2.36}$$

where $\dot{\gamma}$ ($\sim F$) is the flow shear rate. This is quite different from the laws reported in Eqs. 2.27 for mechanical stretching.

2.4.4 Polymers in Confined Environments

When the polymer is confined between two planar surfaces separated by a distance ζ, its friction coefficient (or its conformation) is greatly modified. In the case of the "stem and flower" conformation, Bakajin et al. [20] distinguished three classes of confinement: 1)

$\zeta < L_{trumpet}$: long range interactions are screened; 2) $\zeta < R_{p0}$: intermediate range interactions are screened, where R_{p0} is the diameter of the largest blob; and 3) $\zeta < \ell_p$: hydrodynamic interactions are completely screened, where ℓ_p is the persistence length of the polymer. In the first case where the distance ζ between the walls is smaller than the extension h_x of the "stem and flower" polymer, they suggested that the interactions between the flower and the stem, and those between the blobs in the flower, were diminished, i.e., the polymer has the friction of a cylinder confined between parallel walls which has for effect to increase the drag force. In the second case, when the distance between the walls is smaller than the terminal diameter of the "stem and flower" polymer, interactions within individual blobs in the flower are reduced, the structure is modified and the drag force increases further. Finally, when the distance between the walls gets smaller than the persistence length ℓ_p of the polymer chain, the motion of each segment is hydrodynamically decoupled, the polymer becomes free-draining, and drag forces are at maximum. Using computer simulations, we will see how the polymer evolves through these different regimes.

2.5 Results

2.5.1 The Freely Jointed Chain

Monomer Density

We now investigate the effect of confinement on a tethered FJC polymer pulled at constant velocity. The diameter of the capillary varies between $8.4 \leq D_c \leq 30.6$ whereas its length varies between $47.5 \leq L \leq 190$ depending on the contour length $L_p(M)$ of the polymer ($5 \leq M \leq 100$) being pulled. The polymer chain link potential is the sum of the modified Lennard-Jones and FENE potentials.

Figure 2.13 shows the average density plot of a polymer of length $M = 40$ at different flow velocities. For low-velocity flows, the polymer deforms into a cylindrical shape due to the confinement of the capillary walls (Figure 2.13 (b)). As the velocity increases, the polymer adopts a conical shape (similar to the "trumpet" and "stem and flower" regimes) until completely stretched.

Perkins et al. [63] visualized the stretching of a tethered DNA by a flow using fluorescence microscopy. They were able to calculate the monomer densities $\rho_M(x)$, where x is

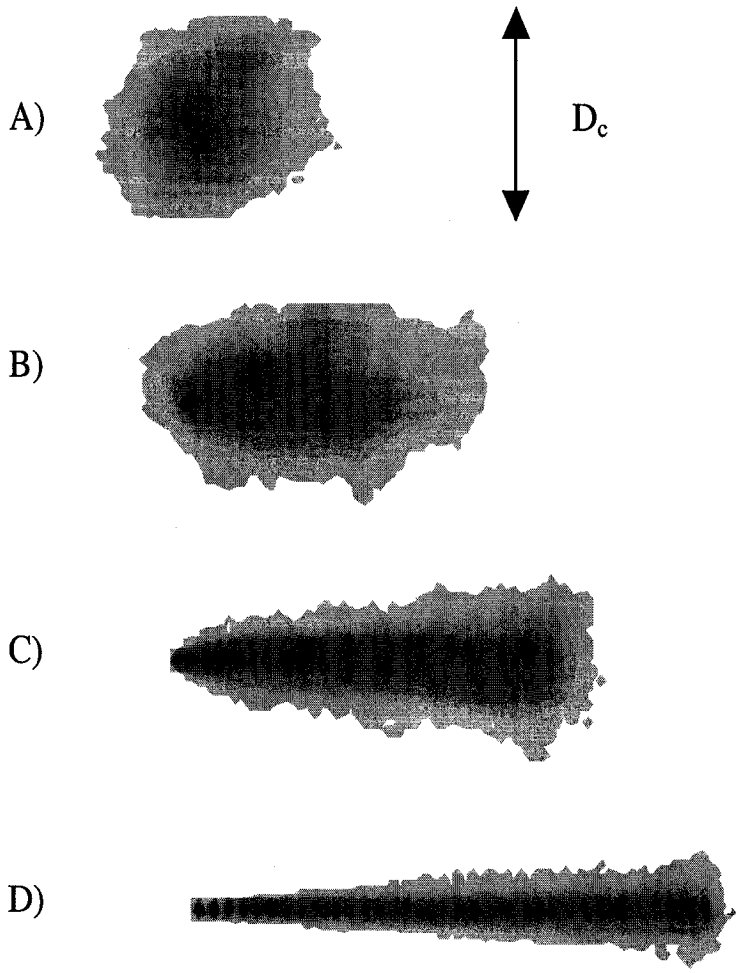

Figure 2.13: Density plots showing the likely locations of the monomers. The polymer chain ($M = 40$) is pulled from one end at constant velocity V inside a capillary of diameter $D_c = 14.8$: a) $V = 0.0$, b) $V = 0.005$, c) $V = 0.05$ and d) $V = 0.5$.

the distance from the tethered end of the polymer in the direction of the flow for different flow velocities. They observed an excess of monomers close to the free end of the chain which progressively decreases as the flow velocity increases and the chain extends (see Figure 2.14). These experimental data are qualitatively similar to our simulation results (see Figure 2.15) and those of Cheon et al. [34]. Figure 2.15 show the average monomer density $\langle \rho_M(x) \rangle$ $(= \frac{average\ \#\ monomer}{slice\ of\ width\ \sigma})$ vs. the distance from the tethered end x inside a capillary diameter of $D_c = 14.8$. The zero position is the location of the tethered monomer. For a polymer to deform, the force exerted by the solvent on the polymer must exceed its entropic cohesion,

$$F > \frac{k_B T}{R_g} \tag{2.37}$$

where R_g is the equilibrium polymer radius of gyration. Since $R_g \sim M^{3/5}$ for an ideal chain with excluded volume, large polymers are easier to deform than smaller ones. This process is observed in Figure 2.15 (a), (b) and (c). For instance, a polymer of length $M = 15$ is still in a random coil conformation at small flow velocities whereas a polymer of length $M = 40$ is already partially deformed.

For longer polymers and higher flow velocities, we observe small oscillations in the monomer densities (Figure 2.15 (d)). These oscillations are due to the fact that at such high velocities, the tethered end of the polymer is fully extended in the direction of the flow, making the displacement of the first few monomers very limited. Since the figures are plotted at constant interval from the tethered monomer, some intervals have higher monomer densities. Changing the plotting intervals would reduce such artifacts.

Figure 2.16 shows the effect of confinement on the monomer densities. For high velocity flows, the effect of confinement is negligible, Figure 2.16 (b), since the polymer becomes free-draining and remains along the tube axis when completely extended. At lower flow velocities, Figure 2.16 (a), the polymer deformation is greater as the confinement increases (for small capillary diameters), i.e., hydrodynamic interactions between the polymer segments are screened [20].

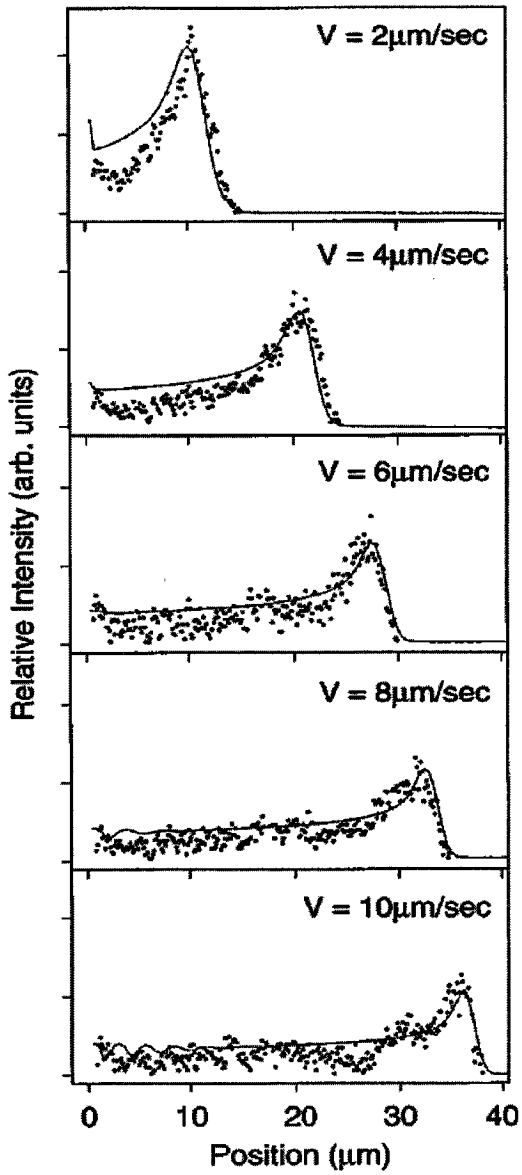

Figure 2.14: Monomer density as a function of position downstream of the tether point for a DNA length of $L_p = 67.2\mu m$ (symbols) subjected to different velocity flows. The line represents the simulation results of ref. [65]. Reproduced from ref. [65].

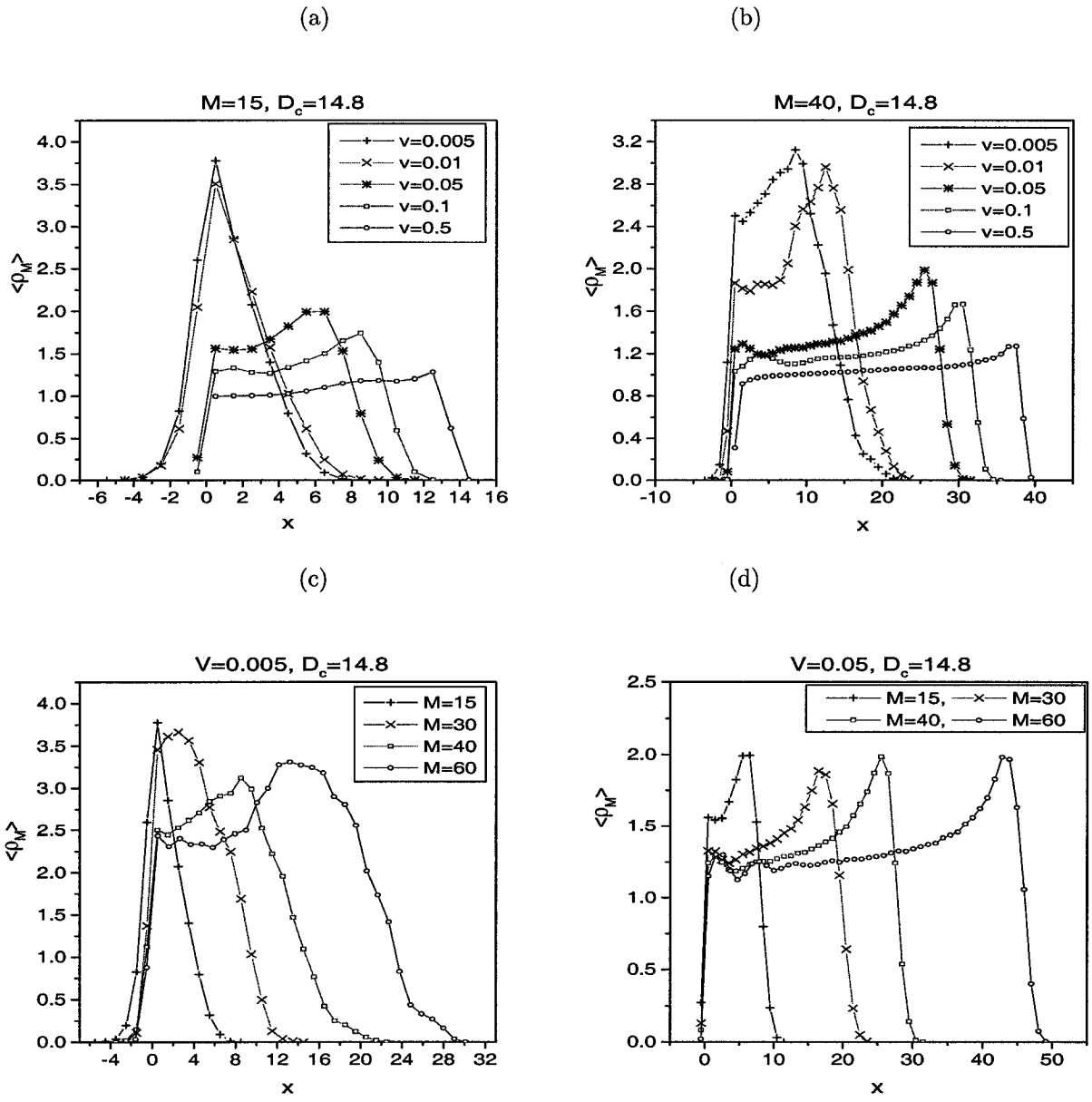

Figure 2.15: Average monomer density $\langle \rho_M(x) \rangle$ vs. the distance from the tethered end of a polymer inside a capillary of diameter $D_c = 14.8$ for $0.005 < V < 0.5$ and (a) $M = 15$ and (b) $M = 40$. Figure (c) is for a polymer pulled at a velocity $V = 0.005$ where the polymer length varies between $15 < M < 60$ whereas (d) is for a polymer pulled at a velocity $V = 0.05$.

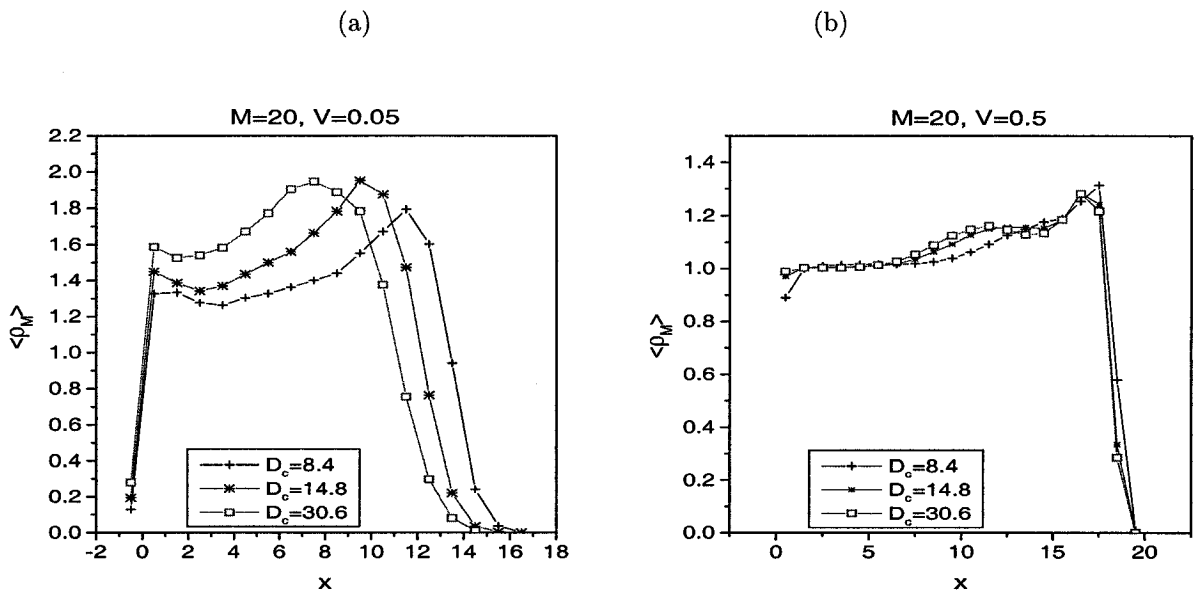

Figure 2.16: Average monomer density $\langle \rho_M(x) \rangle$ vs. the distance from the tethered end of a polymer of length $M = 20$ pulled at a constant velocity (a) $V = 0.05$ and (b) $V = 0.5$. The diameter of the capillary varies between $8.4 < D_c < 30.6$.

Transverse Polymer Conformational Width

Similarly, the average transverse widths $\langle L_t(x) \rangle$ (which is defined as the average lateral position of each monomer within a slice of width σ) show the same characteristics as $\langle \rho_M(x) \rangle$. Small chains retain a random coil conformation at low velocities in spite of the drag forces exerted by the solvent (Figure 2.17 (a) and (c)) while the deformation of longer polymers is obvious even at flow velocities as low as $V = 0.01$ (Figure 2.17 (b)). For intermediate and high flow velocities, the width of the polymer increases approximately linearly along the chain with a sharp drop-off as one approaches the free end of the chain. These qualitative results also agree with the simulation results of Cheon et al. [34].

Brochard-Wyart [39] predicted that the transverse width L_t of a polymer in the "trumpet" state should satisfy the relation $L_t(x) \sim (h_x - x)^{-1}$. None of our results in Figure 2.17 satisfy this prediction. This was expected since her model was developed for very long polymers (in the scaling limit) and the velocity range of the "trumpet" regime is quite narrow. For very high flow velocities, the polymer stretches beyond 80% of its full length

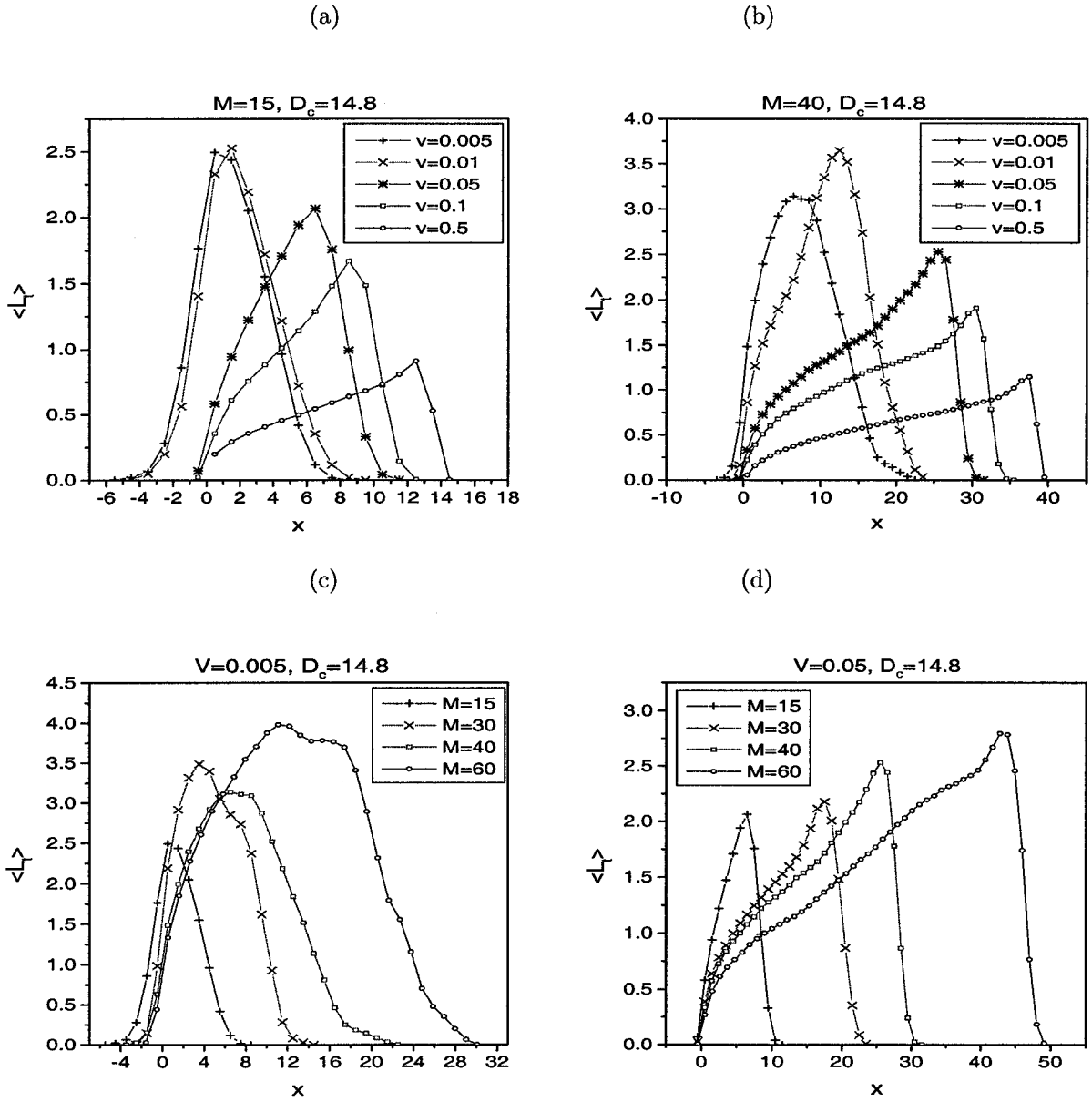

Figure 2.17: Average transverse width $\langle L_t(x) \rangle$ vs. the distance x from the tethered end for a polymer inside a capillary of diameter $D_c = 14.8$ for (a) $M = 15$ and (b) $M = 40$ at different velocities and for (c) $V = 0.005$ and (d) $V = 0.05$ for different polymer lengths.

and essentially assumes a "stem and flower" conformation with a fat stem and a trailing flower (Figure 2.17 (b)).

Figure 2.18 shows the effect of confinement on the transverse width (or span) of the conformations. For high velocity flows, the effect of confinement is negligible (Figure 2.18 (b)) for capillary diameters $D_c > 14.8$. For smaller capillary diameters, the polymer transverse width is reduced and its extension is increased due to the pressure exerted by the walls and to the screening of the hydrodynamics interactions as predicted by Bakajin et al [20]. This effect is even more pronounced when the velocity flow is low (Figure 2.18 (a)).

(a) (b)

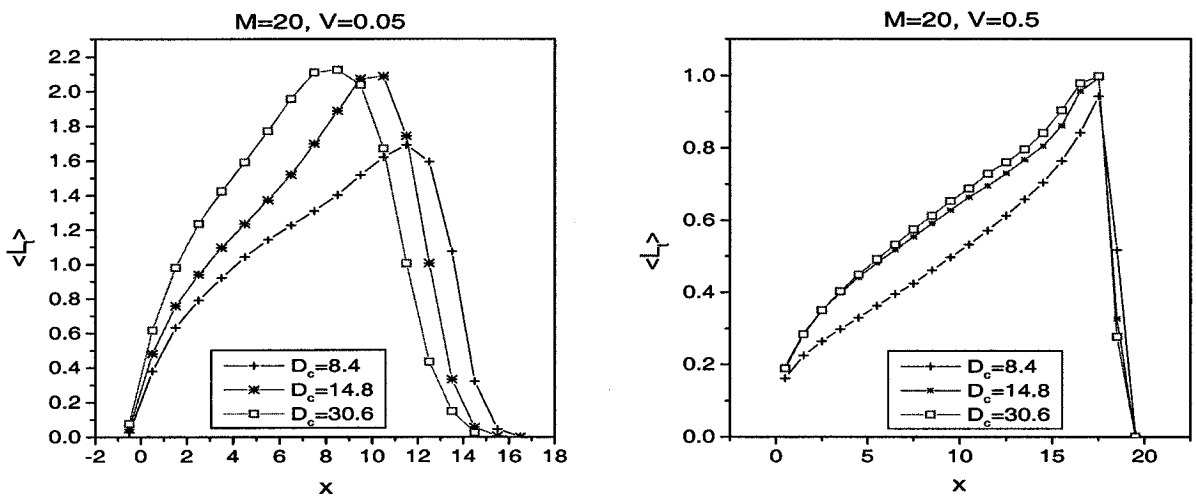

Figure 2.18: Average transverse width $\langle L_t(x) \rangle$ vs. the distance x from the tethered end for a polymer of length $M = 20$ pulled at a constant velocity (a) $V = 0.05$ and (b) $V = 0.5$ where the diameter of the capillary varies between $8.4 < D_c < 30.6$.

Local Bond Orientation

Figure 2.19 shows the average cosine of the angle between the chain bonds and the flow direction. The first link represents the bond between the phantom bead and the first monomer and is thus non-physical. We observe that the orientation of the polymer decreases

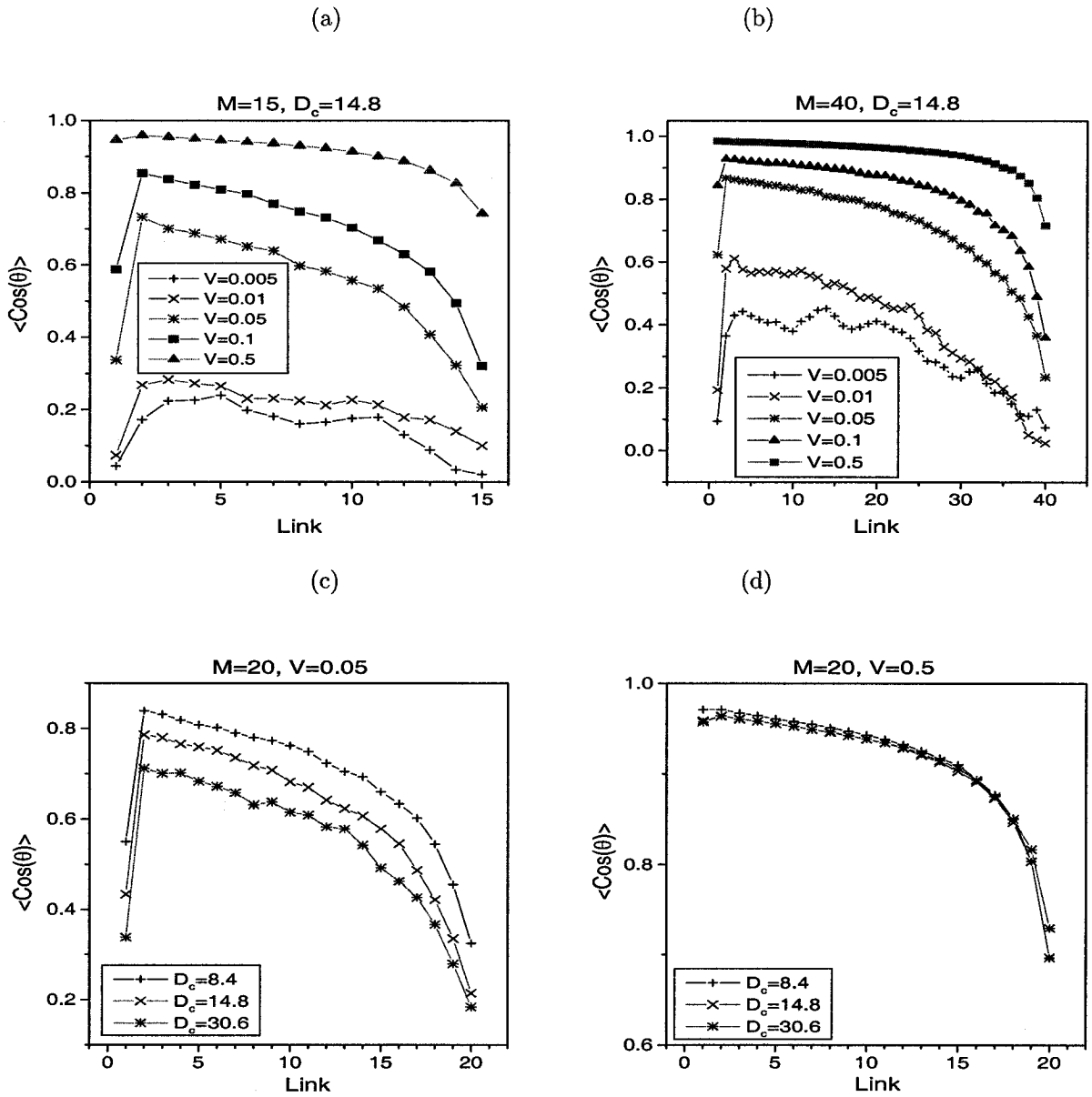

Figure 2.19: Average cosine of the bond angle, $\langle cos(\theta) \rangle$, along the flow direction for polymer of lengths (a) $M = 15$ and (b) $M = 40$ inside a capillary of diameter $D_c = 14.8$ pulled at various velocities $0.005 < V < 0.5$. Figures (c) and (d) show the results for a polymer of length $M = 20$ pulled at velocities $V = 0.05$ and $V = 0.5$, respectively, inside a capillary of diameter $8.4 < D_c < 30.6$.

slowly from the tethered end to the free end, as expected. Further, we observe that the orientation of large polymers is more pronounced since they deform more easily. The effect of confinement on the orientation of the links are negligible at high flow velocities. At lower flow velocities, the chain segments become more oriented as we reduce the capillary diameter. The polymer is more extended and oriented in a more compressed environment.

Local Bond Tension

Figure 2.20 shows the average tension $\langle F_{tx} \rangle$ for each polymer link in the direction of the flow. Again, the first link represents the bond between the phantom bead and the first monomer and the average drag force $\langle F_x \rangle$ of the entire chain. For a free-draining chain, the tension, which represents the sum of the drag forces starting from the free end, should decay linearly. We do indeed observe this linear regime at medium and high flow velocities. Further, the tension becomes negative at equilibrium due to the liquid density used in our simulation, i.e., the number of collisions between the monomers and the solvent increases slightly the equilibrium bond length value of the link potential. As seen previously, the average bond length is 0.965 ± 0.002 whereas the mathematical equilibrium length of F_{tx} is ≈ 0.960897 using our FENE and Lennard-Jones potentials. For small flow velocities, the effect of confinement on the tension in the links is negligible. Increasing the confinement changes the behaviour of the tension, the polymer is more extended and more tension is exerted on each monomer link. This becomes more obvious at higher flow velocities.

Monomer Position

Figure 2.21 shows a plot of the average location of each monomer along the flow direction with respect to the tether end. The data shows some bunching of monomers near the free end for low and medium velocities, whereas a new regime in which the monomers are clearly separated is found for high flow velocities.

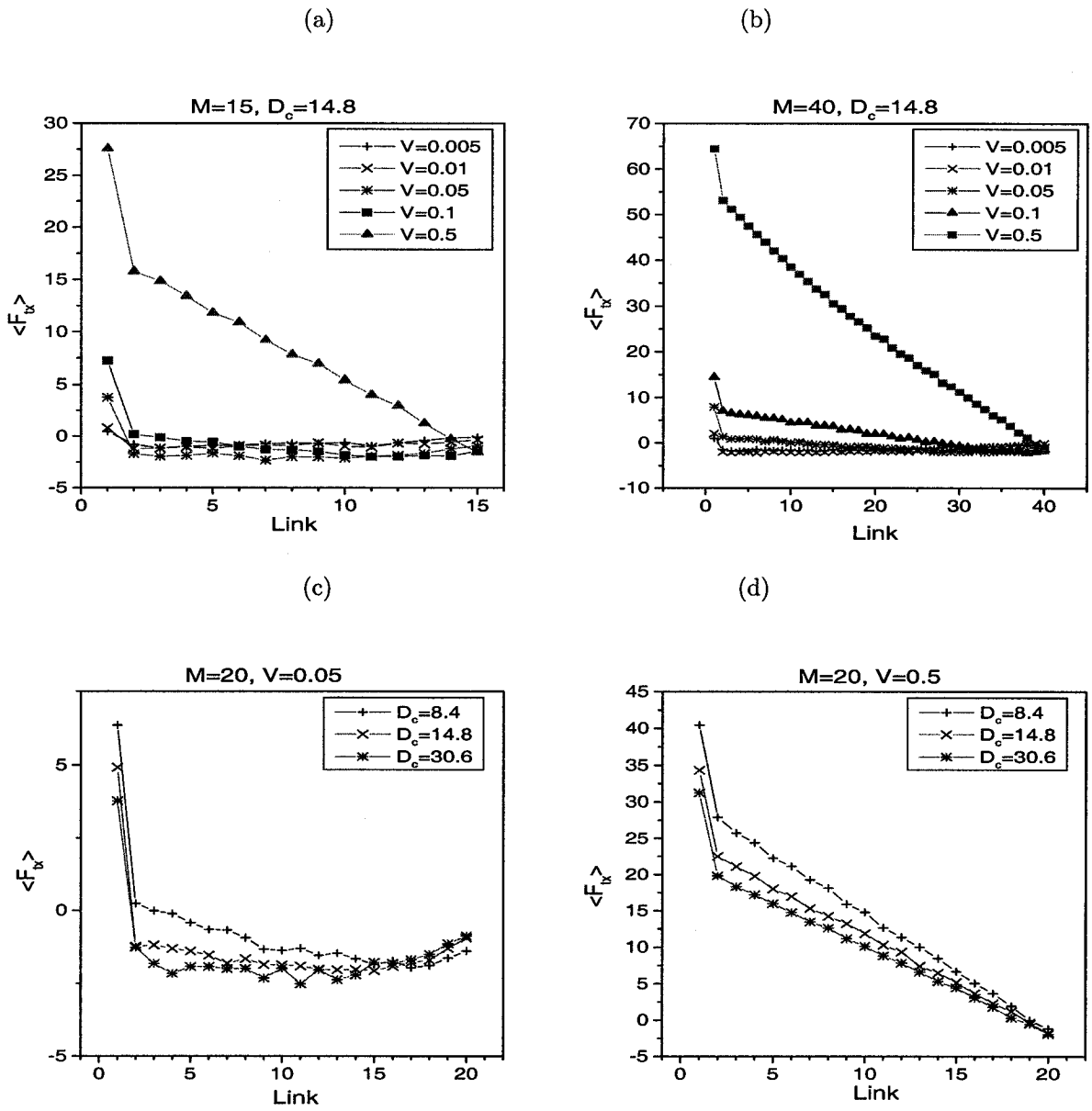

Figure 2.20: Average tension $\langle F_{tx} \rangle$ in the bond along the flow direction of for polymers of length (a) $M = 15$ and (b) $M = 40$ inside a capillary of diameter $D_c = 14.8$ and pulled at various velocities $0.005 < V < 0.5$. Figures (c) and (d) show the results for a polymer of length $M = 20$ pulled at velocities $V = 0.05$ and $V = 0.5$, respectively, inside a capillary of diameter $8.4 < D_c < 30.6$.

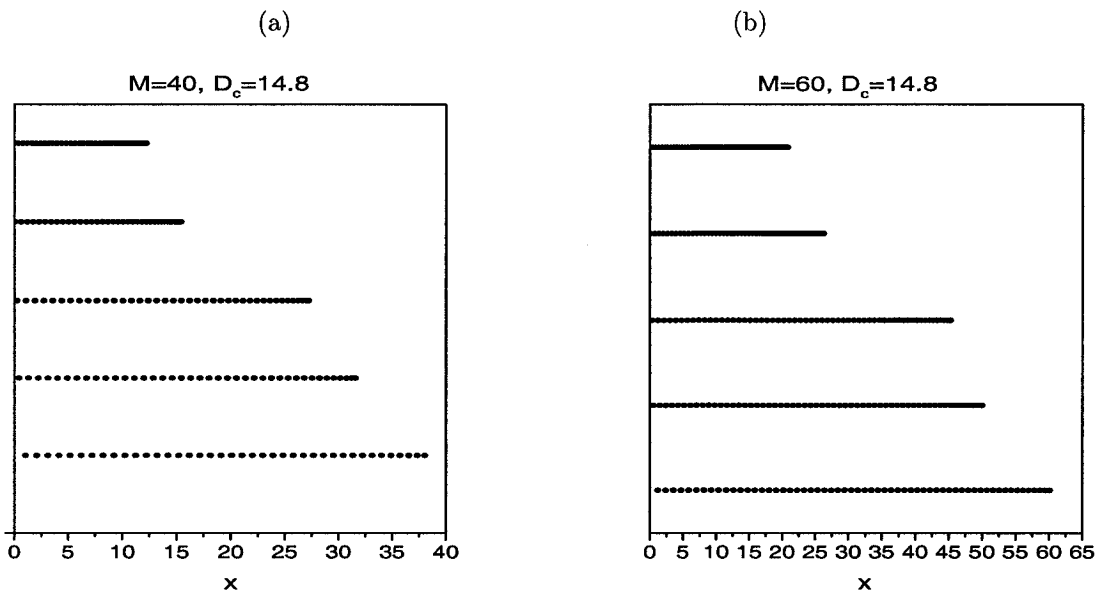

Figure 2.21: Average location of each monomer along the flow direction for molecules of size (a) $M = 40$ and (b) $M = 60$ inside a capillary of diameter $D_c = 14.8$. The velocities (from top to bottom) are $V = 0.005, 0.01, 0.05, 0.1$ and 0.5.

Drag Forces

We calculated the average Stokes drag force $\langle F_x \rangle$ (simply the force exerted on the phantom bead in the direction of the flow) and the average end-to-end distance $\langle h_x \rangle$ $(= \sqrt{\langle r_{xM} - r_{x1} \rangle^2})$ for each simulation, and fitted these data against the Marko and Siggia relations (Eq. 2.25) with fitting parameters b and L_p (Figure 2.22). For chain lengths $M = 20$, 30, 40 and 60 inside a capillary of diameter $D_c = 14.8$, the best global fit is obtained for $b = 0.66$ and L_p values of 20.1, 31.0, 41.8 and 65.3 respectively. Cheon et al. obtained values of $b \approx 0.38$ for polymer lengths $L_p = 24.8$, 33.5, 42.5, 52.4 and 61.7 ($M = 30$, 40, 50, 60 and 70). Note that these authors used the extension measured as the change in the distance spanned by the chain in the flow direction due to the flow. Fitting our data for the span gives similar results, that is, $b = 0.40$ for polymer lengths $L_p = 15.4$, 23.8, 34.9 and 50.1. We also observed that the Marko and Siggia relation does not agree with our results for small drag forces.

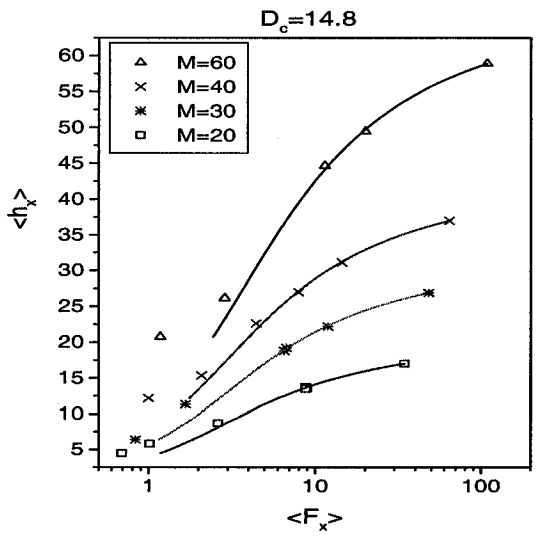

Figure 2.22: The average end-to-end distance vs. the average drag force (both in the direction of the flow) for molecules of size $20 < M < 60$ inside a capillary of diameter $D_c = 14.8$. The curves are numerical fits using the Marko and Siggia relation (Eq. 2.25).

When a polymer becomes free-draining, its drag force increases linearly with the molecule's contour length L_p because the hydrodynamic interactions are screened. In this case the polymer is a linear rod for the solvent. Figure 2.23 shows a log-log plot of the drag force $\langle F_x \rangle$ vs. the length of the polymer L_p (define as the sum of each segment length). We do observe the linear regime (slope of 1) for high flow velocities where the polymer becomes free-draining and completely stretched. For lower velocity flows, the power law $\langle F_x \rangle \sim L_p^1$ does not hold since our polymers are partially draining and we can fit the data using an empirical power law relation $\langle F_x \rangle \sim L_p^\alpha$ with $\alpha < 1.0$, as shown for the $V = 0.05$ case.

The average Stokes drag force $\langle F_x \rangle$ is plotted as a function of the relative extension H $(= h_x/L_p)$ in Figure 2.24; note that we included the data for different flow velocities $(V = 0.005 - 0.5)$, polymer lengths $(M = 5 - 100$, Figure 2.24 (a)) and tube diameters $(D_c = 8.4 - 30.6$, Figure 2.24 (b)). Surprisingly, all of our results fall onto a universal curve where the drag force is entirely defined by the relative extension H of the polymer chain (this is also the case if we remove the wall constraint and use periodic boundary conditions

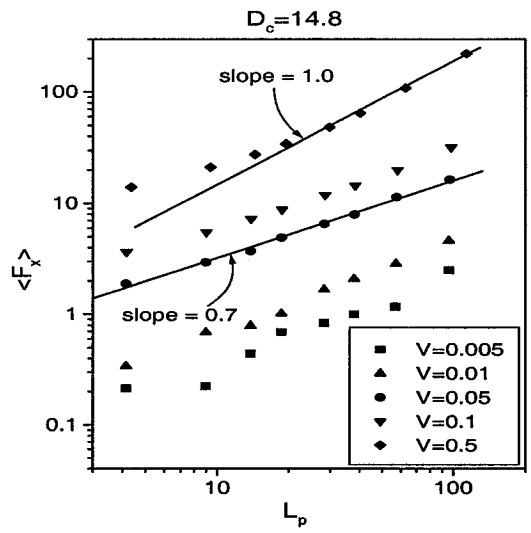

Figure 2.23: Average drag force vs. polymer contour length for $0.005 < V < 0.5$.

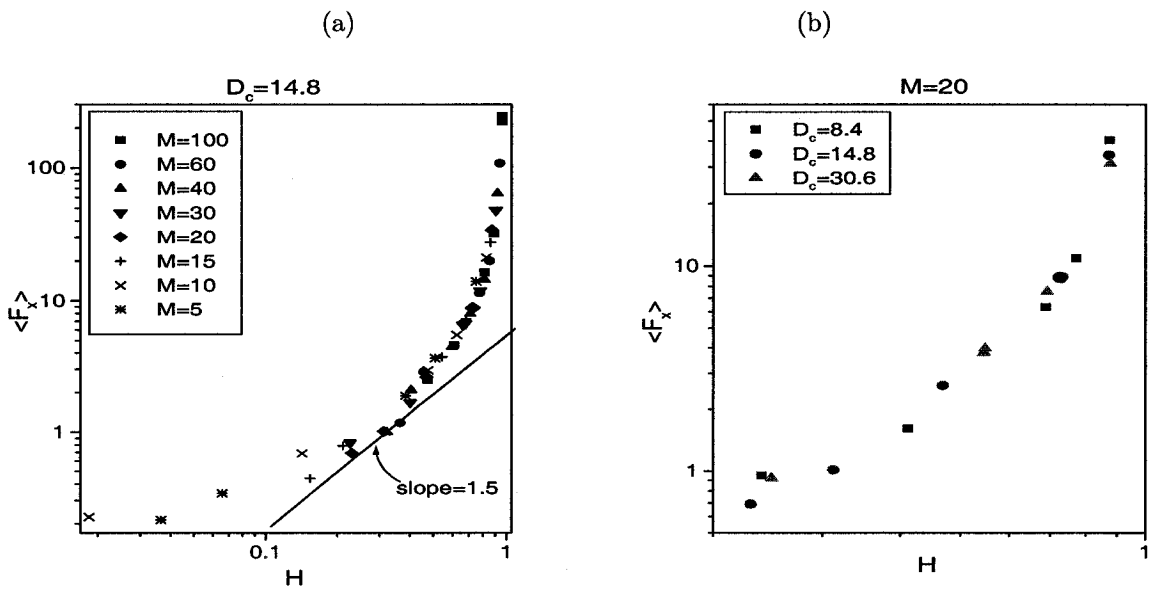

Figure 2.24: Average drag force $\langle F_x \rangle$ vs. average relative end-to-end H: (a) shows $\langle F_x \rangle$ for different polymer lengths ($5 < M < 100$) and flow velocities ($0.005 < V < 0.5$) for a tube diameter of $D_c = 14.8$, and (b) shows $\langle F_x \rangle$ for different capillary diameters ($8.4 < D_c < 30.6$) and flow velocities ($0.005 < V < 0.5$) for a polymer chain of length $M = 20$.

in all three directions; not shown). At low velocity ($V \rightarrow 0$), both $\langle F_x \rangle$ and H tend to zero which explains the noise in this limit. The thick solid line in Figure 2.24 represents the scaling law prediction of Brochard-Wyart for the "trumpet" conformation $F_x \sim H^{3/2}$ (using Eqs. 2.30 - 2.31). Note that the velocity range of the trumpet regime is expected to be quite narrow.

We have also plotted Marko and Siggia's [36] approximate interpolation formula (solid line), Eq. 2.25, and the FJC prediction [55] (dotted line), Eq. 2.21, in Figure 2.25. The Marko-Siggia approximation for a WLC does seem to provide a good approximation of our results. Howerver, this can be misleading, as we now show. The FJC prediction, on the other hand, is clearly unsatisfactory in spite of the fact that we did simulate a FJC and not a WLC.

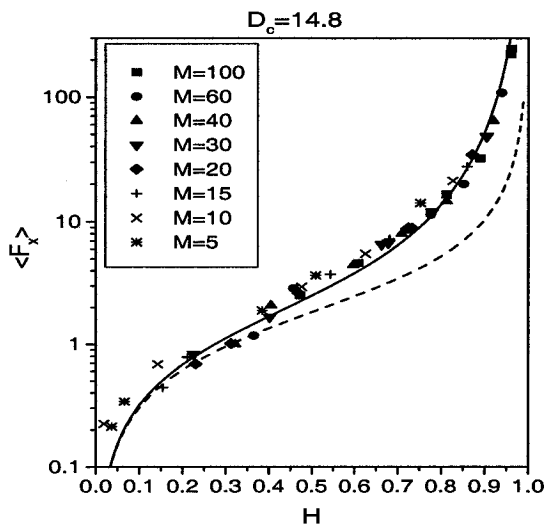

Figure 2.25: Average drag force $\langle F_x \rangle$ vs. average relative end-to-end distance H for different polymer lengths ($5 < M < 100$) and flow velocities ($0.005 < V < 0.5$) for a tube diameter of $D_c = 14.8$. Also plotted are the Marko-Siggia formula (solid line) and the FJC prediction (dotted line).

Figure 2.26 shows that our data (filled squares) actually follow a universal scaling law $(1 - H) \sim \langle F_x \rangle^{-0.60 \pm 0.01}$ for chain extensions greater than 50%, in disagreement with both

models, Marko-Siggia and FJC (see Eqs. 2.27). Interestingly in the case where the polymer chain is stretched by a constant force applied to both ends, we do observe the $\langle F_x \rangle^{-1}$ scaling law predicted by the FJC model (Figure 2.26, open triangles) and the $\langle F_x \rangle^{-0.5}$ scaling law for the WLC model (Figure 2.26, open circles). The worm-like chains were obtained by adding a bending energy $U_{wlc} = k_{wlc} cos\theta$ to the current MD algorithm, as described previously. Therefore, the fact that the Marko-Siggia model provides a better fit in Figure 2.25 is purely accidental.

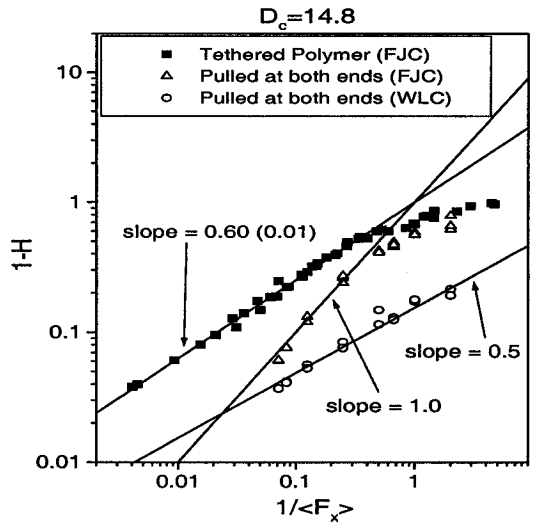

Figure 2.26: The plot shows the remaining extensibility $(1 - H)$ vs. the inverse drag force $1/\langle F_x \rangle$. The filled squares are for a tethered polymer pulled at constant velocity for different polymer lengths $(5 < M < 100)$ and flow velocities $(0.005 < V < 0.5)$ inside a tube diameter of $D_c = 14.8$. The open triangles are for a FJC polymer pulled at both ends for different polymer lengths and forces. The open circles are for a WLC polymer pulled at both ends for different polymer lengths and forces.

The conformational deformation changes the average friction coefficient $\xi \equiv \langle F_x \rangle / V$ of the polymer. In Figure 2.27, we plotted ξ vs the relative end-to-end distance H. More specifically, Figure 2.27 (a) shows the changes in the friction coefficient of different polymers inside a capillary of diameter $D_c = 14.8$ submitted to a variety of velocity flows. For small polymers, ξ remains relatively constant in spite of stretching: this is not surprising since

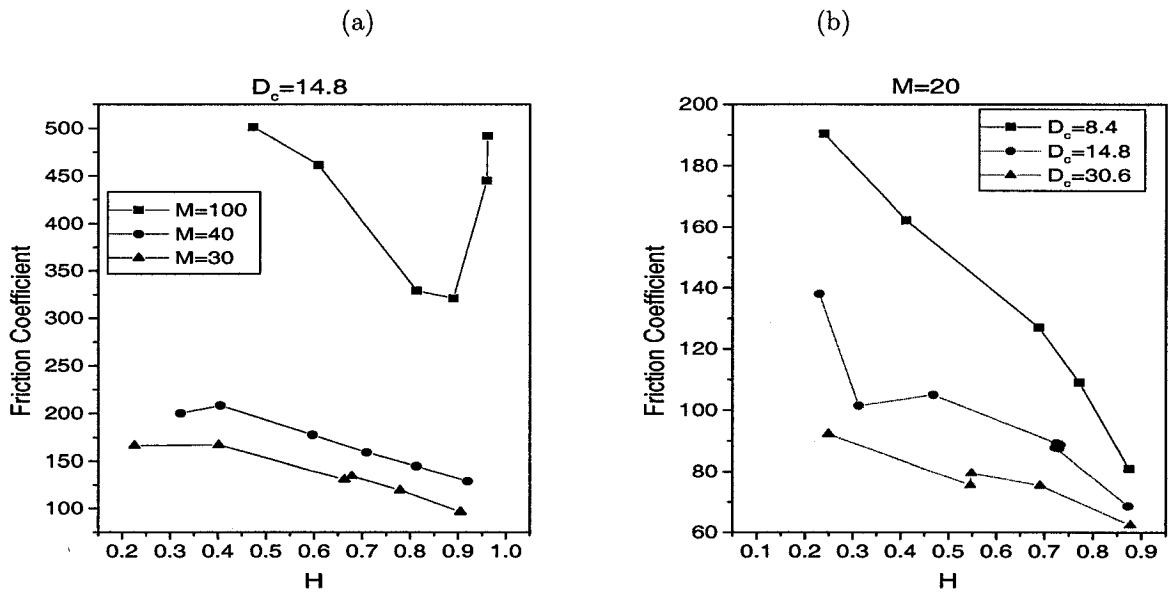

Figure 2.27: Polymer friction coefficient ξ vs. relative end-to-end distance H: (a) Different polymer lengths $30 < M < 100$ inside a capillary of diameter $D_c = 14.8$, (b) a polymer of length $M = 20$ for capillary diameters $8.4 < D_c < 30.6$.

the friction coefficients of a sphere ($\xi \sim R_F \sim L_p^{3/5}$) and a rod ($\xi \sim L_p/\ell n(L_p)$) do not differ much in such cases and the interactions with the walls are limited ($D_c > R_g$). For longer polymers (e.g., $M = 100$), the friction coefficient goes through a deep minimum (due to reduced interactions with the walls) before the stretching increases the friction to that of a rod of length $L \sim L_p \gg R_g$. Figure 2.27 (b) shows the effect of confinement on the friction coefficient. For small capillary diameters, the hydrodynamic interactions among the polymer segments are partially screened and the friction coefficient of the polymer increases dramatically, as predicted by Bakajin et al [20] (see section 2.4.4).

Cross-Correlations

The cross-correlation function $C_{F_x}^{\lambda_x}(t)$ between the drag force F_x and λ_x ($= h_x + a_x$, where a_x is the distance between the first monomer of the chain and the phantom bead) gives us interesting information about the relation between instantaneous drag forces and chain

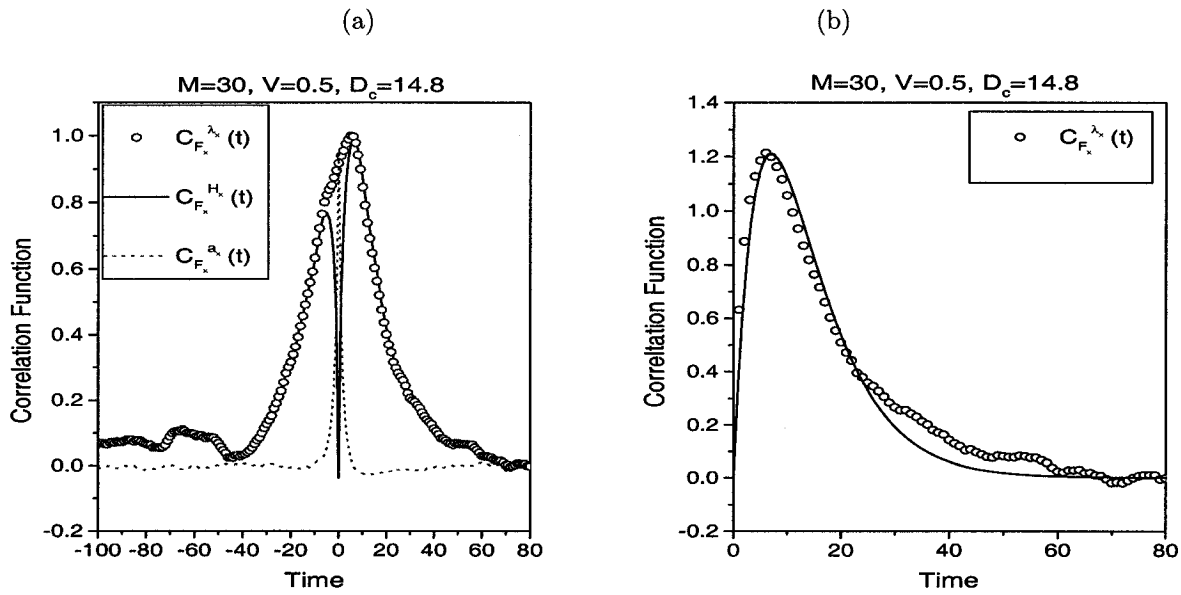

Figure 2.28: Cross-correlation functions for $M = 30$, $V = 0.5$ and $D_c = 14.8$.

conformations. This is shown in Figure 2.28 (a), open circles, for $M = 30, V = 0.5$ and $D_c = 14.8$. Note that

$$C_{F_x}^{\lambda_x}(t) = \langle F_x(0)\lambda_x(t)\rangle - \langle F_x\rangle\langle\lambda_x\rangle \tag{2.38}$$

and that t can be positive or negative. In fact, it is easy to show that $C_{F_x}^{\lambda_x}(t) = C_{F_x}^{h_x}(t) + C_{F_x}^{a_x}(t)$. We expect $C_{F_x}^{a_x}(t) \simeq \delta(t)$ since $F_x(t) = F_x(a(t))$. Both cross-correlations are plotted in Figure 2.28 (a): $C_{F_x}^{h_x}(t)$ is represented by the solid line and $C_{F_x}^{a_x}(t)$ by the segmented line. More specifically, $C_{F_x}^{h_x}(t)$ tells us (if $t > 0$) how the polymer chain reacts to a change in the drag force (or vice-versa if $t < 0$). Remarkably, we observe two unequal maxima at times $\pm\tau_c$. This suggests that the interactions that connect the fluctuations of the drag forces to those of the chain extension are not totally instantaneous.

The empirical function $C_{F_x}^{h_x}(t) \sim (t/\tau_c)e^{-t/\tau_c}$ provides a good fit of our data for both peaks (see Figure 2.28 (b)). Further, this function describes both the position of the maxima and the long-time decay of these cross-correlations with a single time τ_c. This new relaxation time τ_c increases with the velocity flow and also increases linearly with the polymer length M as shown in Figure 2.29. Unfortunately, we were unable to determine the exact position of the maxima for lower velocity flows in spite of the long simulation times used ($6 \times 10^7\tau$).

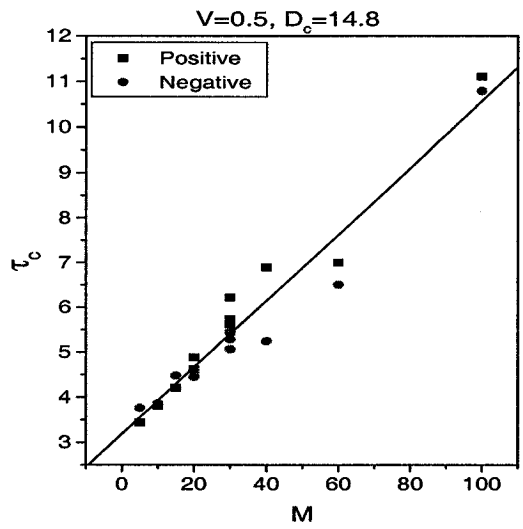

Figure 2.29: The characteristic delay time τ_c vs. the molecular size M for $V = 0.5$ and $D_c = 14.8$.

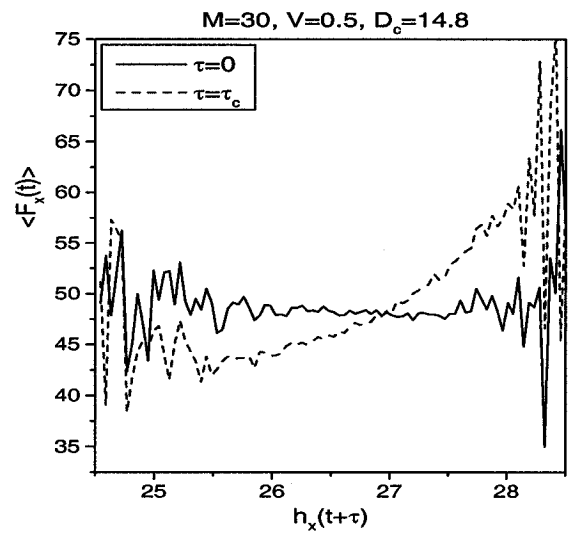

Figure 2.30: Mean drag force $\langle F_x(t)\rangle$ vs. the instantaneous end-to-end distance $h_x(t+\tau)$ for M=30, V=0.5 and D_c=14.8 and where $\tau = 0$ and τ_c.

These results demonstrate that although $\langle F_x \rangle \sim \langle h_x \rangle$, a fluctuation in one of these variables only affects the other after a time delay $\sim \tau_c(M, V)$. To verify this result, we also plotted the average drag force $\langle F_x \rangle$ vs the instantaneous value of $h_x(t + \tau)$ (Figure 2.30). There is no correlation between the two variables if $\tau = 0$. On the other hand, when $\tau = \tau_c$, we do find a clear correlation between the force and the end-to-end distance.

2.5.2 Worm-Like Chains

In this section, we investigate the WLC model. The diameter of the capillary is kept at $D_c = 14.8$ whereas its length varies between $47.5 \leq L \leq 190$ depending on the contour length $L_p(M)$ of the polymer ($5 \leq M \leq 100$) being pulled. The polymer chain link potential is the sum of the modified Lennard-Jones U_{tlj}, the FENE U_F and finally the WLC U_{wlc} (Eq. 2.14) potentials. A value of $k_{wlc} = 10.0$ was used during the simulation to obtain a worm-like chain behaviour [100]. Furthermore, for such a value of k_{wlc}, the persistence length was found to be $\ell_p \approx 9.97$ (which is ≈ 7.55 times larger than for the FENE model, Eq. 2.18).

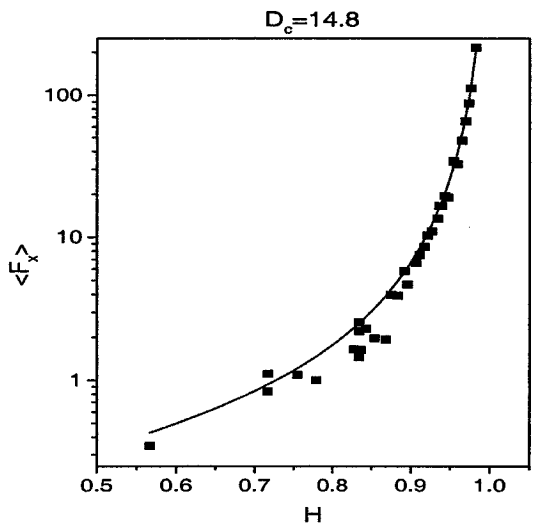

Figure 2.31: Average drag force vs. relative extension for the WLC for $10 < M < 100$ and $0.005 < V < 0.5$. The solid represents the Marko-Siggia approximation.

The average Stokes drag force $\langle F_x \rangle$ is plotted as a function of the relative extension H in Figure 2.31. We included the data for different flow velocities ($V = 0.005 - 0.5$) and polymer lengths ($M = 10 - 100$). The universal behaviour of the drag force (as a function of H) still remains true for the WLC model. The thick solid line in Figure 2.31 represents the Marko-Siggia approximation with the fitted Kuhn length $b_k \approx 7.7 \pm 0.1\ b$ as expected, i.e., similar to the ratio of the persistence length discussed above. One can then calculate the effective polymer length $M_k = L_p/b_k$ used in our simulations; the result, $1 < M_k < 13$, indicates that we had very small polymers indeed!

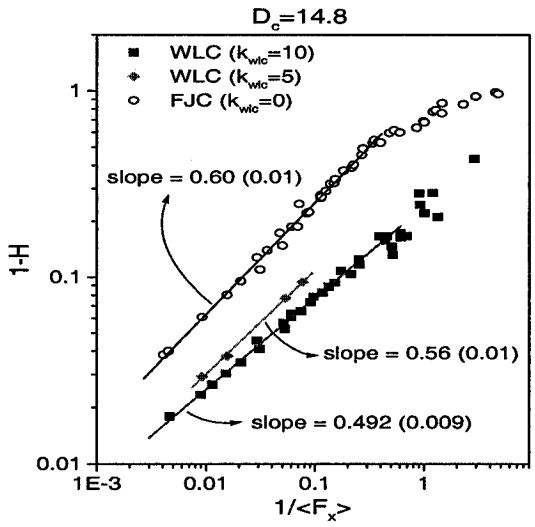

Figure 2.32: Average remaining extension $1 - H$ vs. the inverse of the drag force for the WLC model.

Figure 2.32 shows that the WLC data (filled squares) follow the universal scaling law $(1 - H) \sim \langle F_x \rangle^{-0.492 \pm 0.009}$ for chain extensions greater than 50%, in agreement with the Marko-Siggia model. Interestingly, in the case where we reduced the bending parameter k_{wlc}, the exponent slowly increases from the Marko and Siggia value $\frac{1}{2}$ to our previous FJC value of $\frac{3}{5}$. These results clearly indicate that the current theory regarding mechanical stretching of polymer chains cannot be applied directly to the case of hydrodynamic stretching, especially in the FJC limit (flexible chains).

2.5.3 Liquid Flow Analysis

We now investigate the properties of the solvent particles surrounding the tethered polymer being pulled inside a capillary of diameter $D_c = 14.8$. Figure 2.33 shows a vector plot of the velocities of the solvent particles inside (with respect to the wall) and outside (with respect to the phantom bead) the polymer for the FJC model. In this case the polymer length is $M = 40$ and is pulled at velocity $V = 0.1$. Note that $x = 0$ indicates the position of the phantom bead. One can see that the liquid particles get trapped inside the polymer conformation and that the polymer is not perfectly free-draining. The maximum solvent velocity is about 37% that of the moving polymer chain.

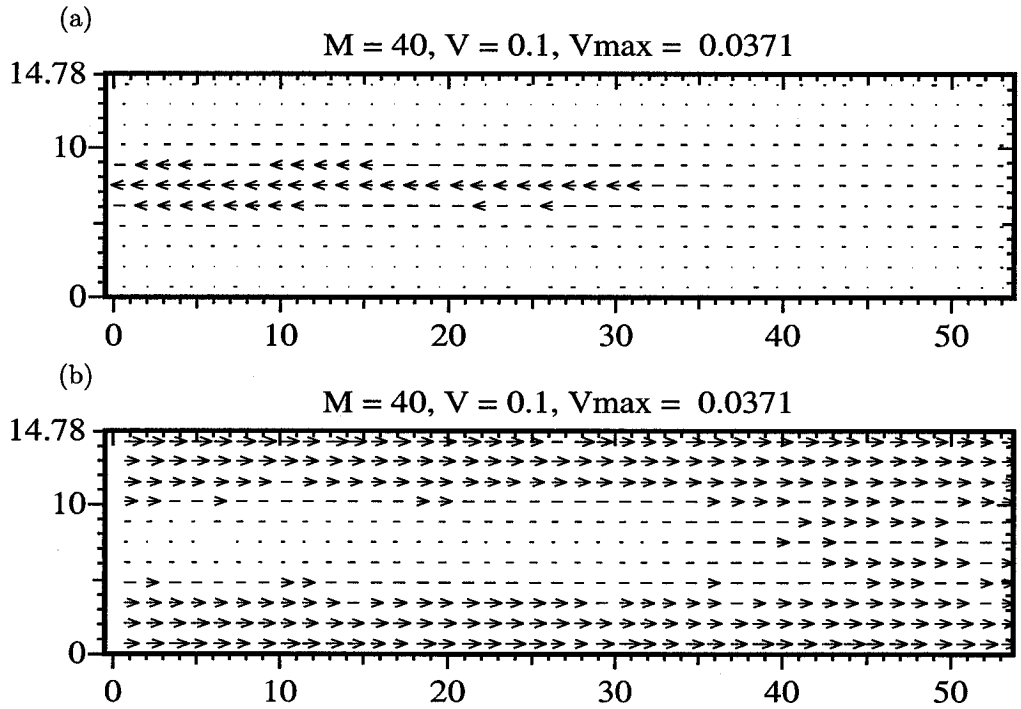

Figure 2.33: Vector plot of the velocity of the solvent particles surrounding a FJC polymer of length $M = 40$ pulled at a velocity $V = 0.1$ along the tube axis. A) represents the velocities of the solvent particles with respect to the wall whereas B) represents their velocities with respect to the phantom bead.

Figure 2.34 shows the average velocity of the solvent particles $\langle V_s(x) \rangle$ along the tube axis as a function of the radial position r, x being the distance from the tethered end of the polymer, for a polymer of length $M = 40$ and velocities $V = 0.05$ and 0.1. The average

$\langle V_s(x)\rangle$ is taken over an axial slice of width $dx = 2^{1/6}$ along the tube axis and over a radial width $dr = 2^{1/6}$. We have seen previously that at such high velocities V, the polymer is either in a "trumpet" or in a "stem and flower" conformation (see Figure 2.13). We observe that the velocity of the solvent decreases toward zero (in a conic shape instead of a parabolic one) as we get closer to the wall of the capillary (non-slip walls). At low velocities V, the velocity of the solvent decreases gradually along the polymer while at higher velocities V, the solvent velocity profile remains constant until it reaches the free end of the polymer. Note that the velocity of the solvent behind the polymer is non-zero.

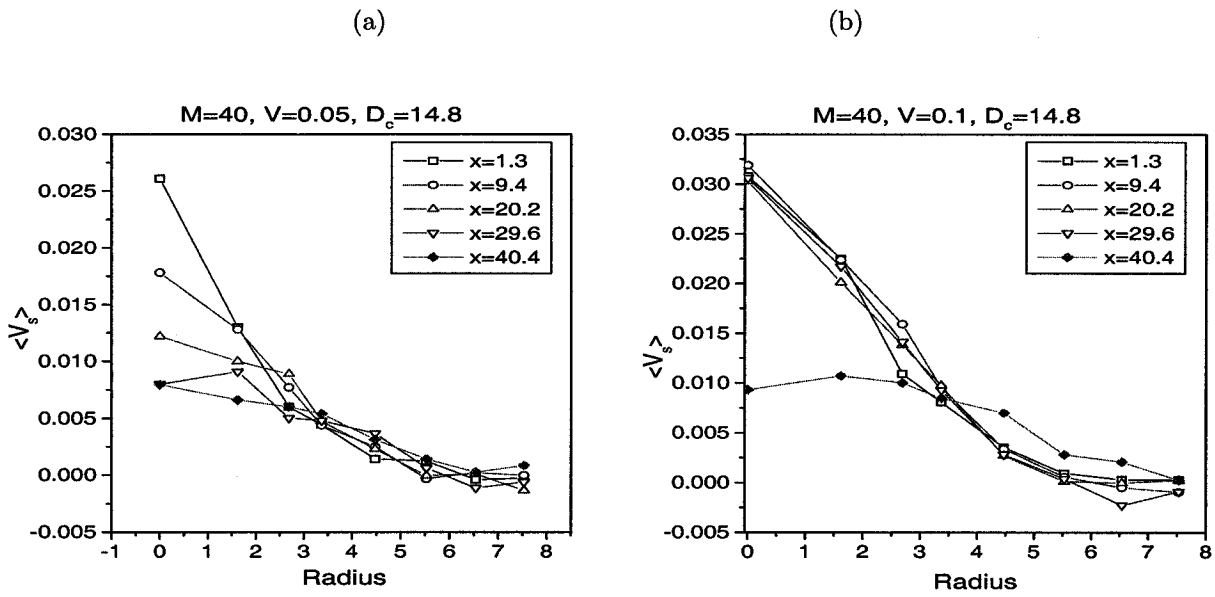

Figure 2.34: Average velocity $\langle V_s(x)\rangle$ as a function of the tube radius r for a polymer of length $M = 40$ and pulled velocities of (a) V=0.05 and (b) 0.1. The mean end-to-end distances of these two chains are $h_x(40)$= 27.4 and 31.1, respectively.

This is very similar to a shear flow problem where the different parts of the polymer are subject to different flow velocities. We believe that this effect is responsible for the power law $1 - H \sim F^{-0.6}$ obtained earlier.

Figure 2.35 shows a vector plot of the flow velocities of the solvent inside and outside the polymer for the WLC model ($M = 40$ and $V = 0.1$). Again, one can see that the liquid particles get trapped inside the polymer and that the polymer is not free-draining.

To compare the flow velocities of the solvent particles between a FJC and WLC polymer,

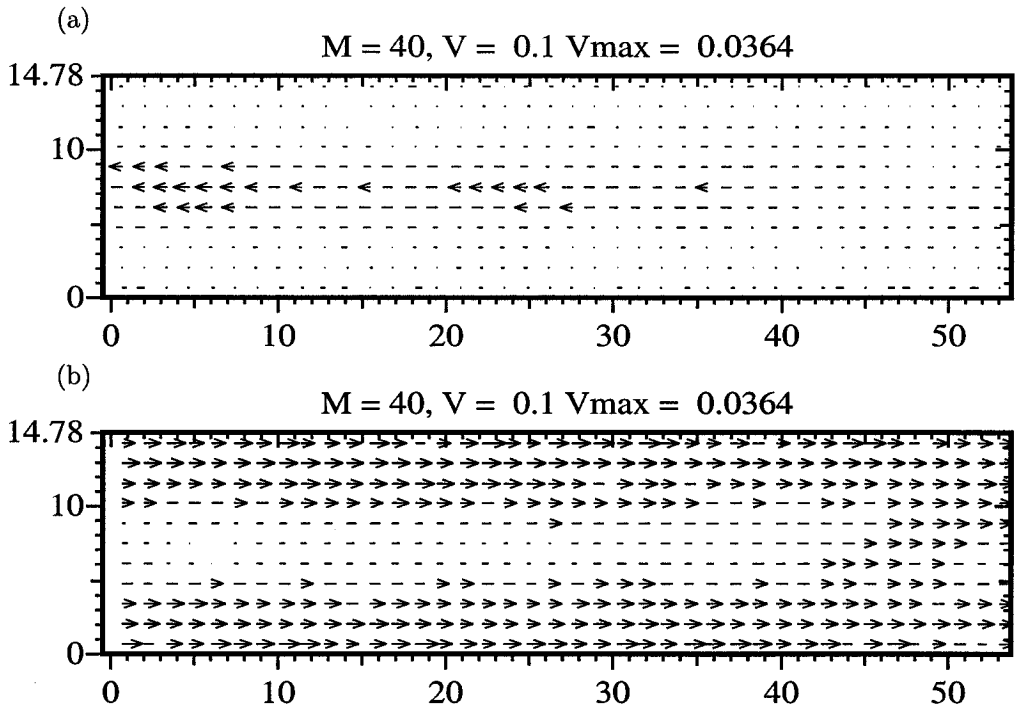

Figure 2.35: Vector plot of the velocity of the solvent particles surrounding a WLC polymer of length $M = 40$ pulled at a velocity $V = 0.1$ along the tube axis. A) represents the velocities of the solvent particles with respect to the wall whereas B) represents their velocities with respect to the phantom bead.

we plotted the average velocity $\langle V_s(x) \rangle$ as a function of the radial position r for two different values of x in Figure 2.36. The flow pattern is similar for both cases but the magnitude of the flow velocity is higher in the case of the FJC polymer where the solvent particles get trapped more strongly inside the chain.

2.6 Discussion

MD simulations allow the user to fully determine and control all variables of the simulation and to measure a wide variety of properties about the fluid and the polymer. We have shown that such an approach can successfully answer questions that can hardly be tackled from a purely macroscopic viewpoint. In the present case, the presence of the walls leads to conformations that do not follow the theoretical predictions for single polymers in free-solution.

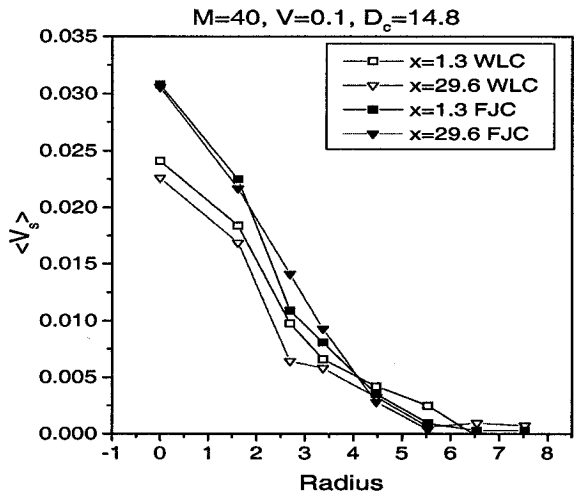

Figure 2.36: Average velocity $\langle V_s(x) \rangle$ as a function of the radial position r for a polymer of length $M = 40$ and a velocity $V = 0.1$.

On the other hand, we were able to reproduce qualitative features of experiments that used DNA molecules in spite of the modest length of our simulated chains. We have also shown that our results compared well with the ones obtained by Cheon et al. [34]. Unfortunately, we were unable to confirm Brochard-Wyart [39] theoretical predictions, probably due to the limited chain lengths used in our simulation.

We found that the total drag force exerted by the polymer gives a universal function when plotted against the relative extension, independent of the degree of confinement. We have also shown that the polymer extension for a FJC does not follow previous predictions at high extension under such conditions; instead we found $(1 - H) \sim F^{-0.6}$. This scaling law may be due to the limited length of the polymer chains used in our simulations or to the creation of a shear flow around the polymer where the solvent trapped inside the polymer could go at a different velocity than those surrounding it. This can easily affect the power law $(1 - H) \sim F^{-1}$ found in mechanical stretching. Compact FJC conformations capture the solvent more tightly (are less free-draining) and thus affect the local flow more than WLC conformations. The resulting local flow clearly shows a strong shear component, not

unlike the one assumed by Ladoux et al. [37]. These authors investigated a similar problem and predicted that the relative chain stretching should follow the scaling law $(1-H) \sim \dot{\gamma}^{-2/3}$ for a FJC polymer, where $\dot{\gamma}$ is the shear rate. These results clearly show that non-uniform flows can explain a lower exponent. The fact that we recover the correct FJC prediction when both ends of our FJC chains are pulled, and the WLC predictions for both mechanical and hydrodynamic forces, suggests that our FJC results are indeed due to effects that are missing in current theories. A self-consistent model of FJC stretching in a flow is thus needed.

The utility of MD simulations in the study of the dynamics of fluids and polymers had been recognized earlier by a number of authors. In this chapter, we calculated the cross-correlation function $C_{F_x}^{h_x}(t)$ between the drag force and the end-to-end distance in the axial direction. The results give two maxima at $t = \pm\tau_c$, i.e., a delay exists between the applied force and the extension of the polymer with $\tau_c(M, V) \sim M$. This means that modelling of high frequency (non steady-state) phenomena would require MD simulations. Simulations using the Oseen tensor to approximate instantaneous hydrodynamic interactions do not take into account such delays.

Obviously, it is easy to modify our MD algorithm to study a wide range of related problems, including the deformation of a polymer pulled with a constant force. For instance, one can modify the interactions between the solvent and the polymer to model a poor solvent, or even between the walls (adsorbing or repulsive) and the polymer or study the collision process of a single polymer with an obstacle. Similarly, polymeric solvents or/and branched probe polymers would be of great interest. Finally, it should be noted that MD simulations allow us to study microscopic properties such as the nature of the fluctuations or the behaviour of the fluid.

Chapter 3 Reptation Dynamics in a Random Energy Landscape: Annealed Disorder [1]

3.1 Introduction

In the original framework of the reptation model [9, 101, 102, 103, 104], the diffusion coefficient of a primitive chain made of M segments is predicted to scale like $D \sim (R_g)^2/\tau$, where $R_g \sim M^\nu$ is the radius of gyration of the polymer, ν is Flory's exponent and τ is the disengagement time (which scales like M^3). In a melt, one has $\nu = \frac{1}{2}$ and the reptation model predicts $D \sim 1/M^2$ (for $M \gg 1$) [105, 106]. In a gel, $\nu = \frac{3}{5}$ because of the absence of excluded volume screening, and the model then predicts the slightly weaker dependency $D \sim 1/M^{9/5}$. Empirical scaling laws of the form $D \sim 1/M^{2+\alpha}$, with $\alpha \sim 0.7 - 0.8$, have been reported for the diffusion coefficient of linear polystyrene in poly(vinyl methyl ether) gels [107]. Positive values of α are obviously inconsistent with the reptation model.

Baumgartner and Muthukumar [108, 109] suggested the existence of entropic trapping effects wherein the distribution of pore sizes leads to entropic barriers that slow down the motion of the polymer. They showed that when the mean "pore" size $\bar{a}$ of a quenched random medium (not a melt) is comparable to R_g, the polymer molecule prefers to reside into the largest pores of the system ($a > \bar{a} \cong R_g$) to maximize its entropy. Since these pores are connected by narrower channels of width $< R_g$, the long-range motion of the polymers is through a "hopping" process where the channels act like "entropic barriers". The physics of this problem is similar to that of a particle moving in a system with a rough energy landscape [110, 111]. The diffusion coefficient D then decreases very quickly with molecular size M; scaling arguments based on an energy barrier model in fact predict that the dependence should be an exponential instead of a power law [112]. However, if we

[1] The simulation algorithm described in this Chapter was developed in reference [119]. This Chapter presents a deeper analysis of the simulation results for the diffusion coefficient and the electrophoretic velocity of polyelectrolytes in random energy landscapes which was missing in reference [119]. This Chapter is also a necessary preamble to Chapter 4.

fit simulation data with a power law (which often provides a good fit because the range of polymer molecular sizes accessible by computer simulation is fairly narrow), we find that the additive exponent α increases from $\alpha = 1-2\nu \leq 0$ (for periodic arrays of obstacles) to values exceeding $1/2$ for very disordered environments [112, 113]. Entropic trapping has therefore been invoked to explain anomalous diffusion data [107] showing large positive values of α. Recent computer simulations have demonstrated that entropic trapping disappears when the gel fibers stop forming a percolating cluster that limits the long-range diffusion of the polymer [113].

Similar results were also observed for gel electrophoresis (GE) of polyelectrolytes. At low electric field, the electrophoretic mobility follows the simple scaling law $\mu \sim 1/M$, a prediction of the biased reptation model (BRM) in excellent agreement with a large body of experimental data [54, 114, 115]. Experimental results from Calladine et al. [62] and Arvanitidou et al. [116] have shown that the low-field electrophoretic mobility of DNA molecules can decrease as fast as $\mu \sim 1/M^3$ for intermediate DNA sizes. Mayer et al. [117] found a $1/M^{1.6}$ dependence for small DNA molecules. More recently, Rousseau et al. [118] reported the results of a detailed study of the low field polyacrylamide gel electrophoresis of single-stranded DNA sequencing fragments. These authors observed regimes where $\mu \sim 1/M^{(1+\alpha)}$, with $0 \leq \alpha \leq 0.4$, when the field intensity was lower than about 30 V/cm and the gel concentration larger than about 3%. High gel concentrations and low field intensities are required to observe finite values of the exponent α. None of these results agree with the $1/M$ law predicted by the standard BRM.

The reptation model assumes that the energy of the chain does not depend on its spatial position or it assumes that the environment provides a uniform and purely steric constraint that forces the polymer to move head first like a snake in a dense plantation. This may not always be the case, however, especially in a disordered gel where the distribution of pore sizes may be quite broad. Moreover, if the gel material and the reptating probe molecule are of different chemical compositions, one may also have enthalpic interactions (attractive or repulsive forces between the chain and the medium). Both of these effects will then lead to a non-uniform energy landscape that may greatly affect the reptation dynamics of the chain. Indeed, large values of α were observed [113] even when $R_g \gg \bar{a}$.

Zimm and Lumpkin (ZL) [61] proposed a modified reptation model to take into account

local interactions between the environment and the reptating polymer. They modelled the reptation of the polymer inside an irregular matrix using a modified BRM where the chain interacts locally with the matrix. Their calculations predicted an exponential decrease of the diffusion coefficient with molecular size M in the zero-field limit, a sign of strong trapping in low-energy regions. As for the electrophoretic mobility, they did indeed obtain a function that decreased much faster than the predicted $\mu \sim 1/M$ relation. However, the nature of the energy landscape was not clear because the mathematical approach was coarse-grained and only considered chain hopping over length scales comparable to the end-to-end vector h_x of the chain in the field direction.

In reference [119], we introduced a microscopic version of the reptation model in the presence of local interactions. The model studies the limit where the correlation length λ of the matrix is shorter than $\bar{a}$, such that the local energies associated with the reptation segments are uncorrelated. For uncorrelated local energies in an annealed gel, the model essentially recovered the predictions of the standard reptation model with an increase effective viscosity of the medium. The model also differs from the one proposed by ZL in that the distance migrated by the polymer during the hopping process is given by $\bar{a}$ (which is actually the proper length scale for the reptation model) instead of h_x. In this Chapter, the analysis of the results presented here go well beyond those reported in [119] and are a necessary preamble to Chapter 4 for the quenched model with long-range correlation.

3.2 The Biased Reptation Model

The main predictions of the standard reptation model can be obtained from the BRM if used in the zero-field limit ($E \rightarrow 0$). For this reason, the calculation of the jumping rates and local biases is done for the BRM, and the $E \rightarrow 0$ limit will be taken later when required.

The topological constraints created by the gel fibers form an imaginary tube with impenetrable walls in which the polymer moves [9, 101, 102, 103, 104, 112, 120]. In practice, the polymer is modelled as a "primitive" chain of M effective "reptation segments" of length $\bar{a}$ and effective charge of q which are not allowed to bend away from the tube axis. The dynamics of the polymer inside this imaginary tube is characterized by two assumptions: 1) the primitive chain, and consequently the reptation tube, have a fixed constant contour

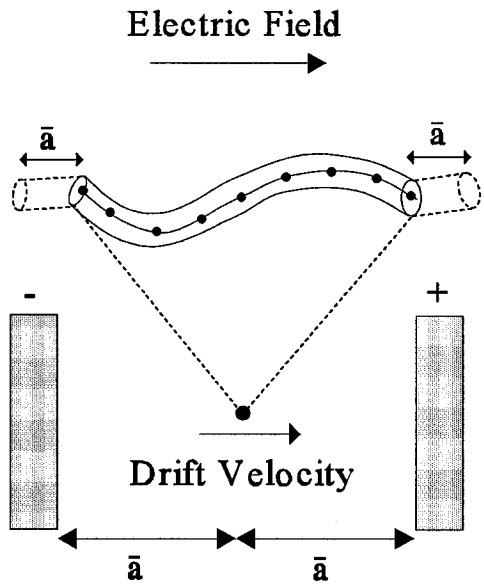

Figure 3.1: The tube model and its equivalent one-dimensional point-like particle problem. An elementary jump of length $\bar{a}$ along the tube axis is completed when the particle is "absorbed" by one of the walls.

length $L_p = M\bar{a}$; and 2) the only allowed motion for the chain is along the tube axis. Therefore, the motion of the polymer is represented by a series of discrete displacements of length $\bar{a}$ as seen in Figure 3.1. In the absence of electric forces ($E = 0$), the motion of a polymer is due solely to random thermal motion and the probabilities of jumping toward either end of the tube are equal.

The presence of an electric field $\mathbf{E} = E\hat{\mathbf{x}}$ leads to a net force acting along the tube axis of the polyelectrolyte chain (the transverse component of the total force $Q\mathbf{E}$ does not play a role because of the rigid-tube assumption). In this case, the probability $p_{\pm}$ for the chain to jump towards the $\pm$ end of the tube (see Figure 3.1) is given by [121]

$$p_{\pm}(h_x) = \frac{1}{1 + e^{\mp 2\delta(h_x)}} \tag{3.1}$$

where we define the following dimensionless variables

$$\begin{aligned} \delta(h_x) &= \epsilon \frac{h_x}{\bar{a}} \\ \epsilon &= \frac{qE\bar{a}}{2k_BT} \\ q &= Q/M \end{aligned} \tag{3.2}$$

where δ is the conformation-dependent bias factor, ϵ is the scaled electric field intensity and Q is the total electric charge of the chain. Once we have selected the end towards which the polymer will jump (using Eq. 3.1), the orientation Θ ($0 \leq \Theta \leq \pi$) of the new end-segment with respect to the field axis is chosen using the probability distribution function [121, 122]

$$P(\Theta)d\Theta = \frac{1}{2}\frac{\epsilon}{sinh(\epsilon)} sin(\Theta) d\Theta e^{\epsilon cos(\Theta)}. \tag{3.3}$$

In the zero-field limit, Eq. 3.3 reduces to $P(\Theta)d\Theta = \frac{1}{2}d[cos(\Theta)]$, as expected for an isotropic system.

The displacement of the chain inside the tube can be compared to the diffusion of a particle halfway between two absorbing walls (see Figure 3.1). The completion of a discrete jump by the chain simply corresponds to the absorption of the point-like particle by one of the walls. The chain moves in response to Brownian motion (with a curvilinear diffusion constant $D_c \sim 1/M$, as in the Rouse model since the hydrodynamic interactions are screened by the gel) as well as to the field-induced drift (with an instantaneous curvilinear velocity $V_c \sim h_x E$). We replace this continuous motion by biased jumps of constant length $\bar{a}$. It is actually the lack of intratube degrees of freedom that allows us to replace the primitive chain by a point-like object to determine its basic dynamical properties. However, one must keep track of the long-time memory effects that are typical of reptation dynamics, especially if a field is applied. Using this analogy, we are able to derive the mean time required to jump over a distance $\bar{a}$ (in either direction) and its second moment [121, 124]

$$\begin{aligned} \frac{t_{\pm}(h_x)}{\tau_B} &= \frac{tanh[\delta(h_x)]}{\delta(h_x)} \\ \frac{t_{\pm}^2(h_x)}{\tau_B^2} &= \frac{1}{\delta^2(h_x)} \left[tanh^2[\delta(h_x)] - sech^2[\delta(h_x)] + \frac{tanh[\delta(h_x)]}{\delta(h_x)} \right] \end{aligned} \tag{3.4}$$

where $\tau_B = \bar{a}^2/2D_c \sim M$ is the Brownian time ($\epsilon = 0$) necessary for the diffusion of the chain over a curvilinear distance $\bar{a}$. Using these equations, we can investigate polyelectrolyte

gel electrophoresis (for $\epsilon > 0$) or normal reptation (for $\epsilon = 0$) using computer simulations or analytical calculations.

In the zero-field limit ($\epsilon \to 0$), we can calculate the diffusion coefficient using the Doi and Edwards approach [101] to obtain,

$$D(M, \epsilon \to 0) = \lim_{t\to\infty} \frac{\langle [\mathbf{r_{cm}}(t) - \mathbf{r_{cm}}(0)]^2 \rangle}{6t} = \frac{D_c}{3(M+1)} \sim \frac{1}{M(M+1)} \tag{3.5}$$

where $\mathbf{r_{cm}}(t)$ is the position of the center of mass at time t and $D_c = \bar{a}^2/2\tau_B \sim M^{-1}$. In passing, we found that the well-known result $D \sim (4M+1)/(4M^2)$ given in ref. [101] is actually incorrect due to several minor mistakes in the derivation.

For low field intensities ($0 < \epsilon < 1$), approximate analytical expressions for the electrophoretic velocity $V(M, \epsilon)$ and the diffusion coefficient $D(M, \epsilon)$ were obtained for the BRM. The electrophoretic velocity showed three regimes [121, 122, 124]:

$$\begin{aligned} V(M,\epsilon) &\cong \tfrac{\bar{a}}{\tau_B}\tfrac{\epsilon}{3} \sim M^{-1}E, && M\epsilon^2 < 1 \\ &= \textit{shallow minimum}, && M = M_{min} \cong 14/\epsilon^2 \\ &\cong \tfrac{\bar{a}}{\tau_B}\tfrac{M\epsilon^3}{9} \sim M^0E^3, && M\epsilon^2 \gg 14. \end{aligned} \tag{3.6}$$

The unexpected shallow minimum was first seen in computer simulations [114] and later observed experimentally [114].

The Nernst-Einstein relation between the electrophoretic velocity $V(M, \epsilon)$ and the diffusion coefficient $D(M, \epsilon)$ reads

$$\frac{D(M,\epsilon)}{V(M,\epsilon)} = \frac{k_BT}{MqE} = \frac{\bar{a}}{2M\epsilon}. \tag{3.7}$$

This relation predicts that we should have $D \sim M^{-2}$ and $D \sim M^{-1}$ in the small and large size limits mentioned in Eq. 3.6. Instead, it was found that the diffusion coefficient (in the field direction) decreases successively like M^{-2} and $M^{-1/2}$, goes through a broad maximum and finally reaches a plateau value for large molecular sizes. A detailed analysis of the BRM demonstrates that the relevant scaling laws are [124]

$$\begin{aligned} D(M,\epsilon) &\cong D_c\tfrac{1}{3(M+1)} \sim M^{-2}E^0, && M < M_d \equiv 1.68\epsilon^{-2/3} \\ &\cong D_c\tfrac{\epsilon\sqrt{2M}}{3\sqrt{3\pi}} \sim M^{-1/2}E, && M_d < M < \epsilon^{-2} \\ &\cong D_c\tfrac{M\epsilon^2}{9} \sim M^0E^2, && M > \epsilon^{-2} \\ &= \textit{broad maximum}, && M = M_{max} \cong 28\epsilon^{-2} \cong 2M_{min}. \end{aligned} \tag{3.8}$$

The non-linear effects predicted by the BRM invalidate the Nernst-Einstein relation when $M > M_d \cong \epsilon^{-2/3}$ or before the mobility is affected, which occurs only for $M > \epsilon^{-2} > M_d$.

For very flexible polyelectrolytes, the BRM does not describe appropriately the orientation process. It was found that the orientation term was dominated by another phenomenon arising from the coupling between the fast fluctuations of the chain ends and the local chain orientation [115, 125, 126]. In this thesis, we will follow the original BRM in order to compare our finite-field results with those obtained by Zimm and Lumpkin [61]. The effects of the fluctuations (for flexible polyelectrolytes) and orientation coupling (for stiff polyelectrolytes) are left for future investigations.

3.3 Reptation with Random Fluctuation: an Annealed Matrix

The topology of the gel may affect the dynamics of reptating polymers. For instance, if a polymer moves inside a narrow, curved space, either the gel deforms to let the polymer through or the polymer bends, or both occur. In this situation, energy is required to perform the bending of the polymer or the deformation of the gel which can lead to local energetic effects. Similarly, one may have direct interactions between the fibers and the segments of the polymer (e.g., random electric charges on the gel fibers may lead to local repulsive or attractive forces). Local entropic effects may also affect the dynamics of long reptating polymers in inhomogeneous systems.

To simulate such local energetic effects, we associate with pore i ($i = 1, ..., M$) an energy g_i (in units of k_BT) which remains fixed as long as a primitive segment occupies it. We further defined the correlation length of the matrix to be shorter than the segment length $\bar{a}$ of the reptation segment so that there is no correlation between the various g_i's. This corresponds to an annealed gel since we keep no memory of the energy of a pore once the chain end segment has left it. The case of a quenched and correlated gel will be treated in Chapter 4. The distribution function $w(g_i)$ for the local energies g_i follows a Gaussian probability distribution function with a zero mean and a standard deviation g:

$$w(g_i) = \frac{1}{\sqrt{2\pi g^2}} e^{-\frac{g_i^2}{2g^2}}. \tag{3.9}$$

The Gaussian distribution is cut beyond $2g$ in order to avoid exceedingly large trapping

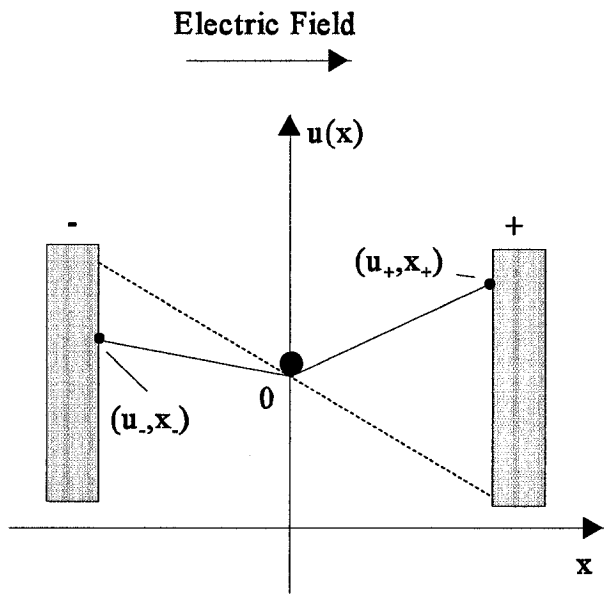

Figure 3.2: A point-like particle in an external field and in the presence of disorder. The net potential $u(x)$ is shown for $g = 0$ (dashed line) and $g \neq 0$ (solid line). The walls are at $x_+ > 0$ and $x_- < 0$.

times (the distribution function decays very quickly for $|g_i| > 2g$).

The motion of the polymer inside the imaginary tube can be represented by the diffusion of a particle between two absorbing walls as seen in the previous section (see Figure 3.1). The one-dimensional space of the particle problem is equivalent to the curvilinear tube axis, not the field axis. Therefore, when the chain jumps towards the $\pm$ end of the tube, the particle is effectively absorbed by the $\pm$ wall. The presence of a constant and uniform electric field (including $\epsilon = 0$) leads to a longitudinal drift velocity, $V_c(\epsilon) \geq 0$. This drift velocity can be derived from the potential function U as $V_c = -\nabla U/\xi$, where $\xi \sim M$ is the curvilinear friction coefficient of the polymer in its tube. Figure 3.2 show a uniform electric field (dotted line) where $U_\pm = \mp 2\delta k_B T$ is simply the value of the potential at the $\pm$ wall. The scaled potential is simply $u_\pm = \mp 2\delta$.

The effect of the local energies g_i when added to the electric field is represented as a random perturbation on the local potentials $u_\pm$ (Figure 3.2, solid line). We assume that the potential $u(x)$ is linear between the initial position and the "wall" (Figure 3.2); this

simplifying assumption can easily be changed to study other models. The new values of $u_\pm$ are simply the sum of the electric potential ($\mp 2\delta$) and the net change of the chain's total free energy $\Delta g_\pm$ during a jump of length $\bar{a}$ in the $\pm$ direction, i.e.

$$u_\pm = \mp 2\delta + \Delta g_\pm \ . \tag{3.10}$$

When the chain completes a jump in the $\pm$ direction, the $\mp$ end-segment disappears, while a new end-segment is created at the $\pm$ end of the tube. Since all the internal chain segments slide, the net energy difference comes solely from the two ends (there is no net change in energy elsewhere along the chain). Therefore, $\Delta g_\pm$ is actually the difference in energy between the new end-segment and the destroyed end-segment. We expect it to scale like $\Delta g_\pm \sim M^0$. In ZL's article [61], the coarse-graining approximation effectively led to $\Delta g_\pm \sim h_x \sim M^{1/2}$.

The mean first-passage time and the probability that the particle (chain) will first reach a given wall (end of the tube) can be derived using stochastic methods (more precisely, the Fokker-Planck equation). The mean exit time $\langle T \rangle$ of a particle initially at position x (such that $x_- \leq x \leq x_+$) exits through x_- is formally given by [119]

$$\langle T(x_-, x) \rangle = 2 \left[\frac{1}{p_{x_-}(x)} \int_x^{x_+} \frac{dy}{\Psi(y)} \int_{x_-}^{y} \frac{dy' \Psi(y') p_{x_-}(y')}{B(y')} - \int_{x_-}^{x_+} \frac{dy}{\Psi(y)} \int_{x_-}^{y} \frac{dy' \Psi(y') p_{x_-}(y')}{B(y')} \right] \tag{3.11}$$

where $\Psi(y)$ is defined as

$$\Psi(y) = exp \left\{ \int_{x_-}^{y} dx' \frac{2A(x')}{B(x')} \right\} . \tag{3.12}$$

Here, $A(x)$ is the drift velocity and $B(x)$ is a diffusion coefficient. Similarly, the mean exit time, given that the particle starting at x exits through x_+ is

$$\langle T(x_+, x) \rangle = 2 \left[\int_{x_-}^{x_+} \frac{dy}{\Psi(y)} \int_{x_-}^{y} \frac{dy' \Psi(y') p_{x_+}(y')}{B(y')} - \frac{1}{p_{x_+}(x)} \int_{x_-}^{x} \frac{dy}{\Psi(y)} \int_{x_-}^{y} \frac{dy' \Psi(y') p_{x_+}(y')}{B(y')} \right] . \tag{3.13}$$

The mean square exit time $\langle T^2 \rangle$ for the particle initially located at x to exit through x_- is

$$\begin{aligned} \langle T^2(x_-, x) \rangle = 4 \ \Big[& \tfrac{1}{p_{x_-}(x)} \textstyle\int_x^{x_+} \frac{dy}{\Psi(y)} \int_{x_-}^{y} \frac{dy' \Psi(y') p_{x_-}(y') T(x_-, y')}{B(y')} - \\ & \textstyle\int_{x_-}^{x_+} \frac{dy}{\Psi(y)} \int_{x_-}^{y} \frac{dy' \Psi(y') p_{x_-}(y') T(x_-, y')}{B(y')} \Big] . \end{aligned} \tag{3.14}$$

Similarly, if the exit is through x_+,

$$\langle T^2(x_+,x)\rangle = 4 \left[\int_{x_-}^{x_+}\frac{dy}{\Psi(y)}\int_{x_-}^{y}\frac{dy'\Psi(y')p_{x_+}(y')T(x_+,y')}{B(y')} - \frac{1}{p_{x_+}(x)}\int_{x_-}^{x}\frac{dy}{\Psi(y)}\int_{x_-}^{y}\frac{dy'\Psi(y')p_{x_+}(y')T(x_+,y')}{B(y')}\right]. \tag{3.15}$$

To calculate the probabilities of exiting through the two end-positions, we need the boundary conditions

$$\begin{aligned} p_{x_-}(x_-) &= p_{x_+}(x_+) = 1 \\ p_{x_-}(x_+) &= p_{x_+}(x_-) = 0 \end{aligned} \tag{3.16}$$

as well as the normalization condition

$$p_{x_-}(x) + p_{x_+}(x) = 1. \tag{3.17}$$

The probability that the particle will exit through $x = x_-$ and $x = x_+$ are given by

$$p_{x_-}(x) = \frac{\int_x^{x_+}\frac{dy}{\Psi(y)}}{\int_{x_-}^{x_+}\frac{dy}{\Psi(y)}} \qquad p_{x_+}(x) = \frac{\int_{x_-}^{x}\frac{dy}{\Psi(y)}}{\int_{x_-}^{x_+}\frac{dy}{\Psi(y)}}. \tag{3.18}$$

During the simulation, we use $x_- = -1$ and $x_+ = 1$ (uniform pore sizes). The scaled drift velocity ($a(x) = A(x)\tau_B/\bar{a}$) is defined as

$$a(x) = \begin{cases} u_- & x \le 0 \\ -u_+ & x \ge 0 \end{cases} \tag{3.19}$$

and the (uniform) scaled diffusion coefficient $b(x) = B(x)/D_c = 2$. Using these reduced units, Eq. 3.18 can be rewritten as

$$p_\pm \equiv p_{\pm 1}(0) = \frac{e^{2u_\mp} - 1}{\frac{u_\mp}{u_\pm}(e^{2u_\pm} - 1) + (e^{2u_\mp} - 1)}. \tag{3.20}$$

The equation for the mean scaled first passage time can be derived using Eqs. 3.11, 3.13, 3.14 and 3.15. For the special case where $x_- = -x_+ = -1$ (uniform pore sizes) and $b(x) = 2$ (uniform diffusion coefficient), the average duration (first moment) of a jump is given by

$$\frac{t_\pm}{\tau_B} = \frac{\langle T(\pm 1,0)\rangle}{\tau_B} = \begin{cases} [2FEGu_\pm^2 + 2u_\pm u_\mp(u_\pm(C(4-C-2D)-1) - FE^2) - \\ u_\mp^2(2E(2F + u_\pm(1+D)))]/[u_\pm^2 u_\mp E(Eu_\pm + Fu_\mp)] \end{cases} \tag{3.21}$$

where we have defined the following parameters to simplify the result:

$$\begin{aligned} C &= e^{u_-} \\ D &= e^{u_\pm} \\ E &= 1 - C \\ F &= 1 - D \\ G &= 1 + C. \end{aligned} \tag{3.22}$$

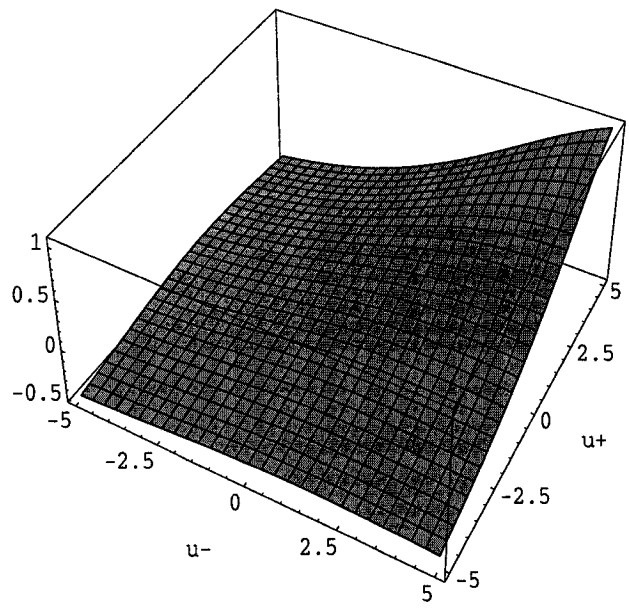

Figure 3.3: A 3-dimensional plot of the logarithm of the first-passage time t_+/τ_B vs. the scale variables $u_\pm$ for the ranges $-5 \leq u_\pm \leq 5$.

Figure 3.3 shows a 3-dimensional representation of t_+/τ_B.

The second moment of the first passage time is given by

$$\frac{t_\pm^2}{\tau_B^2} = \frac{\langle T^2(\pm 1,0)\rangle}{\tau_B^2} = \left\{ \begin{array}{l} [8E^2FGu_\pm^5 + u_\mp(8EFu_\pm^4(2Cu_\pm - FG(C+2))+ \\ u_\mp(8u_\pm^3(-2DE^2FG + u_\pm(1 + D(-3 + C(7 - 2D(1+2C)+ \\ C(11 - 3C))) + C(-3 + C(C+5)) + 2CFGu_\pm))+ \\ u_\mp(4u_\pm^2(2EF(4 - 2CE + D(C(C-4) - 1))+ \\ u_\pm(-2E(D(D-3) - 1 + C(D(10 - 3D - 3C) - 1))+ \\ u_\pm(C(11 + C(C-7)) - 1 + 4CD(D + 3C - 5))))+ \\ u_\mp(8u_\pm(E^2F(5+D) + u_\pm(D(D+6) - 1+ \\ C(6-C) + CD(2D + 6C + CD - 20)+ \\ u_\pm(C(4-C) - 1 + D(C(6 - 2D - 3C) - 3))))+ \\ u_\mp(4E(-4F^2 + u_\pm(2F(1+D)+ \\ u_\pm(1 + D(D+6)))))))))]/[Eu_\pm^4u_\mp^3(Fu_\mp + Eu_\pm)^2] \; . \end{array} \right. \tag{3.23}$$

The variance of the first passage time is simply given by

$$\Delta t^2 = t_\pm^2 - (t_\pm)^2 \; . \tag{3.24}$$

For the case $g = 0$ ($u_\pm = \mp\delta(h_x)$), we recover the equations derived by the biased reptation model (Eqs. 3.1 and 3.4).

3.4 Methodology of the Simulations

We assume that the pores have a uniform size $\bar{a}$, which implies that the tube has a constant length $M\bar{a}$. Since the random fluctuation model cannot be solved exactly when both the external field ϵ and the random interaction energies g_i are present, we will rely on Monte Carlo computer simulations. These simulations are very efficient at the exception of large values of g since one then encounters very large jumping times $t_\pm$ making it difficult to reach a steady-state. Note that the absence of a pre-defined grid or lattice in our simulation means that we do not restrict the chain motion to specific directions.

The chain is first created as a three-dimensional freely-jointed primitive chain where each step has a uniform length $\bar{a}$. Each segment is then associated with an energy g_i ($i = 1...M$) according to Eq. 3.9. We defined $\bar{a} = 1$ for the length scale and $\tau_B(M = 1) = 1$ for the time scale (note that we then have $\tau_B(M) = M \times \tau_B(M = 1) = M$) to simplify the notation. The times, velocities and diffusion coefficients in this chapter are given in unit of $\tau_B(M = 1)$, $\bar{a}/\tau_B(M = 1)$ and $\bar{a}^2/\tau_B(M = 1)$, respectively. The dimensionless electrophoretic mobility μ is then defined as $\mu = V/\epsilon$.

The following procedure is used to simulate a sequence of discrete jumps:

1. First, we calculate the polymer's end-to-end distance, h_x, and the bias parameter $\delta = h_x\epsilon/\bar{a}$.

2. Next, the random energies (noted g_0 and g_{M+1} at this stage) of the two new possible end-segments are generated (following the truncated Gaussian distribution function, Eq. 3.9). The values of $\Delta g_\pm$ are then calculated as $\Delta g_+ = g_{M+1} - g_1$ and $\Delta g_- = g_0 - g_M$. With the bias δ and these values, we calculate the scaled potentials $u_\pm$ using Eq. 3.10.

3. From the values of $u_\pm$, the probability of jumping towards the + end of the tube, p_+, is calculated using Eq. 3.20. We then compare p_+ with a random number between 0 and 1 to choose the curvilinear direction of the next step.

4. Once the direction of the jump is known, we calculate its mean duration t_+ (or t_-) using Eq. 3.21 and its variance Δt_+^2 (or Δt_-^2) using Eq. 3.24, as well as the angular

direction Θ of the new tube section (according to Eq. 3.3). Note that the angles Θ are assumed to be independent of the energies g_i.

5. The chain is then moved in its tube in the selected ($\pm$) curvilinear direction. The current time is increased by $t_+ \pm \Delta t_+$ for a forward jump, or by $t_- \pm \Delta t_-$ for a backward jump (the $\pm$ sign in front of the standard deviation is selected randomly). We finally update the energy vector which keeps the current energy values of the chain's segments as well as the position vector.

This cycle is repeated until the steady-state is reached, which may require millions of iterations for large values of g. The simulation must be long enough for the chain to explore the different values of g_{tot}. Once the steady-state is reached, we can calculate the electrophoretic velocity V and the diffusion coefficient D in the direction of the electric field:

$$V = \lim_{t\to\infty} \frac{d\langle x(t)\rangle}{dt} \tag{3.25}$$

and

$$D = \frac{1}{2}\lim_{t\to\infty}\frac{d}{dt}\left[\langle x^2(t)\rangle - \langle x(t)\rangle^2\right] = \frac{1}{2}\lim_{t\to\infty}\frac{d}{dt}\left\langle (x(t) - \langle x(t)\rangle)^2\right\rangle \tag{3.26}$$

where the $\langle ...\rangle$ averages are over ensembles of identical molecules., i.e., a large number of identical chains are simulated simultaneously. It should be mentioned that the steady-state time t_{ssV} for V is shorter than that (t_{ssD}) for D. The diffusion coefficient in the two transverse directions has not been studied.

3.5 Results

3.5.1 The Zero-Field Case ($\epsilon = 0$): Diffusion Coefficient

Figure 3.4 shows a log-log plot of the relative diffusion coefficient D_g/D_0 as a function of the polymer length M for different values of g. Note that $D_0 = 1/6M(M+1)$ is the diffusion coefficient of a polymer for $\epsilon = 0$ and $g = 0$. As we increase the local interaction energies g, the diffusion coefficient decreases rapidly. This is mainly due to the fact that the polymer tends to stay into areas of low energy for a longer period of time which increases its tube disengagement time. Using Eq. 3.21, we can derive the average first-passage time required

to jump over a distance $\bar{a}$ when $g > 0$ and $\epsilon = 0$,

$$\frac{t_{\pm}(\epsilon \to 0)}{\tau_B} = \left(\frac{-1 + exp(2\Delta g_{\pm}) - 2\Delta g_{\pm}}{2\Delta g_{\pm}^2} \right) . \tag{3.27}$$

It is easy to show that $\langle t_{\pm}/\tau_B \rangle \geq 1.0$ for an unbiased distribution of energy differences $\Delta g_{\pm} > 0$.

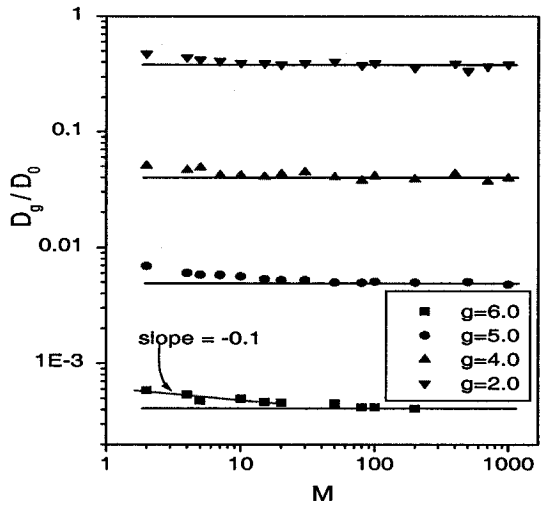

Figure 3.4: A log-log plot of the relative diffusion coefficient $6M(M+1)D_g$ as a function of the molecular size M. Horizontal lines are shown to demonstrate that the scaling $D \sim 1/M(M+1)$ is conserved for long chains.

Further, we notice that the $1/M(M+1)$ scaling law predicted by the standard reptation model is asymptotically conserved for the different values of g used in our simulations, in agreement with Lumpkin's model [122]. Only small deviations are observed for small chains which are due to correlations in the motion of the polymer, that is, consecutive jumps in the same direction are less likely if $g > 0$, thus changing the scaling law for the tube disengagement time to $\tau \sim M^{3+\beta}$, with $\beta > 0$. For larger chains, the standard reptation scaling law $\tau \sim M^3$ is recovered. These results are fundamentally different from those of Zimm and Lumpkin [61] who observed an exponential dependency of the diffusion coefficient $D(M)$ upon the chain length M when g was increased. We believe that the results of ref.

[61] effectively correspond to correlated disorder with a correlation length $\lambda \approx |h_x|$ because of the mathematical method used by these authors. Therefore, the subtle reptation effect of tube memory described earlier is lost if a coarse-graining model is used. In our simulation, the local energies effectively increase the viscosity of the environment and simply reduce the magnitude of the diffusion coefficient.

3.5.2 $\epsilon > 0$: *Electrophoretic Velocity*

Figure 3.5 shows the relative electrophoretic velocities V_g/V_0 vs. the polymer size (M) for energy parameters $g = 1.0$ and 5.0 as well as for different field intensities ϵ. Note that $V_0 = V_{g=0,\epsilon=0}$ is the BRM velocity discussed in Eq. 3.6. We observed that the local interactions reduce the velocities of small chains. In this case, the average disengagement time τ increases due to the formation of regions of low energy. When we increase the local energy parameter g, we increase the depth of those local traps, i.e., we decrease the net electrophoretic velocity. Notice that this effect is more pronounced for low electric fields. For large chains and high electric fields, the relative velocity always reaches unity since the electric forces completely dominate the local energies. In fact, the electrophoretic velocity is driven by the competition between the electric forces acting on the polymer and the local energy interactions (refer to Eq. 3.10). Using simple scaling arguments, we can rewrite Eq. 3.10 assuming that short polymers ($M < 14/\epsilon^2 = M_{min}$) remain in a random-walk statistics ($h_x \sim M^{1/2}$),

$$u_{\pm} \approx 2\epsilon M^{1/2} + \Delta g_{\pm} \tag{3.28}$$

where $\Delta g_{\pm} \sim gM^0$. Consequently, we can approximate the transition size M^* by this condition where both terms are of equal magnitude, that is, $M^* \sim (g/\epsilon)^2$ with the restriction that $M^* < M_{min}$. When $M > M^*$, the random energies become irrelevant compared to the electric forces and the electrophoretic velocities reach "normal" values (the values observed for $g = 0$). When $M < M^*$, the local interaction energies are dominant and the electrophoretic velocities decrease.

Another effect of the local energies on the dynamic of the polymer is the displacement of the minimum velocity (described in Section 3.2) to a size $M_{min}(g) < M_{min}(g = 0)$ (Figure 3.6). More importantly, the minimum is much deeper, which gives rise to very strong "band

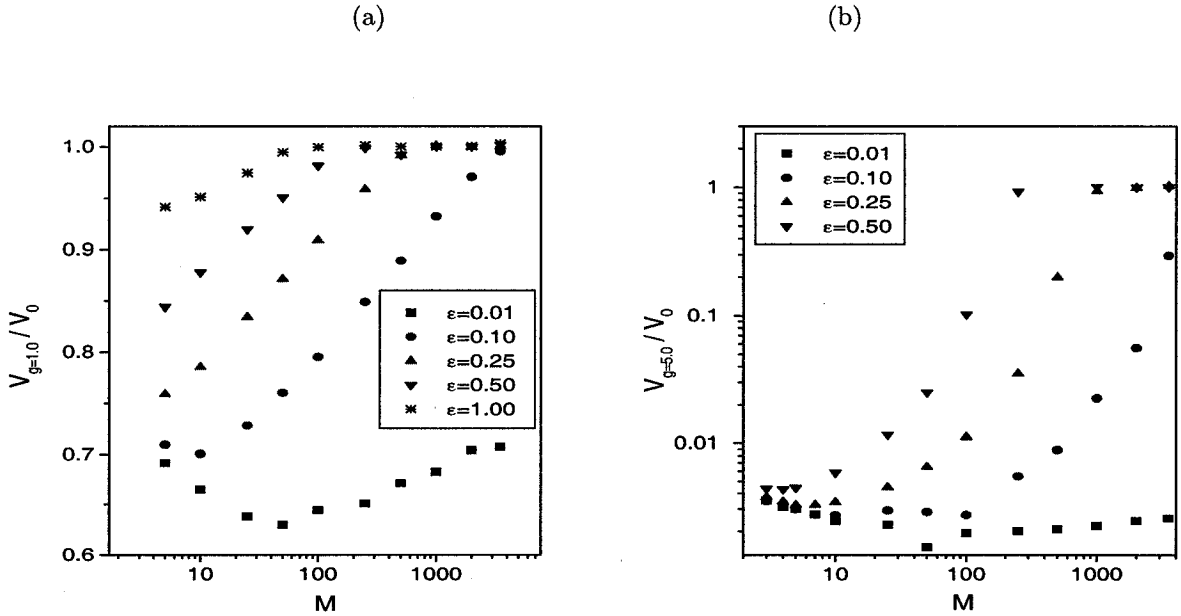

Figure 3.5: A log-log plot of the relative velocity $V_g/V_{g=0}$ vs molecular size M for the (a) $g = 1.0$ and (b) $g = 5.0$ cases. The values of $V_{g=0}$ were calculated as described in ref [113].

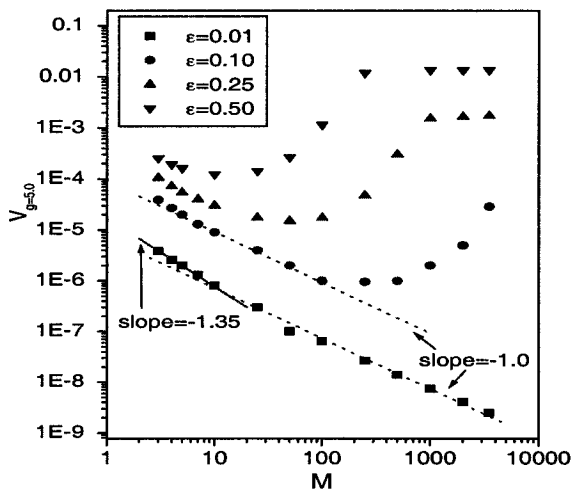

Figure 3.6: A log-log plot of the electrophoretic velocity V vs. molecular size M for the $g = 5.0$ case. The electrophoresis velocity minima predicted by Eq. 3.6 (for the case $g = 0$) are at $M = 1400$, 224 and 56 for the electric field intensities $\epsilon = 0.1$, 0.25 and 0.5, respectively.

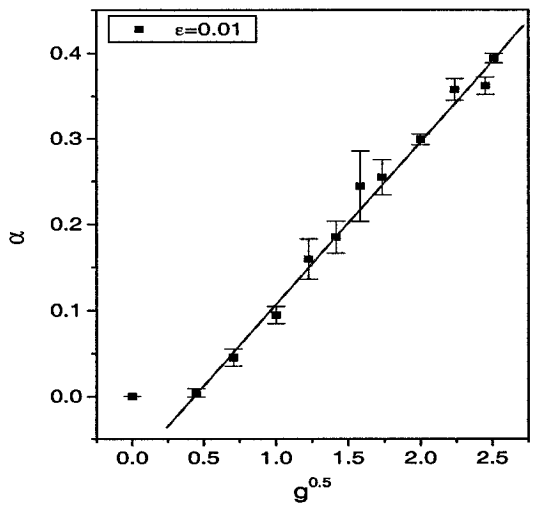

Figure 3.7: Asymptotic value of the effective exponent α vs. the square-root of the energy parameter g.

inversion" where larger chains move faster than smaller ones. This was also obtained by Zimm and Lumpkin [61].

We also find a different effective scaling law $V \sim M^{-(1+\alpha)}$, with $\alpha > 0$, for small chains (see Figure 3.6). Figure 3.7 shows the asymptotic exponent α as a function of $g^{0.5}$ for a low field intensity $\epsilon = 0.01$ where we defined α as

$$\alpha = -\lim_{M \to 1} \left(\frac{\partial log(V)}{\partial log(M)} + 1 \right) \tag{3.29}$$

For low values $g < 0.1$, the local interactions do not affect the electrophoretic velocity and we recover the BRM scaling law $V \sim M^{-1}$. On the other hand, for larger values $g > 0.1$, we find $\alpha \sim g^{0.5}$ with values of α as high as 0.4, i.e., the velocity of small chains follows a scaling relation $V \sim M^{-1.4}$. These results are in agreement with experimental data of Mayer et al. [117] where the electrophoretic velocity was found to decrease as fast as $M^{-1.6}$ for small single-stranded DNA molecules (roughly for $M < 15$) in polyacrylamide gels. Other low field experimental results for single-stranded DNA have reported $V \sim M^{-(1+\alpha)}$, with α increasing linearly with the gel concentration [118]. As we can see on Figure 3.6,

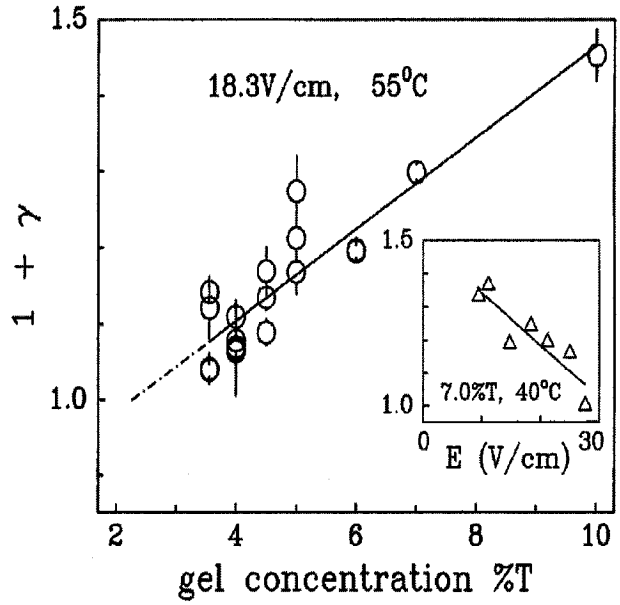

Figure 3.8: Exponent $1+\gamma$ of the mobility scaling of single-stranded DNA ($\mu \sim 1/M^{1+\gamma}$) vs gel concentration for experiments done at 55°C with an electric field $E = 18.3$ V/cm in polyacrylamide gels. The inset shows how the exponent varies with field intensity for a fixed gel concentration. Reproduced from ref. [118].

non-zero values of α can only be observed for low field intensities, also in agreement with experimental data [117, 118] (see Figure 3.8).

Zimm and Lumpkin found important effects for intermediate polymer sizes since their local energies are proportional to $M^{1/2}$ whereas in our local energy model, we only found important effects for small chains since $\Delta g \sim M^0$. Because the electric forces are strictly proportional to $M^{1.0}$ for large values of M (oriented molecules), both models must converge towards the $g = 0$ limit for high field intensities and/or large molecular sizes. We do indeed observe this behaviour for both models.

3.5.3 $\epsilon > 0$: *Diffusion Coefficient*

Figure 3.9 shows a log-log plot of the diffusion coefficient vs. the molecular size M for the $g = 0.1$ and 5.0 cases and for different field intensities ϵ. The relative diffusion coefficient is shown in Figure 3.10 for $g = 5.0$. At low velocities (low field intensities) or for small chains,

the diffusion coefficient is related to the mean rate $1/t_{\pm}$ at which the chain jumps. Since the mean jumping time increases exponentially with g when $\epsilon \to 0$ (refer to Eq. 3.27), the local interactions will tend to decrease the diffusion coefficient. Such an effect is observed in Figure 3.10. Notice that the scaling laws predicted by the BRM are conserved for low field intensities (Figure 3.9).

On the other hand, for high field intensities (high velocities) or long chains, the electric forces dominate over the local energy interactions and the relative diffusion coefficient reaches unity which again leads to very deep minima (Figures 3.9 and 3.10). Surprisingly, in some cases, the ratio D_g/D_0 actually exceeds unity due to the mechanism where deep traps created by the local energies g increase the width $\Delta t_{\pm}$ of the distribution of jumping times. This increased width coupled to shorter mean times $t_{\pm}$ leads to enhanced dispersion of the molecules because we then have $D \sim \Delta t_{\pm}^2/t_{\pm}^3$ [123]. In the high field limit, many chains will migrate together at a high velocity ($t_{\pm} \ll 1$) and some of them will get trapped in a local (low-energy) environment with $t \approx t_{\pm} + \Delta t_{\pm}$. The trapped chains will lag behind the others by a distance $\Delta x \sim v\Delta t_{\pm}$ giving a diffusion coefficient $D \sim \Delta x^2/t_{\pm} \sim \Delta t_{\pm}^2/t_{\pm}^3$. Therefore, the atypically deep local traps play a large role, and the diffusion coefficient becomes proportional to the ratio $\Delta t_{\pm}^2/t_{\pm}^3$.

Using the Nernst-Einstein relation (which is expected to be valid only in the equilibrium limit, i.e., $M > M_d \equiv 1.68\epsilon^{-2/3}$), we can relate the electrophoretic velocity to the diffusion coefficient to obtain the following relationship:

$$D_g(M,\epsilon) = \frac{1}{2\epsilon(M+1)} \times V_g(M,\epsilon). \tag{3.30}$$

Figure 3.11 shows a logarithmic plot of the "Nernst-Einstein ratio" $(D_g/V_g)2\epsilon(M+1)$ vs. molecular size M. When $g = 0$, the ratio is equal to unity for small molecular sizes, indicating that the Nernst-Einstein relation is indeed valid in this limit. However, when $g > 0$, the ratio is always larger than unity. This is consistent with the fact that far from equilibrium, D is more affected than V.

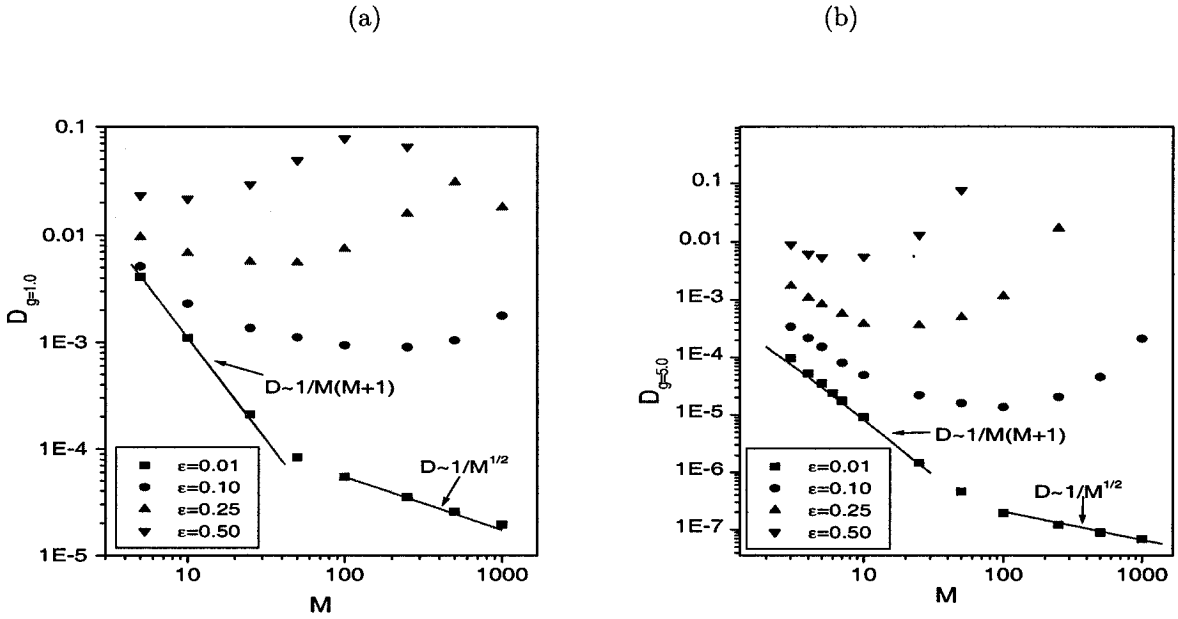

Figure 3.9: A log-log plot of the diffusion coefficient vs. molecular size M for the (a) $g = 1.0$ and (b) $g = 5.0$ cases. Lines showing the scaling laws $1/M(M+1)$ and $M^{-1/2}$ are provided for comparison.

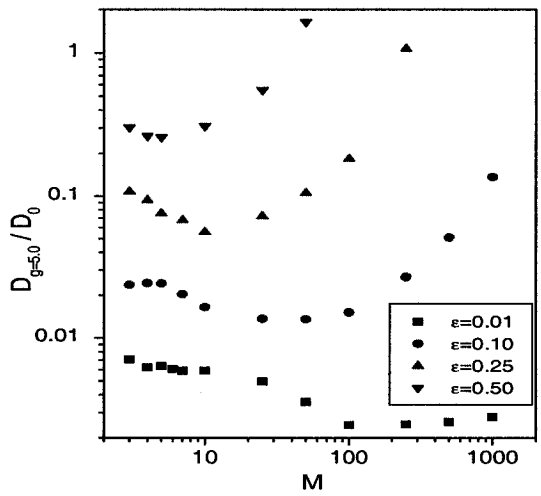

Figure 3.10: A log-log plot of the relative diffusion coefficient $D_{g=5.0}/D_{g=0}$ vs. molecular size M. The values of $D_{g=0}$ were calculated as described in ref [113].

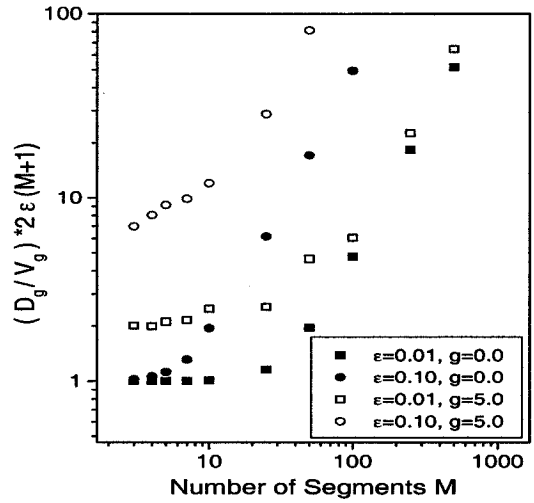

Figure 3.11: A log-log plot of the "Nernst-Einstein ratio" $(D_g/V_g) \times 2\epsilon(M+1)$ vs. molecular size M for various cases.

3.6 Discussion

In this chapter, we presented a generic mathematical model for the diffusion of polymers and polyelectrolytes in irregular matrices. The equations that characterized the discrete random jumps made out by the polymer in its reptation tube when an external field and/or local interaction energies are present have been derived using the theory of stochastic processes. Since each random jump is carried over a distance $\bar{a}$, our model takes into account subtle memory effects that are due to the reptation dynamics in the presence of local interactions. This is much different from the model proposed by Zimm and Lumpkin [61] where the chain hops over length scales comparable to the chain's end-to-end distance h_x. Not surprisingly, ZL's results show that even weak local interactions g can have dramatic effects on both the diffusion coefficient and the electrophoretic velocity. We believe that the coarse-graining step effectively led to a system with a correlation length $\lambda \approx h_x$. On the other hand, our model keeps a strict correlation length $\lambda \approx \bar{a}$.

In the absence of a field, our results predict a small increase of the molecular-size

dependence of the diffusion coefficient. This comes from the fact that the local energies lead to correlated jumps of the chain in its tube (consecutive jumps in the same direction become less probable), thus changing the scaling law for the tube disengagement time to $\tau \sim M/D \sim M^{3+\beta}$, with $\beta > 0$. This subtle effect of tube memory is lost if a coarse-graining procedure is used. We also note that this effect is found only for small molecular sizes, and that the standard scaling law $D \sim M^{-2}$ is recovered very naturally for large sizes M. Our model thus predicts that deviations from the standard reptation model are expected only for small molecules.

In the presence of an electric field, the situation can become quite complicated. For low fields and low molecular sizes, we simply get $V \sim 1/M^{1+\alpha}$ with $\alpha > 0$, in qualitative agreement with the experimental results of Mayer et al. [117] and of Rousseau et al. [118]. For high fields, both the diffusion coefficient and the electrophoretic velocity converge towards their $g = 0$ values since the electric forces dominate over the effect of the local energies. The intermediate case is complicated and leads to very large mobility inversions, as found by ZL, and increased diffusion. Such effects have yet to be reported experimentally.

In conclusion, we have presented a set of generalized stochastic equations to study the reptation of polymer chains in the presence of local interaction energies. The examples studied in this chapter provide interesting results that agree with recent electrophoresis experimental data. The next logical step is to study the diffusion of polymer chains in quenched matrices where the random energies g are correlated over distances $\lambda > \bar{a}$. For short chains such that $R_g < \lambda$, we expect the molecules to get trapped in local, low-energy volumes of size λ^3. For larger chains such that $R_g \gg \lambda$, however, the chain is expected to effectively reptate in a "rough" tube. This could be a realistic model to study the effect of gel concentration inhomogeneities on polymer diffusion. In the presence of an electric field, further effects are expected when the electric forces orient short polymers and make them move quickly between low-energy areas. This is the subject of the next chapter.

Chapter 4 Reptation Dynamics in a Random Energy Landscape with Long-Range Correlations: Quenched Model

4.1 Introduction

Real porous media, of course, are neither totally uncorrelated nor annealed. Gels, for instance, may be heterogeneous over length scales λ that greatly exceed their mean pore size $\bar{a}$, and these heterogeneities are expected to be quenched. Stellwagen [50], for example, reported the apparent presence of very large domains ($\lambda \gg \bar{a}$) in agarose gels, and such domains may actually play a role in the separation of large DNA molecules by pulsed-field gel electrophoresis if $R_g \simeq \lambda$.

In this chapter, we use a modified reptation model based on the algorithm described in Chapter 3 to study the reptation dynamics of a polymer chain in a gel with quenched and correlated energy landscapes, first in the absence and then in the presence of an external driving force (e.g., an electric field in the case of gel electrophoresis). The gel is essentially made of cubic cells of volume λ^3, with $\lambda \geq \bar{a}$, and we associate a random energy g_i to each cell. A smoothness parameter β is also introduced to control the width of the energy interface between uncorrelated cells so that we can study both smooth and sharp energy landscapes. As we shall see, the correlation length 2λ (which was equal to the mean pore size $\bar{a}$ in our previous Chapter) plays a major role in determining the static and dynamic properties of a reptating chain, especially when the chain's unperturbed radius of gyration R_g is comparable to λ. The competition between the reptation motion and the localization of the chain in the low-energy regions of the gel lead to new diffusion regimes.

4.2 The Biased Reptation Model with Excluded Volume Interactions

The equations for the diffusion coefficient and the electrophoretic velocity given in Chapter 3 were derived for an ideal chain without excluded volume. When excluded volume is taken into account, these equations vary slightly, as we will see in this section. In the absence of an electric field and local interactions, a real chain may be represented by a self-avoiding walk instead of a simple random walk for the case of an ideal chain. Using this model, the mean square end-to-end distance scales like $\langle h_x^2 \rangle \sim M^{6/5}\bar{a}^2$. Therefore, the uncertainty (variance) about the position of the center-of-mass when the entire tube is renewed is given by [124]

$$\langle \Delta x^2 \rangle = \langle h_x^2 \rangle - \langle h_x \rangle^2 \sim M^{6/5}\bar{a}^2 \tag{4.1}$$

where $\langle h_x \rangle = 0$ since $\epsilon = 0$.

The average electrophoretic velocity can be written as,

$$V(M,\epsilon) = \frac{\langle \Delta x \rangle}{\tau} \tag{4.2}$$

where the mean tube renewal time τ is defined as the ratio of the tube length $L_p \sim M$ divided by the chain longitudinal velocity V_ℓ. Since the mean distance travelled by the chain in the direction of the electric field during a jump is simply $(p_+(h_x) - p_-(h_x))\bar{a}$, where $p_\pm(h_x)$ is the probability for the polymer to jump towards the $\pm$ end of the tube (see Eq. 3.1), the longitudinal velocity is simply given by

$$V_\ell(M,\epsilon) = \frac{(p_+(h_x) - p_-(h_x))\bar{a}}{\tau_\pm(h_x)} = \frac{\delta\bar{a}}{\tau_B} \sim \frac{\epsilon h_x}{\tau_B} \sim M^{-2/5}\epsilon \tag{4.3}$$

where $\tau_\pm(h_x)$ is the mean time required to jump over a distance $\bar{a}$ (see Eq. 3.4). This gives $\tau \sim M^{7/5}/\epsilon$. Therefore, the average electrophoretic velocity can be rewritten as

$$V(M,\epsilon) = \frac{\langle \Delta x \rangle}{\tau} \sim \frac{M^{3/5}}{M^{7/5}\epsilon^{-1}} \sim M^{-4/5}\epsilon. \tag{4.4}$$

The electrophoretic velocity given by Eq. 4.4 is valid until the polymer becomes elongated, i.e., $Ma\langle cos\theta \rangle < \langle |h_x| \rangle$ where we used $\langle |h_x| \rangle^2 \sim M^{6/5}\bar{a}^2$ [124].

Within the limit of low field intensities, the mean tube renewal time is driven by thermal motion and is given by the zero-field limit $\tau(M, \epsilon \to 0) = M^2\tau_B \sim M^3$. In this case, the diffusion coefficient is therefore given by

$$D(M,\epsilon) \cong \frac{\langle \Delta x^2 \rangle}{2\tau} \sim M^{-9/5}\epsilon^0 \ . \tag{4.5}$$

When the total electric force QE is large enough, the motion inside the tube becomes biased and the tube renewal process is accelerated; this leads to a longitudinal velocity (i.e., along the tube axis) given by Eq. 4.3. The polymer length at which the longitudinal velocity takes over the thermal motion can be derived from the inequality $\tau(M, \epsilon \to 0) > \tau(M, \epsilon)$. We then get $M > \epsilon^{-5/8} \equiv M_d$. This lead to a diffusion coefficient

$$D(M, \epsilon) \cong \frac{\langle \Delta x^2 \rangle}{2\tau} \sim M^{-1/5} \epsilon \, . \tag{4.6}$$

4.3 The Random Fluctuation Model: a Quenched Matrix

As we have seen in Chapter 3, the motion of a polymer inside a gel is described by the Rouse or the reptation model depending on its radius of gyration (R_g) and the average pore size ($\bar{a}$). In this Chapter, we consider only the case where the radius of gyration is much larger than the typical pore size of the gel such that the reptation regime applies.

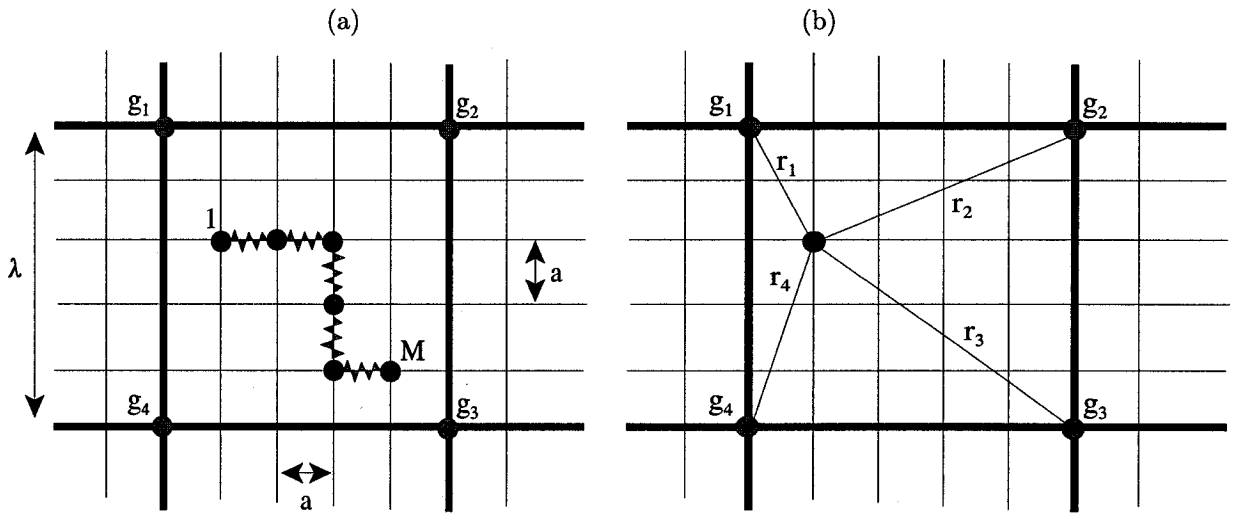

Figure 4.1: A two dimensional representation of the simulation matrix for $\lambda = 5\bar{a}$ where each vertex represents the center of a pore. (a) shows the position of a polymer of length $M = 5$ segments (or $M + 1$ monomers); (b) shows the distance from the first bead of the polymer with respect to the four corners of a cell. Note that the energy is given to the polymer's monomers (vertex) instead of its segments.

In the standard reptation theory, each pore of the gel is assumed to be energetically equivalent, that is, the probability to jump from either end of the tube is equal (1/2). This

assumption is probably not valid for various reasons. If the polymer encounters a narrow or curved space, either it must bend itself to continue or the gel must deform, or both. Each of these cases requires energy and can lead to local energetic effects.

To model the motion of polymers in a quenched energy landscape system, we use a modified reptation theory with local free energies. The gel matrix is defined by two characteristic lengths, the mean pore size $\bar{a}$ and the energy correlation length $2\lambda \geq \bar{a}$ (Figure 4.1 (a)). We also associate a pre-defined energy to each pore. This is achieved by defining an energy function (a random function with a correlation length 2λ) which depends only on the coordinates of the pores.

The gel matrix is divided into cubic cells that contains $(\lambda/\bar{a})^3$ pores for a three dimensional system. Each of the eight corners of a cell is given a random energy g_i, in units of k_BT (Figure 4.1), based on its coordinates. The distribution function $w(g_i)$ is a Gaussian with a mean value of 0 and a standard deviation g (refer to Eq. 3.9). In practice, we cut the Gaussian beyond $2g$ in order to avoid exceedingly large trapping times. We use the coordinates of the corner of a cell to generate a unique random number which is then used to calculate the corner energy g_i following the distribution $w(g_i)$:

1. We first generate three random integers based on the coordinates (x,y,z):

   - random seed ♯ 1 = (X * 151 + 1013904223) * 1664525 + 1013904223
   - random seed ♯ 2 = (Y * 417 + 1013904223) * 1664525 + 1013904223
   - random seed ♯ 3 = (Z * 720 + 1013904223) * 1664525 + 1013904223

   Note that the integers 151, 417 and 720 could be changed to obtain different realizations of the energy landscapes.

2. Using these numbers, we generate three random numbers between -1 and 1:

   - random number ♯ 1 = random seed ♯ 1 * 4.656612875245797d-10
   - random number ♯ 2 = random seed ♯ 2 * 4.656612875245797d-10
   - random number ♯ 3 = random seed ♯ 3 * 4.656612875245797d-10

3. We then combine these three random numbers to generate a unique number which is converted into an integer:

- random integer = (ran1+ran2+ran3)*4357938274.

4. This integer is then used within a random gaussian number generator to obtain the value of g_i. Therefore, a given set of coordinates (x,y,z) will always give us the same pseudo-random energy g_i.

To compute the energy of a pore inside such a cubic cell, we first evaluate the energy value of each of the eight corners of the specific cell (as detailed previously) and then interpolate the energy of the pore g_{pore} using the following relationship:

$$g_{pore} = \frac{\sum_{i=1}^{8} g_i r_i^{-\beta} \prod_{\alpha=1}^{3}(\lambda - \Delta r_{i\alpha})}{\sum_{i=1}^{8} r_i^{-\beta} \prod_{\alpha=1}^{3}(\lambda - \Delta r_{i\alpha})} \tag{4.7}$$

where $\Delta r_{i\alpha}$ is the absolute distance between the pore and cell corner i in the direction given by the index α ($j = x, y, z$), $r_i = \sqrt{\sum_\alpha \Delta r_{i\alpha}^2}$ is the net distance between the pore and a corner, and β is a parameter (exponent) that controls the smoothness of the energy landscape. Such a function puts more weight on the cell corner that is the closest to the pore that we want to evaluate. Using Eq. 4.7, $\beta = 2$ and $\lambda = 5$, the energy value of monomer ♯1 in the two-dimensional example shown in Figures 4.1 (a) and (b) is given by

$$\begin{aligned} g_{pore} &= \frac{g_1(\frac{4\times3}{1+4}) + g_2(\frac{1\times3}{16+4}) + g_3(\frac{1\times2}{16+9}) + g_4(\frac{4\times2}{1+9})}{(\frac{4\times3}{1+4}) + (\frac{1\times3}{16+4}) + (\frac{1\times2}{16+9}) + (\frac{4\times2}{1+9})} \\ &= \frac{240g_1 + 15g_2 + 8g_3 + 80g_4}{343} \ . \end{aligned} \tag{4.8}$$

If we have the following g_i values for the four corners of the cell: $g_1 = +0.5$, $g_2 = -2.0$, $g_3 = -1.0$ and $g_4 = -0.5$, then the energy of the first monomer will simply be $g_{pore} \approx +0.122$. Figures 4.2 and 4.3 illustrate typical one and two dimensional potential energy landscapes. Figure 4.2 shows the effect of the parameter β on the energy landscape (top Figure is with $\beta = 2$, bottom Figure is with $\beta = 4$). The larger the β parameter, the more abrupt (rough) is the landscape. We used a value of $\beta = 2$ for the simulations discussed in this Chapter.

As described in the previous Chapter, the displacement of the chain inside the tube can be represented by the diffusion of a particle between two absorbing walls. When the particle is absorbed by the + (or −) "wall", the polymer moves toward the + (−) end of its tube (Figure 3.1). The effect of the electric field on the displacement of the particle is represented by the longitudinal drift velocity V_c. The drift velocity V_c can be obtained from

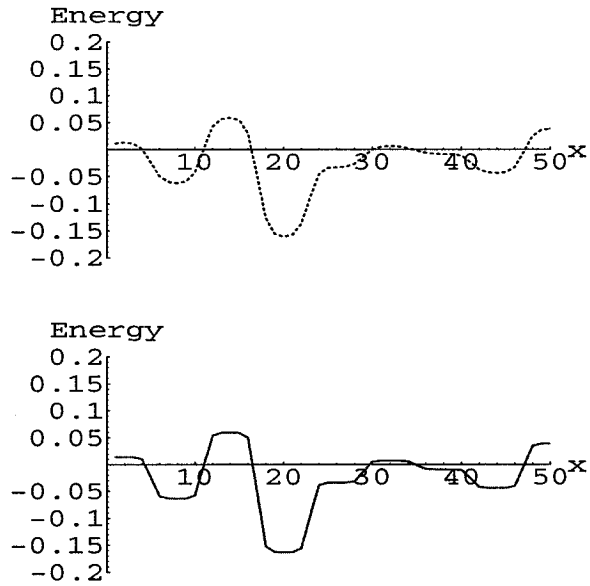

Figure 4.2: A one dimensional representation of the energy landscapes for $g = 0.5, \lambda = 6$ and $\beta = 2$ (top) and $\beta = 4$ (bottom).

a potential function U as $V_c = -\nabla U/\xi$, where $\xi \sim M$ is the curvilinear friction coefficient of the polymer. We can write this equation in terms of scaled variables such that $v_c = -\nabla u$ (with $v_c = V_c \tau_B/\bar{a}$ and $u = U/k_B T$).

For a constant and uniform electric field, the effect of the local energies g_i is a random perturbation of the local (wall) potentials $u_\pm$ (Figure 3.2). The new values of $u_\pm$ are simply the sum of the two terms: the electric potential ($\mp\delta$ defined by Eq 3.2) and a random energy term (Eq. 3.10).

In the annealed system described in the previous Chapter, the energy values of the two new possible tube segments were simply given by two random numbers g_i, following Eq. 3.9. In the quenched system, the two new possible effective energy values used for the calculation of $\Delta g_\pm$ are actually the average energies of the five possible directions (for our three dimensional system) that the end polymer segment can choose after the direction ($\pm$) of the move is chosen. In other words, we first decide through which end ($\pm$) the polymer will move; this is followed by the selection of the new segment orientation. We used the

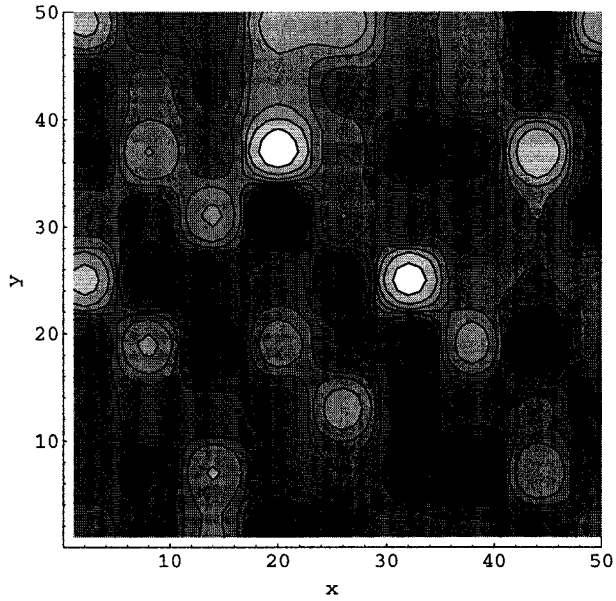

Figure 4.3: A two dimensional contour plot of an energy landscape characterized by the parameters $g = 0.5, \lambda = 6$ and $\beta = 2$. High energy values are found in the dark regions whereas white regions represent low energies (wells).

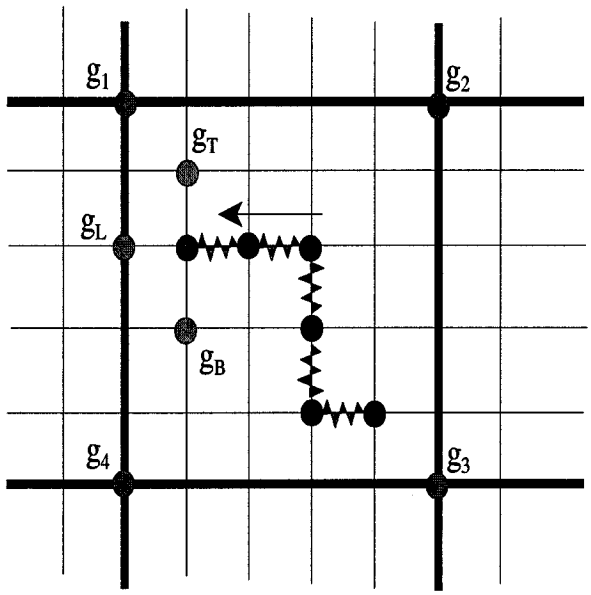

Figure 4.4: A two dimensional representation of the jumping process

following equation to calculate the mean energies $g_{\pm wall}$ for the end jumps:

$$g_{\pm wall} = \frac{\sum_{pore=1}^{5} g_{pore} e^{-g_{pore}}}{\sum_{pore=1}^{5} e^{-g_{pore}}} . \tag{4.9}$$

The above equation uses a Boltzmann exponential to provide more weight to negative values of the pore energies. For instance, in Figure 4.4, the average energy value g_{wall} of the new tube segment (direction of the first monomer) is simply $g_{wall} \approx +0.0153$ given that $g_T \approx +0.439$, $g_L \approx +0.271$ and $g_B \approx -0.324$. An alternative to Eq. 4.9 is to first choose a specific orientation among g_T, g_L and g_B for the new tube segments, calculate their energy values, then calculate $\Delta g_{\pm}$ and finally choose the direction ($\pm$) of the jump. Our approach attempts to take into account the fast fluctuations of the chain end's positions and local chain orientation described by the biased reptation with fluctuations model [115, 125, 126].

The mean first-passage time and the probability that the particle (chain) will first reach a given wall (end of the tube) can be derived using stochastic methods (more precisely, the Fokker-Planck equation). The mean exit time $\langle T \rangle$ is given by Eqs. 3.11 and 3.13 respectively while its mean square exit time $\langle T^2 \rangle$ is given by Eqs. 3.14 and 3.15. The probability of jumping towards the $\pm$ wall is given by Eq. 3.18. Finally the probability that the new tube segment occupies one of the five possible orientation (pores) is given by

$$p_k = \frac{e^{-g_k + \gamma(\epsilon)}}{\sum_{pore=1}^{5} e^{-g_{pore} + \gamma(\epsilon)}} \tag{4.10}$$

where k is the pore index (with $\sum_{k=1}^{5} p_k = 1$) and $\gamma(\epsilon) = \epsilon$ for the orientation along the field, -ϵ for the orientation opposite to the field and 0 for the other orientations. If the pore is already occupied with a segment of the polymer, the move is rejected and the current time is increased.

4.4 Methodology of the Simulation

Since the polymer is assumed to take a random conformation when loaded into the gel during real diffusion or gel electrophoresis experiments, the polymer is first created as a three-dimensional idealized freely-jointed self-avoiding random walk primitive chain where each step has a uniform length $\bar{a}$. In our simulation program and for the rest of this Chapter, we use $\bar{a} = 1$ and $\tau_B(M = 1) = 1$ for the length and time scales (note that we then have

$\tau_B(M) = M \times \tau_B(M=1) = M$). An important aspect of this computer simulation is the presence of a pre-defined grid or lattice which limits the chain motion to specific directions. Once the chain is created, with each segment energy selected according to Eq. 4.7, the following procedure is used to simulate the sequence of discrete jumps:

1. First, we calculate the polymer's end-to-end distance, h_x, and the bias parameter $\delta = h_x\epsilon/\bar{a}$.

2. Next, the average (or effective) random energies (noted $g_{\pm wall}$ at this stage) of the two possible new tube sections are generated (following Eq. 4.9). Following this, the values of $\Delta g_\pm$ are calculated as $\Delta g_+ = g_{+wall} - g_1$ and $\Delta g_- = g_{-wall} - g_M$ since during a + (-) jump the $i = 1$ ($i = M$) tube segment will be lost while the $i = M+1$ ($i = 0$) segment will be created. With δ and these values, we calculate the scaled potentials $u_\pm$ using Eq. 3.10.

3. From the values of $u_\pm$, the probability of jumping towards the + end of the tube, p_+, is calculated using Eq. 3.18. We then compare p_+ with a random number between 0 and 1 to choose the curvilinear direction (+ or - end) of the next step.

4. We calculate the probabilities of the five possible orientations of the new tube segment using Eq. 4.10. The direction of the segment is then chosen by comparing these probabilities with a random number between 0 and 1.

5. Once the direction and orientation are known, we calculate the mean duration t_+ (or t_-), Eq. 3.21, and the variance Δt_+^2 (or Δt_-^2), Eq. 3.24, of the jumping process.

6. The chain is then moved in its tube in the selected ($\pm$) curvilinear direction, unless the new site is already occupied. The current time is increased by $t_+ \pm \Delta t_+$ for a forward jump, or by $t_- \pm \Delta t_-$ for a backward jump (the $\pm$ sign in front of the standard deviation is selected randomly). We finally update the energy vector as well as the position vector.

This cycle is repeated until the steady-state is reached, i.e., the simulation must be long enough for the chain to explore the spatial distribution of energies. The duration of this transient period depends strongly on the local interaction energy parameter g. We

then calculate the electrophoretic velocity V and/or the diffusion coefficient D (in the field direction) of the polymer using Eqs. 3.25 and 3.26. The diffusion coefficient in the two transverse directions has not been studied. It should be mentioned that the steady-state time t_{ssV} for V is shorter than that (t_{ssD}) for D. The times, velocities and diffusion coefficients are given in unit of $\tau_B(M=1)$, $\bar{a}/\tau_B(M=1)$ and $\bar{a}^2/\tau_B(M=1)$, respectively.

The radius of gyration R_g^2 is also evaluated during the simulation using the following definition:

$$\langle R_g^2(M)\rangle = \frac{1}{M+1}\left\langle \sum_{i=1}^{M+1} (\mathbf{r}_i - \mathbf{r}_{cm})^2 \right\rangle \tag{4.11}$$

where $\mathbf{r}_i$ is the (x,y,z) coordinate of monomer i and $\mathbf{r}_{cm} = \frac{1}{M+1}\sum_i \mathbf{r}_i$ is the position of the center of mass of the polymer.

4.5 Results

4.5.1 *Testing the Algorithm ($\epsilon = 0$ and $g = 0$)*

The simulation was first tested against known reptation results ($g = 0$). Figure 4.5 (a) shows the mean square radius of gyration, R_0^2, versus the length of the polymer M. As anticipated, the self-avoiding walk power law $R_g^2 \sim M^{1.2}$ was obtained (we thus find the proper three-dimensional Flory exponent $\nu = 3/5$). Similarly, the diffusion coefficient D_0 as a function of M is plotted in Figure 4.5 (b). On a logarithmic plot, it is easy to see that $D_0 \sim M^{-9/5}$ as predicted. The agreement between the simulation results (points) and the "exact" analytical prediction of the theory tells us that the method works correctly for the $g = 0$ and $\epsilon = 0$ limit.

4.5.2 *The Zero-Field Case ($\epsilon = 0$) with Local Interactions ($g > 0$)*

We now investigate the effect of the local interaction energies g on the reptation dynamics of polymers in the zero-field case ($\epsilon = 0$). The simulations are performed using the smoothness parameter $\beta = 2.0$. Figure 4.6 shows the relative mean square radius of gyration R_g^2/R_0^2 as a function of the polymer length $2 < M < 1000$ for different values of g (0.050, 0.075 and 0.100) and λ (1.0, 3.0 and 6.0).

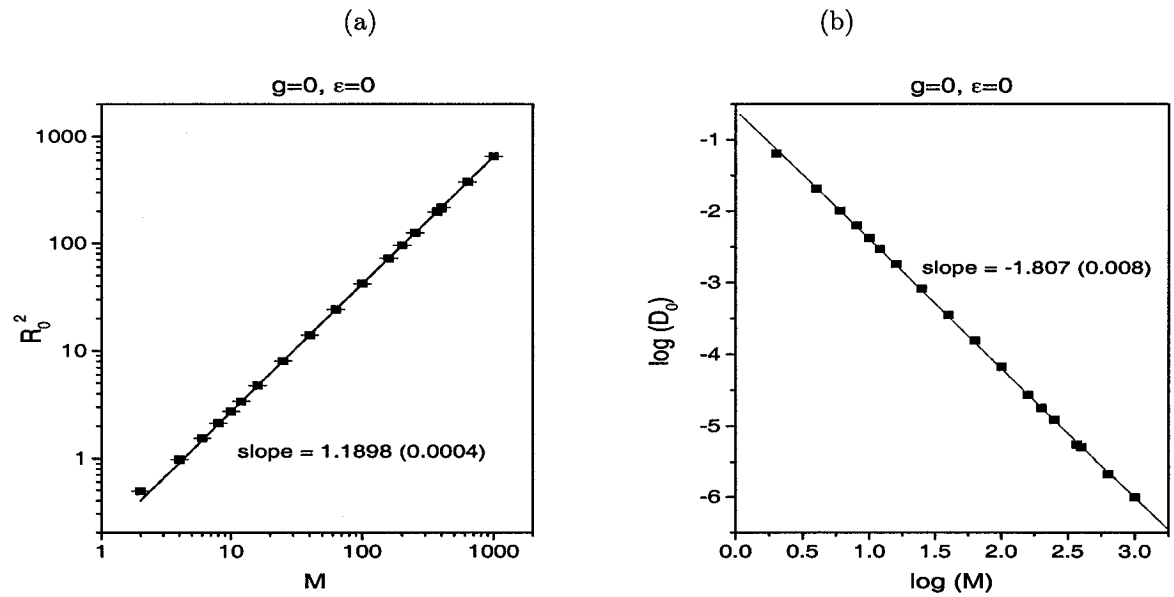

Figure 4.5: (a) Log-log plot of the mean square radius of gyration R_0^2 vs. the length of the polymer M; (b) Log-log plot of the diffusion coefficient D_0 vs. M. For both cases, we obtain the expected scaling laws.

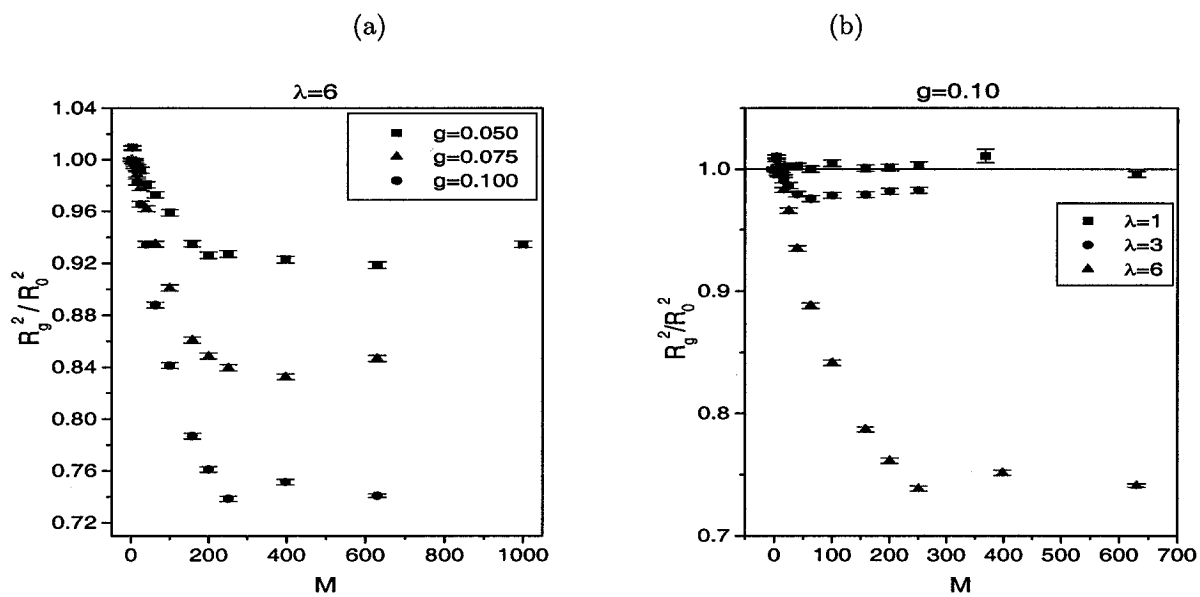

Figure 4.6: Mean square radius of gyration ${R_g}^2$ vs. the length M of the polymer for (a) different values of g, and (b) different values of λ.

We have seen that when the local interaction energies are present ($g > 0$), the simulation matrix is composed of regions of high and low energies (see Figure 4.3). When the polymer encounters regions of low energy, it tends to collapse into one or more of such regions (Figure 4.7) to lower its total energy, therefore reducing its radius of gyration (Figure 4.6). The size of these regions is defined by the parameter λ whereas their depth (energy value) is characterized by g. For larger values of the local energy parameter g, we increase the depth of these local traps (low energy regions) and, consequently, we increase the collapsing effect of the polymer and the time required by the polymer to exit the trap. For small polymers, the effect is negligible since they can easily (i.e., rapidly) escape. When increasing λ, we increase the width (size) of the local traps allowing larger chains to fit into them. This leads to a smaller radius of gyration for larger chains as shown in Figure 4.6 (b). For both cases (large g and λ values), the relative radius of gyration reaches a plateau for large polymers. In this regime, the polymer finds itself occupying many regions of low energies as show in Figure 4.7. The maximum number of monomers M_r that can fit into any region is $\sim \lambda^3$. Therefore, the plateau should begin around $M = (\lambda/\bar{a})^3$. In our simulation, this gives $M_r = 27$ and 216 for $\lambda = 3$ and 6 respectively. Figure 4.8 shows the radius of gyration divided by $M^{6/5}$ (the scaling law for R_0^2) as a function of M. Also shown in this Figure is the plateau (horizontal line) and M_r. We see that our results for the beginning of plateaus are in agreement with our prediction. Note that we do not have data points for sizes larger than $M = 1000$ since the steady-state could not be reached (in spite of extensive simulation times).

Figure 4.9 is a log-log plot of the relative diffusion coefficient D_g/D_0 vs. the length M of the polymer for different values of g and λ. In the absence of an electric field, the diffusion coefficient is simply given by $D \sim R_g^2/\tau$. Since the relative radius of gyration R_g^2/R_0^2 decreases only by less than 30% (see Figure 4.6), the decrease in the diffusion coefficient found in Figure 4.9 is mainly due to an increase in τ. We have seen that the collapsing of the polymer is stronger for larger chains, larger values of g and larger values of λ. In this case, the polymer finds itself trapped in regions of the matrix where the local energies are low and where the escape times are large. Since the escape time depends on the length of the polymer (as long as $R_g < \lambda$), small chains will exit much faster than larger ones. Therefore, the diffusion coefficient of small chains should remain unchanged as observed in

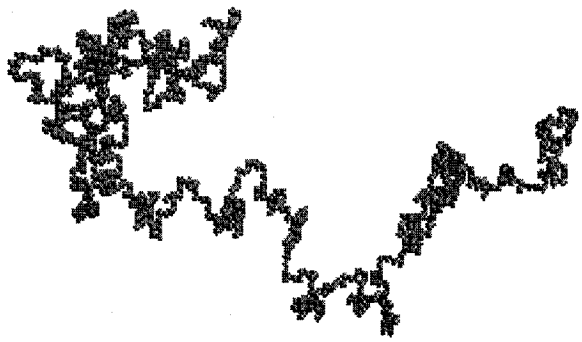

Figure 4.7: Polymer of length $M = 1000$ moving inside the simulation matrix for $\lambda = 6$ and $g = 0.1$. Notice the aggregation of monomers along the chain.

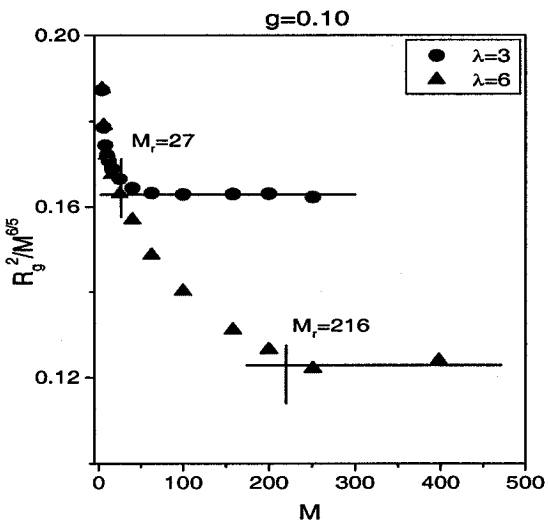

Figure 4.8: Scaled mean square radius of gyration $R_g^2/M^{6/5}$ vs. M for $\lambda = 3$ and 6. We also show the predicted plateaus.

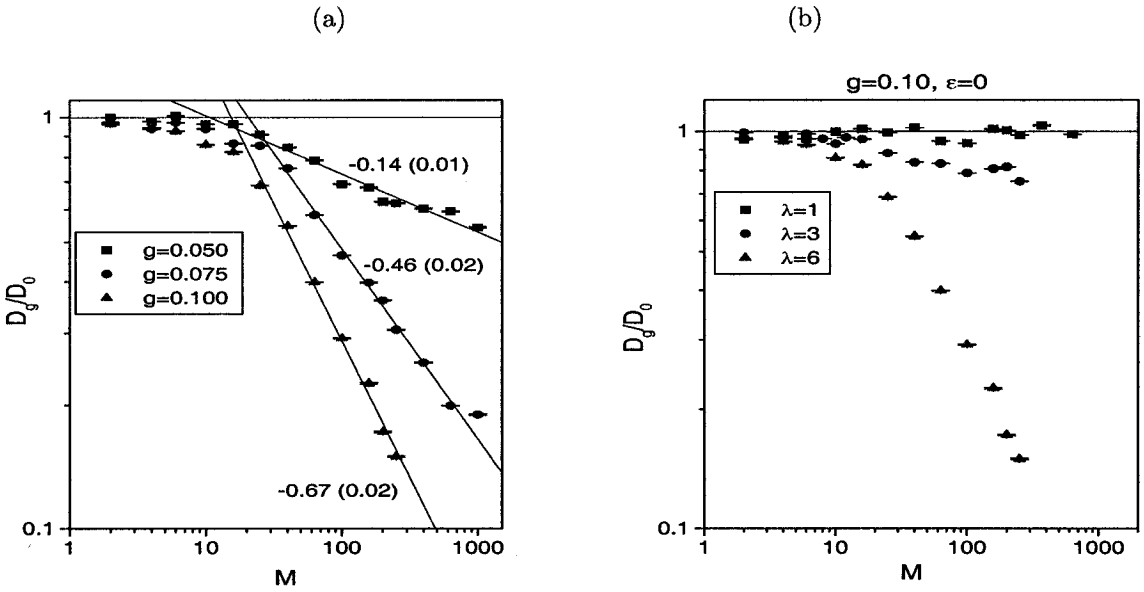

Figure 4.9: Relative diffusion coefficient vs. the length M of the polymer for (a) different values of g and (b) different values of λ.

Figure 4.9. For larger polymers, however, the diffusion coefficient decreases at a much faster rate than predicted by the reptation model. In our simulations, we find $D_g \sim 1/M^{1.8+\alpha}$ with $\alpha = 0.14 \pm 0.01$ for $g = 0.05$, $\alpha = 0.46 \pm 0.02$ for $g = 0.075$ and $\alpha = 0.67 \pm 0.02$ for $g = 0.1$, in qualitative agreement with experimental results of Rotstein and Lodge [107]. These authors found that the diffusion coefficient of linear polystyrenes in poly(vinyl methyl ether) gels decreases as fast as $D \sim 1/M^{-2.8}$ depending on the concentration of the gel. Our simulation results are very different from those obtained for the annealed matrix studied in Chapter 3 where the D_0 scaling law was maintained but the relative diffusion coefficient decreased below unity for all chain lengths.

Another interesting parameter to study is the total energy E of a polymer chain in the gel. Figure 4.10 shows the total energy distribution of a polymer of size $M = 251$ for $g = 0.075$ and $\lambda = 6$ (this is a situation where trapping is very strong; see Figure 4.6). This is well described by a Gaussian with a mean value of -12.4 and a standard deviation of 3.44. We found that the mean value $\langle E \rangle$ and the standard deviation ΔE both increase linearly with g on a log-log plot (Figure 4.11), consistent with the scaling laws $\langle E \rangle \sim g^2$

and $\Delta E \sim g^1$.

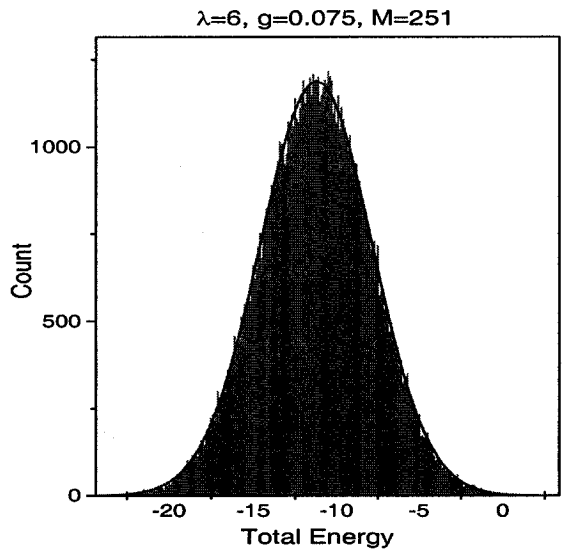

Figure 4.10: Total energy distribution function for a polymer of size $M = 251$ with $g = 0.075$ and $\lambda = 6$. The solid line represents a Gaussian fit with a mean $\langle E \rangle = -12.4$ and a standard deviation $\Delta E = 3.44$.

Therefore, we should obtain a universal curve when plotting -$\langle E \rangle / g^2$ vs. M for different values of g (Figure 4.12). In fact, we observe that $\langle E \rangle \sim M^{0.991 \pm 0.002}$ for all values of M when $\lambda = 1$, that is, $\langle E \rangle \sim M^1 g^2$. We also notice two different regimes when $\lambda > 1$. Below a polymer critical size M_e, the total energy scales like $M^{1+\alpha} g^2$, with $\alpha = 0.47 \pm 0.02$ for $\lambda = 3$ and $\alpha = 0.66 \pm 0.01$ for $\lambda = 6$, whereas above M_e, we return to the $\langle E \rangle \sim M^1 g^2$ scaling law. We get $M_e \approx 24 \pm 2$ and 70 ± 3 for $\lambda = 3$ and 6 respectively. These values correspond approximatively to $R_0 \approx \lambda$. In the first regime, small chains tend to fit into a single region where the tube renewal time is dictated by the time required to escape the region. For larger chains, the polymer has to exit through many regions before it can renew its entire tube. Note that the value of M_e will increase with the size λ of the local traps as shown in Figure 4.12.

Similarly, plotting $\Delta E / g$ against M for different values of g results into a single curve (Figure 4.13). For the standard deviation, we found $\Delta E \sim g M^{0.486 \pm 0.002}$ for all values of

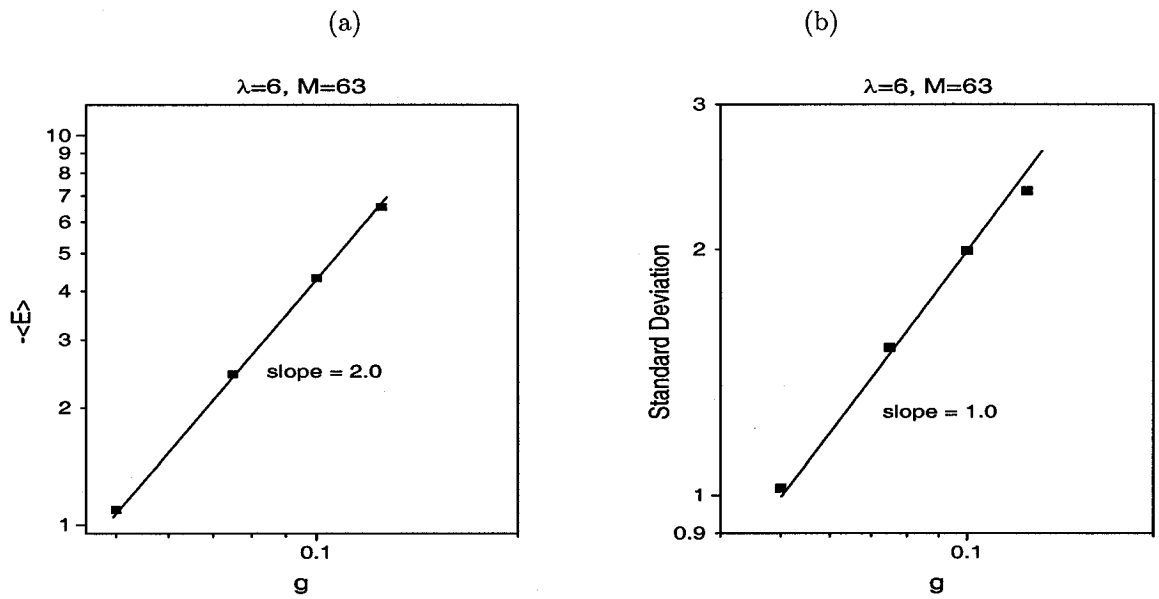

Figure 4.11: (a) Mean value of the total energy $\langle E \rangle$ of a polymer vs. g for $M = 63$. (b) Standard deviation ΔE of the total energy of the same polymer vs. g.

M when $\lambda = 1$, i.e., roughly $\Delta E \sim M^{1/2} g$. Again, we observe two different regimes when $\lambda > 1$ with a transition around M_e. Below M_e, $\Delta E \sim g M^{0.5+\gamma}$ with $\gamma = 0.27 \pm 0.02$ and 0.41 ± 0.01 for $\lambda = 3$ and 6 respectively. For larger chains ($M > M_e$), we return to the $\Delta E \sim g M^{1/2}$ scaling law. We get $M_e \approx 28 \pm 2$ and 68 ± 3 for $\lambda = 3$ and 6 respectively. These values correspond approximatively to the one obtained earlier for the mean energy. The value of M_e will increase with the size of the local traps or with λ (see Figure 4.13).

For instance, the total energy of a chain for $\lambda = 6$ follows a Gaussian distribution function defined by

$$\begin{aligned} w(E) &= \frac{1}{\sqrt{2\pi}(M^{0.75} g)} exp\left[-\frac{(E+(1.4 M^{1.4} g^{2.0}))^2}{2(M^{0.75} g)^2}\right], \qquad M < M_e \\ &= \frac{1}{\sqrt{2\pi}(2.8 M^{0.5} g)} exp\left[-\frac{(E+(8.0 M^{1.0} g^{2.0}))^2}{2(2.8 M^{0.5} g)^2}\right], \quad M > M_e \ . \end{aligned} \tag{4.12}$$

We tested Eq. 4.12 in Figure 4.14 for M=630, g=0.05 and M=10, g=0.10 with $\lambda = 6$. Similar results were obtained for $\lambda = 1$ (in which case $M_e = 1$) and 3. The next section provides detailed information about the influence of an electric field on polymer dynamics, with and without the presence of local interactions.

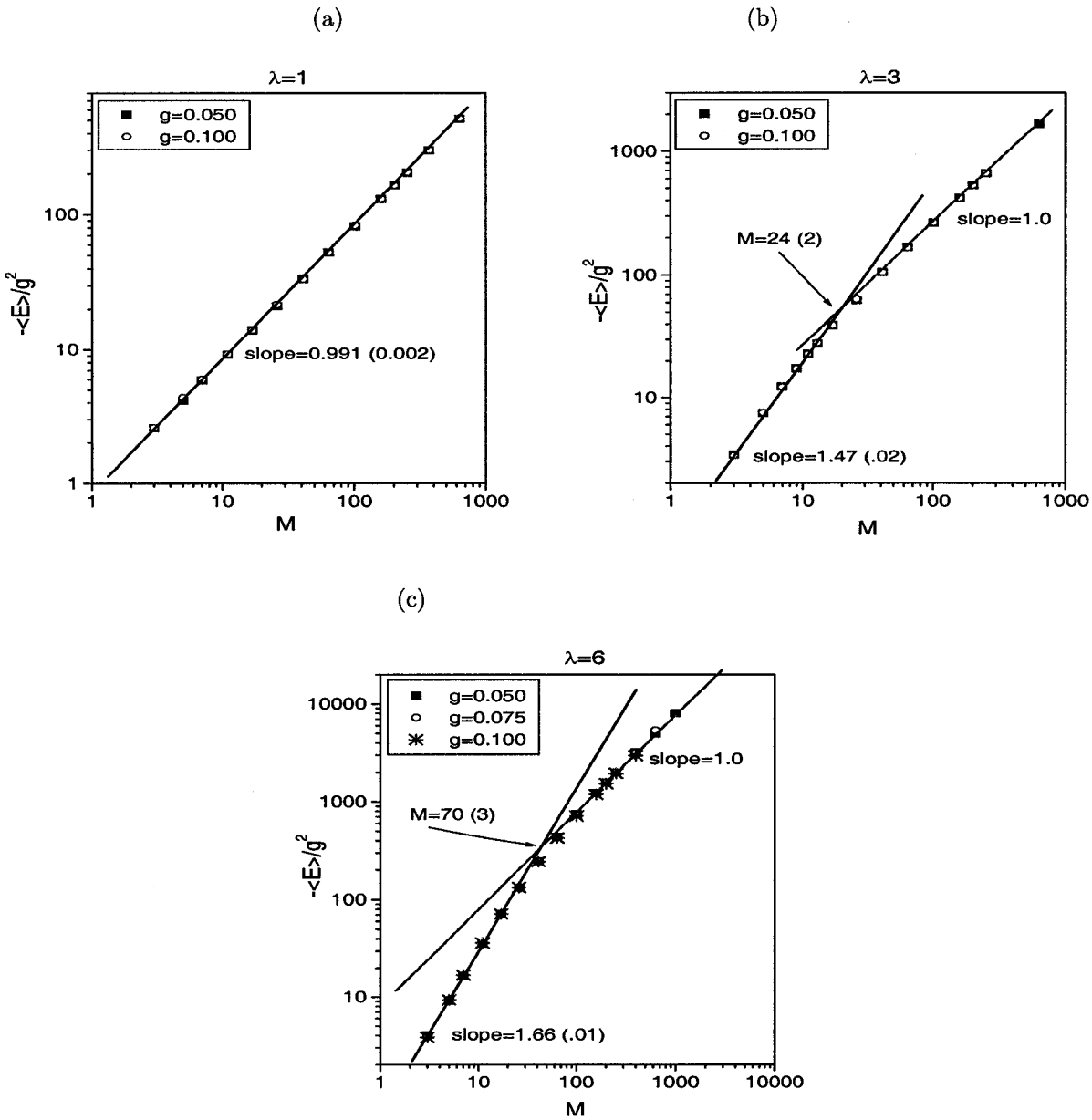

Figure 4.12: Ratio $-\langle E\rangle/g^{2.0}$ vs. M for $\lambda = 1, 3$ and 6.

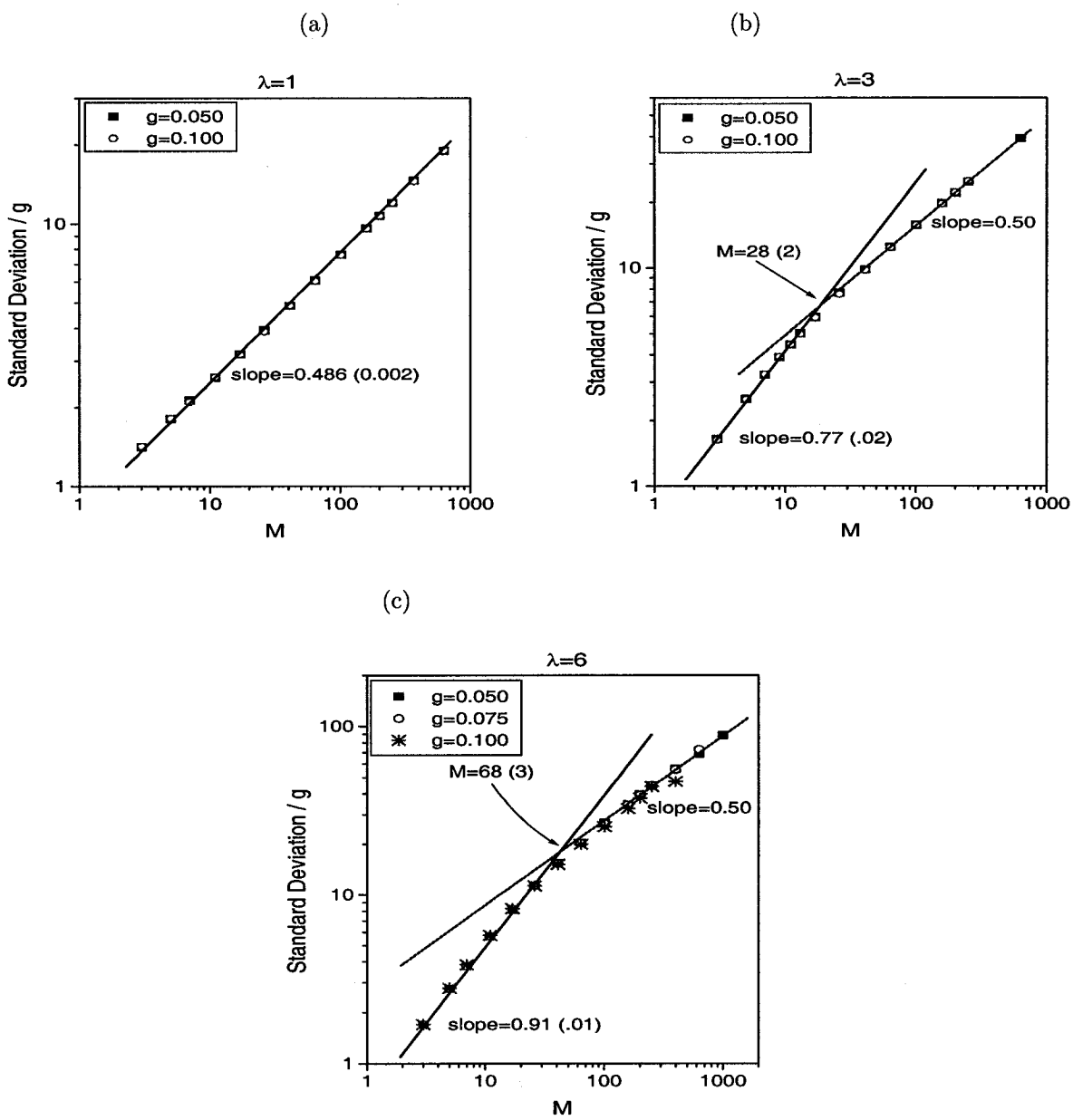

Figure 4.13: Ratio $\Delta E/g$ vs. M for $\lambda = 1, 3$ and 6.

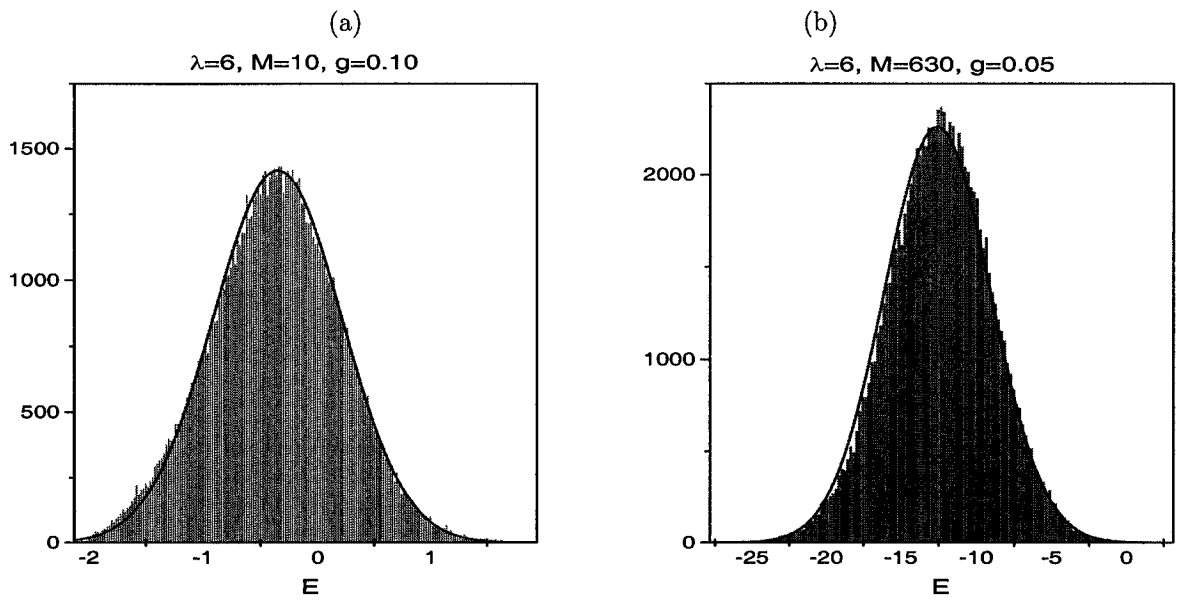

Figure 4.14: Gaussian fit of two total energy distribution functions.

4.5.3 $\epsilon > 0$ *without Local Interactions* ($g = 0$)

Figure 4.15 (a) shows a log-log plot of the diffusion coefficient $D_{g=0}(\epsilon)$ in the direction of the electric field (x-axis) vs. the size M of the polymer for different field intensities ϵ. Figure 4.15 (b) shows the relative diffusion coefficient over the scaled electric field $D_{g=0}(\epsilon)/(\epsilon\, D_0)$ where D_0 is the diffusion coefficient for $\epsilon = 0$ and $g = 0$ as a function of the polymer size M. Note that the correlation length is set to $\lambda = 6$ unless otherwise stated.

In order to understand the diffusion results, we must keep in mind that in the presence of an external field, diffusion is due to a combination of different mechanisms. For small chains, the electric forces are negligible and the diffusion process is mainly due to thermal motion, or $D_{g=0} \sim M^{-9/5}\epsilon^0$ (see Figures 4.15 (a) and 4.15 (b)). For larger chains (or high field intensities), the longitudinal velocity along the tube axis dominates and the BRM predicts $D_{g=0} \sim M^{-1/5}\epsilon^1$. Our results show that for large chains or high electric fields, the diffusion coefficient follows the scaling $D_{g=0} \sim M^{-0.53}\epsilon^1$ (Figure 4.15), in disagreement with the previous statement. The main reason for the discrepancy is found in the mean square end-to-end distances. As shown in Figure 4.16, $\langle h_x^2 \rangle$ follows the $M^{6/5}$ scaling law predicted for the self-avoiding walk model for small chains. For larger chains however, the

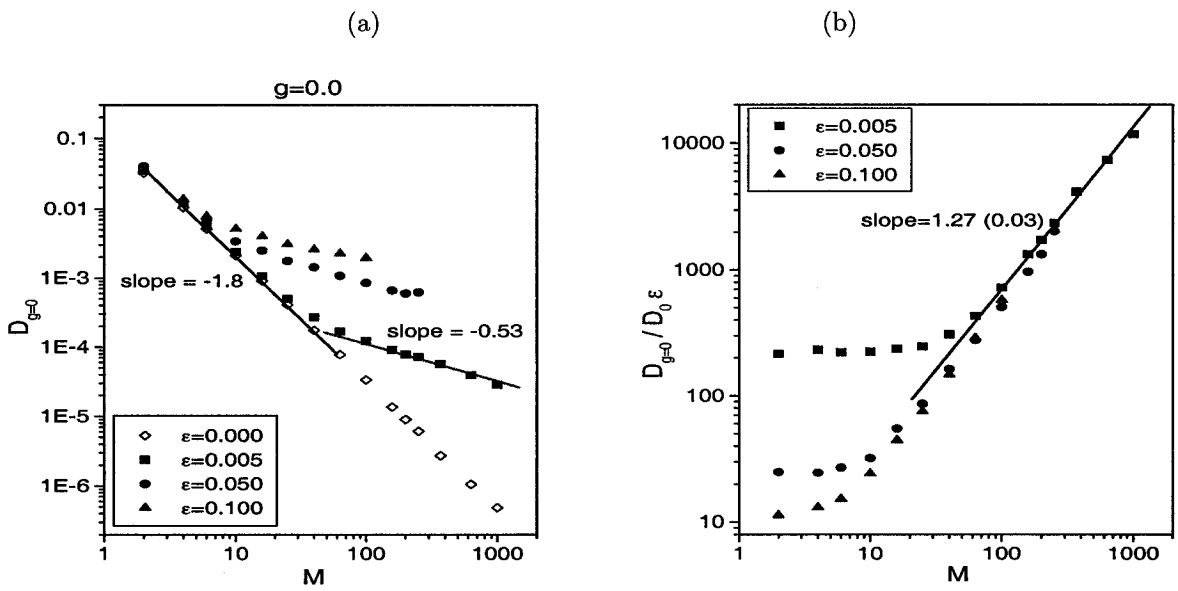

Figure 4.15: (a) Diffusion coefficient vs. M for various values of ϵ. The same data is presented in figure (b) into a different format.

scaling law changes to $M^{0.927\pm0.002}$, as if excluded volume interactions were screened.

The change in the power law is due to the time required to perform a jump in the presence of the electric field and to the excluded volume interactions. We have seen in Chapter 3 that the mean first-passage time required to jump over a distance $\bar{a}$ in the direction of the electric field was given by $t_+ = \tau_B tanh(\delta)/\delta$. The time t_+ reaches its maximum value (τ_B) when $\delta = 0$ (the polymer is in a compact conformation) and decreases for $|\delta| > 0$ (the polymer conformation is more elongated). In other words, stretched conformations have a very small jumping time while more compressed polymers have a longer jumping time. Furthermore, during the tube renewal process, if the new tube segment is already occupied by the chain itself, the simulation time is incremented and the polymer stays in the former conformation. This effect is entirely due to excluded volume interactions and reveals itself more frequently when the polymer is in a compact conformation. The combination of both these effects puts more weight on the compressed conformations (h_x small) leading to smaller mean end-to-end distances. Using the new scaling law for the mean square end-to-end distance in Eq. 4.1 leads to a diffusion coefficient scaling law $D \sim M^{-0.473}\epsilon^1$, in better

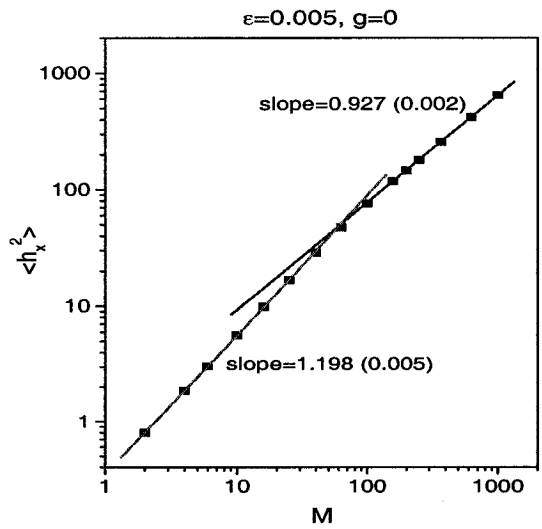

Figure 4.16: The mean square end-to-end distance vs. molecular size for $\epsilon = 0.005$. Similar results were obtained for other values of ϵ.

agreement with our simulation results.

Notice that we were unable to obtain good results for large chains. During the course of the simulation, a large polymer eventually finds itself into an elongated conformation ($h_x \gg 0$) where most of the possible jumping sites are already occupied (see Figure 4.17). Such a conformation gives a bias $\delta \gg 0$ which makes the probability of jumping in the direction of the electric field close to 1. In this case, however, the polymer stays in this conformation for very long times and a steady state is very hard to reach. Figure 4.17 shows a two dimensional representation of such conformation where h_x=13. For an electric field intensity of $\epsilon = 0.10$, the probability of jumping towards the direction of the electric field is $p_+ \cong 97\%$ (using Eq. 3.1) and the resulting state is thus metastable.

Figure 4.18 shows a logarithmic plot of the electrophoretic velocity $V_{g=0}$ in the direction of the electric field (x-axis) vs. the size of the polymer M for $g = 0$ and $\epsilon = 0.005$, 0.05 and 0.10. For small chains, we recover the $V \sim M^{-4/5}$ scaling law derived earlier. For larger chains, the electrophoretic velocity decreases more rapidly than predicted, $V_{g=0} \sim M^{-1}$. Since the velocity V is simply defined as the ratio of the mean tube length in the direction

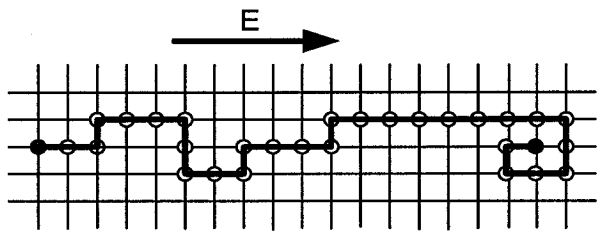

Figure 4.17: Two dimensional representation of a polymer with a metastable self-trapping conformation.

of the electric field and the mean tube renewal time, the reduction in h_x discussed earlier accounts for the faster decrease for larger chains.

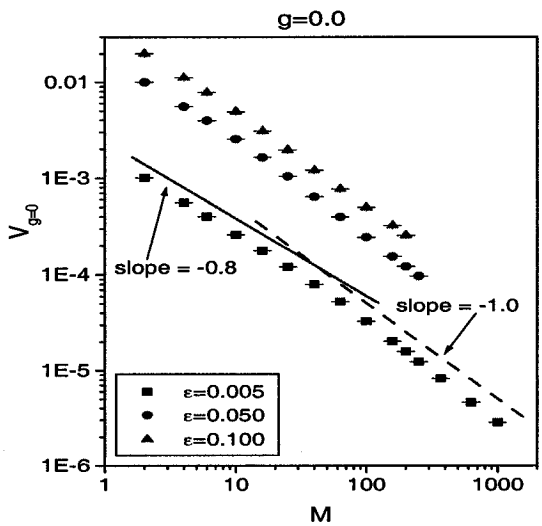

Figure 4.18: The electrophoretic velocity vs molecular size M for various values of ϵ.

4.5.4 $\epsilon > 0$ with Local Interactions ($g > 0$)

Figure 4.19 shows the diffusion coefficient D_g vs. M for ϵ=0.005 and 0.05 where the interaction parameter varies from $0 \leq g \leq 0.25$. For small chains, the thermal motion

dominates and we recover the case where $g = 0$, that is, the diffusion coefficient of small chains follows the power law $D \sim M^{-9/5}$ (see Figure 4.15). For low fields and intermediate polymer sizes, we observe two regimes. Firstly, the diffusion coefficient decreases faster than the predicted power law $D \sim M^{-9/5}$; in the limit where $\epsilon \to 0$, we should recover the results of section 4.5.2. Secondly, when the electric forces become larger than the local energies, the atypically deep traps play an important role whereby if some polymer chains get into regions of low energy, the others will migrate away, hence increasing the dispersion. In this regime, the diffusion coefficient actually exceeds the standard diffusion D_0. These results are very different from those of Zimm and Lumpkin where the diffusion coefficient decreases exponentially. For larger chains or high fields, the electric forces overcome the local interactions and we again recover the $g = 0$ limit.

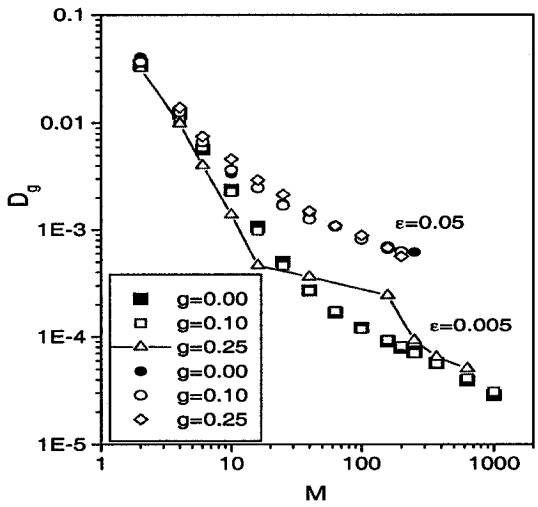

Figure 4.19: The diffusion coefficient vs. molecular size for various values of g and ϵ.

Figure 4.20 shows the electrophoretic velocity V_g vs. M for ϵ=0.005 and 0.05 where the interaction parameter varies from $0 \leq g \leq 0.25$. Again we found that it is only for low field intensities that intermediate polymer sizes are affected by the presence of local interactions. This is consistent with the results found by Zimm and Lumpkin [61]. These

authors claim that the reduction in the electrophoretic mobility is due to the occurrence of traps along the migration path. At higher field intensities or for larger chains, the electric forces overcome the local energy interactions and we recover the case $\epsilon > 0$ and $g = 0$. Note that the ϵ=0.005 and g=0.25 case is the most interesting one for both V_g and D_g.

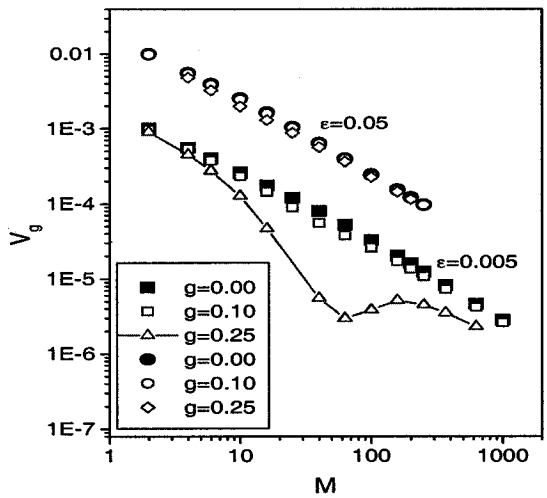

Figure 4.20: The electrophoretic velocity vs. molecular size for various values of g and ϵ.

Interestingly, we get the following scaling laws for large chains ,

$$\begin{aligned} V_g &\sim \frac{\epsilon}{M} \\ D_g &\sim \frac{\epsilon}{\sqrt{M}}, \end{aligned} \tag{4.13}$$

a result similar to the one predicted by the BRM for the electrophoresis of polyelectrolytes without excluded volume interactions (refer to Eqs. 3.6 and 3.8). Note that for the $\epsilon \to 0$ limit, we should recover the results of the previous section ($g > 0$ and $\epsilon = 0$).

4.6 Discussion

In this Chapter, we modified the mathematical model introduced in Chapter 3 for the diffusion of polymers and polyelectrolytes in irregular matrices. The simulation is carried

out inside a pre-defined matrix (quenched system) where local energies are correlated over a distance of 2λ. The matrix also introduces excluded volume effects on the polymers. The subtle memory effects that are due to the reptation dynamics in the presence of local interactions are taken into account, since each random jump is carried over a distance $\bar{a}$. This new model is very different from the one proposed by ZL [61] where the chain hops over length scales comparable to the chain's end-to-end distance h_x. This could be a realistic model to help study the effect of gel concentration inhomogeneities on polymer diffusion. The limitations of our model are: 1) for large values of g, the escape time (time required to exit from local traps) can be excessively long; and 2) in the presence of an electric field, the polymer can find itself in a conformation where most of its jumps will be rejected for very long period of times.

In the absence of a field, our results predict a small decrease of the relative mean square radius of gyration which plateaus at $M \cong (\lambda/\bar{a})^3$. Small polymers tend to fit entirely into a single region of low energy. When increasing the energy parameter g, we increase the depth of the traps and the polymer escape time (the chain stays longer in a compact conformation). When we increase the correlation length 2λ, we also increase the size M_e of the polymer that can fit into a single trap. All these effects affect the radius of gyration of polymer chains with sizes $M < M_e(\lambda)$. We have also looked at the diffusion coefficient. In this case, we noticed an increased of the molecular-size dependence of the diffusion coefficient. The local energies lead to longer tube disengagement times, thus changing the scaling law from $D \sim 1/M^{9/5}$ to $D \sim 1/M^{9/5+\alpha}$, with $\alpha > 0$. Another interesting parameter studied was the change in the total chain energy. We observed that the total energy of the chain followed the scaling law $E \sim M^1 g^2$ for large molecular sizes and for all values of λ. In this case, the polymer chain occupies many regions of different energies.

In the presence of an electric field, the situation can become quite complicated. For low fields and low molecular sizes, we simply have $D_{g=0} \sim M^{-9/5}$ and $V_{g=0} \sim M^{-4/5}$, in agreement with the BRM predictions. For high fields or larger chains, both the diffusion coefficient and the electrophoretic velocity diverge from the BRM predictions, i.e., $D_{g=0} \sim M^{-0.53}$ and $V_{g=0} \sim M^{-1.0}$. This is mainly due to the mean square end-to-end distance which becomes more compressed for larger chains ($\langle h_x^2 \rangle \sim M^{0.927}$) due to the electric field and excluded volume effects. When $g > 0$, the electrophoretic velocity shows the $g = 0$

scaling law $M^{-4/5}$ for small M, is markedly depressed for intermediate sizes, and returns to the $g = 0$ scaling law again for large M. At sufficiently high fields, the velocity follows the $g = 0$ scaling for all values of M. The depression at intermediate sizes can make the electrophoretic velocity depends very steeply on sizes over a narrow range of molecular sizes M and can produce band inversion where large chains move faster than smaller ones. The slope of the dependence of velocity on size is steepened on the low side of the depression. This initial steepening could explain some of the high slopes seen by Calladine et al. [51] and by Arvanitidou and Hoagland [116]. This is similar to the results obtained by ZL where intermediate chains showed very large mobility inversions. Similarly, the dependence of the diffusion coefficient on chain size M differs from the $g = 0$ scaling laws only for intermediate chains where the diffusion constant exceeds the standard D_0 values. This is quite different from ZL who predicted an exponential decrease of the relative diffusion coefficient in the low-field limit.

In conclusion, we have presented a study of the static and dynamic properties of polymer chains in the presence of correlated energy interactions. The algorithm can be adapted to study gel electrophoresis of polyelectrolytes in irregular matrices with different correlation lengths or the reptation of polymers in narrow and large pores. The rather generic algorithm developed and provided in this thesis provide a good foundation for the study of gel electrophoresis.

Chapter 5 Conclusion

This thesis presented a theoretical study of the flow-induced deformation of a tethered polymer chain in a nanochannel using Molecular Dynamics simulations, as well as the reptation dynamics of polymers in random energy landscapes (quenched and annealed) using Monte-Carlo simulations.

In Chapter 2, we presented a Molecular Dynamics study of the effect of strong lateral confinement on the properties of tethered freely-jointed and worm-like chains pulled at constant velocity along the axis of a nanochannel. The simulation algorithm used allows us to measure properties about both the polymer and the fluid. We found that a single universal function can describe the relation between the average drag force F_x and the fractional chain extension H, independent of the degree of confinement, the velocity or the chain length. However, we obtained $1-H \sim F_x^{-q}$ for large extensions where $q = 0.6$ for the FJC (a result that does not agree with current theories which predict $q = 1$) and $q = 0.5$ for the WLC (in agreement with theory). When we reduced the bending potential from our WLC ($k_{wlc} = 10$) to that of a FJC ($k_{wlc} = 0$), the exponent q slowly increased from $q = 0.5$ to $q = 0.6$. Note that our MD algorithm did recover the proper FJC and WLC predictions when a constant force was applied at both ends of the chain. One possible explanation for the value of q obtained for a FJC is the effect of the impact of the polymer on the flow, i.e., the free-draining nature of the polymer. A self-consistent model of FJC stretching in a flow is thus needed. The Ladoux et al. [37] results clearly show that non-uniform flows can explain a lower q exponent for FJC. Finally, we examined the coupling between the fluctuations of the drag force and the molecular extension, and we demonstrated that there is a time delay between these fluctuations. The possibility of a retardation between the drag force and the polymer extension is not something which the Oseen tensor can take into account. Therefore, modelling of high frequency (non steady-state) phenomena would certainly require MD simulations.

It is easy to modify the MD algorithm described in Chapter 2 to study a wide range of related problems, such as the deformation of a polymer pulled with a constant force. The interactions between the polymer and the solvent or the wall can be modified. Similarly, polymeric solvents or/and branched probe polymers would be of great interest.

In Chapter 3, we compared two models of gel electrophoresis in an irregular matrix. The first model, proposed by Zimm and Lumpkin [61], is based on the reptation model with random energy fluctuations. These authors have observed that even small interactions between the gel and the polyelectrolytes were able to influence the dynamics and have major effects on the mobility and the diffusion coefficient. The main effects observed by ZL are: 1) a reduction of the electrophoretic velocity, 2) the velocity of intermediate chains have a M^{-3} dependence compared to the M^{-1} law predicted by the standard reptation model, and 3) the diffusion coefficient decreases exponentially with polymer size M as opposed to the standard M^{-2} reptation law. Our model is also based on the biased reptation model to which we added random energy fluctuations. The main difference between our model and the one proposed by ZL are in the definition of the energy model used, and the length of the discrete jumps in the tube renewal process. Since the length of the jumps are small ($\delta x = \bar{a}$) in our model, this takes into account the key memory effects of the reptation model. This effect disappears if the distance between each jump becomes large (Zimm and Lumpkins used $\delta x \cong h_x$). For this reason, we consider our approach to be more reliable. The main effects that we have observed are: 1) a reduction of the electrophoretic velocity, 2) a decrease of the velocity of small chains as fast as $M^{-1.5}$ (compared to M^{-1}), 3) a diffusion coefficient that does not seem to be affected for small chains or low field intensities, and 4) an increase in the diffusion coefficient for high field intensities.

In Chapter 4, we used the Monte-Carlo algorithm develop in Chapter 3 to study the properties of polymers in a random energy landscape (a quenched system) with long-range correlations (λ being the correlation length). In the absence of an electric field, we observed a reduced radius of gyration and a decrease of the relative diffusion coefficient when the correlation length or the energy interaction parameter are increased. The relative radius of gyration of small chains decreases rapidly, $R_g \sim M^{1.2-\alpha}$ with $\alpha > 0$, to plateau for larger chains $M > (\lambda/\bar{a})^3$. The diffusion coefficient follows the standard power law of $D \sim 1/M^{9/5}$ for small chains and then decreases rapidly, $D \sim 1/M^{9/5+q}$ where $0 < q < 0.67$. Note that

for $\lambda \to \infty$, we should recover the BRM scaling laws. Zimm and Lumpkin predicted an exponential decrease of the relative diffusion coefficient in the low-field limit ($\epsilon \to 0$). In the presence of an electric field, the diffusion coefficient did not follow the anticipated power law $D \sim M^{-1/5}$ for $M > M_d$. Instead, we obtained a scaling law of $D \sim M^{-0.53}$. After further investigations, we showed that the discrepancy was due to the definition of the uncertainty about the position of the center-of-mass $\langle \Delta x^2 \rangle$, where $\langle \Delta x^2 \rangle \sim M^{0.927}$ for larger polymers. When we added random local interactions to the system (with a correlation length of $\lambda = 6$), the effect of trapping is strongest for intermediate sizes. The random local interactions are not effective for short chains since the time to exit a trap is then relatively small; for larger chains, however, the electric forces overwhelm the local interactions. The net result is a reduced electrophoretic velocity for intermediate chains which lead to strong band inversion. Similar results were obtained by Zimm and Lumpkin. On the other hand, these authors predicted an exponential decrease of the diffusion constant. Instead, we obtained a diffusion coefficient that follows the $g = 0$ scaling laws for small and large chains and exceeds the standard D_0 values for intermediate sizes.

The results presented in Chapter 3 and 4 agree well with available experimental data [107, 117, 118] and can potentially be used to model new gels that could improve the electrophoretic separation of macro-ions such as DNA. The algorithm can also be easily modified to study other problems related to reptation dynamics such as pulsed-field gel electrophoresis.

Appendix A Glossary of Symbols

Chapter 2	
Symbol	**Description**
$\mathbf{a}$	Particle acceleration
a_x	Distance between first monomer and phantom bead
b	Length of a polymer link (Kuhn length)
b_k	Kuhn length of a worm-like chain
$C_{F_x}^{a_x}$	Cross-correlation function between the drag force and the phantom link
$C_{F_x}^{h_x}$	Cross-correlation function between the drag force and the chain end-to-end distance
$C_{F_x}^{\lambda_x}$	Cross-correlation function between the drag force and the total chain length
D	Diffusion coefficient
D_c	Diameter of the nanochannel
d_n	Normalization distance
F	Scaled force ($= F_x b/k_B T$)
F_{tx}	Local bond tension
F_v	Force applied to the solvent particles to simulate a flow
F_x	Drag force or external force in the direction of the tube axis
$\mathbf{f}$	Force on a particle
$\mathcal{H}$	Hamiltonian
H	Scaled end-to-end distance ($= h_x/L_p$)
h_x	End-to-end distance in the direction of the tube axis
$\mathcal{K}$	Total kinetic energy
k_B	Boltzmann constant
k_F	FENE constant for U_F
k_w	Spring constant for U_w
k_{wlc}	Interaction strength for U_{wlc}
L	Size of the simulation box
L_c	Size of the cubic cell
L_p	Polymer contour length
L_{stem}	Length of the stem
L_t	Lateral span of the polymer
$L_{trumpet}$	Length of the trumpet
ℓ_p	Persistence length
M	Number of monomers forming the polymer
M_k	Number of Kuhn segments b_k in a worm-like chain
M_p	Number of monomers per blob

Chapter 2	
Symbol	**Description**
m	Particle molecular mass
m^*	Number of monomers in the trumpet when the polymer is in a "stem and flower" conformation
N	Total number of particles in a Molecular Dynamics simulation
N_c	Average number of particles per cubic cell
N_m	Number of polymers
n	Number of cubic cells in a simulation box
$\mathbf{p}$	Particle momentum
R_F	Maximum extension of a polymer link for U_F
R_g	Radius of gyration
R_p	Size of a blob in a Pincus chain
r	Distance between two particles
$\mathbf{r}$	Particle coordinates
r_c	Distance where the Lennard-Jones $\frac{\partial U_{lj}}{\partial r} = 0$
$\mathbf{r_{cm}}$	Position of the center of mass
$\mathcal{T}$	Current kinetic temperature
T	Desired thermodynamic temperature
t	Total simulation time
$\mathcal{U}$	Total potential energy
U_F	FENE potential energy
U_{lj}	Lennard-Jones potential
U_{tlj}	Truncated Lennard-Jones potential
U_w	Wall potential energy
U_{wlc}	Worm-like chain potential energy
u	Potential energy of individual particles, pairs, triplets, etc
V	Solvent flow velocity
V_{coil}	Flow velocity to deform a polymer in a coil conformation
V_s	Solvent velocity
$V_{trumpet}$	Flow velocity to deform a polymer in a trumpet conformation
$\mathbf{v}$	Particle velocity
x	Distance from the tethered end
y	Profile of the trumpet
$\dot{\gamma}$	Flow shear rate
Δr	Extension of the spring for U_w
δt, Δt	Simulation time step
ε	Lennard-Jones energy scale
ζ	Distance between two planar surfaces
η	Viscosity of the solvent
θ	Angle between two consecutive segments
θ_0	Reference angle
$cos\theta$	Local bond orientation
λ_x	Total chain length including the phantom bead $(= h_x + a_x)$
ξ	Polymer friction coefficient

Chapter 2	
Symbol	**Description**
ρ	Particle density during the Molecular Dynamic simulation
ρ_M	Monomer density along the chain
σ	Distance scaling for the Lennard-Jones potential
τ	Reduced time $(= \sigma(m/\varepsilon)^{1/2})$
τ_c	Time where the cross-correlation function is maximum

Chapter 3 and 4	
Symbol	**Description**
$A(x)$	Drift velocity function
a	Pore size
$\bar{a}$	Mean pore size of a gel
$a(x)$	Scaled drift velocity function
$B(x)$	Diffusion coefficient function
$b(x)$	Scaled diffusion coefficient function
D	Diffusion coefficient of the polymer
D_0	Diffusion coefficient of a polymer with $g = 0$ and $\epsilon = 0$
D_c	Curvilinear diffusion coefficient
D_g	Diffusion coefficient of a polymer with $g \geq 0$
$\mathbf{E}$	Electric field intensity
$\langle E \rangle$	Total energy of a chain
g	Variance of the energy gaussian distribution
g_i	Energy associated to a pore or monomer
g_{pore}	Energy associated to a pore
$g_{\pm wall}$	Energy at the $\pm$ wall
h_x	End-to-end distance
k_B	Boltzmann constant
L_p	Contour length of the polymer
M	Number of segments
M_d	Polymer size where the longitudinal velocity takes over the thermal motion
M_e	Polymer size where the total energy E changes power law
M_{max}	Polymer size where the diffusion coefficient reaches its maximum
M_{min}	Polymer size where the electrophoretic velocity reaches its minimum
M_r	Maximum number of monomers that can fit into a region of size λ^3
M^*	Polymer size where both terms in $u_\pm$ are equal
$P(\theta)$	Probability of the new tube orientation
p_k	Probability that the new tube segment occupies one of the five possible orientations
$p_\pm$, $p_{x_\pm}$	Probability for the chain to jump toward the $\pm$ end of the tube
Q	Total charge of the polyelectrolyte

Chapter 3 and 4	
Symbol	**Description**
q	Effective charge per segment
R_0	Radius of gyration of a polymer with $g = 0$ and $\epsilon = 0$
R_g	Radius of gyration of a polymer with $g \geq 0$
$\mathbf{r_{cm}}$	Position of the center of mass of the polymer
r_i	Distance between the pore and the cell corner i
$\mathbf{r_i}$	Coordinate of monomer i
T	Temperature
$\langle T \rangle$, $t_\pm$	Mean exit time
$\langle T^2 \rangle$, $t_\pm^2$	Mean square exit time
t_{ssD}	Steady-state time for the diffusion coefficient
t_{ssV}	Steady-state time for the electrophoretic velocity
$t_\pm$	Mean duration of the jumping process
U	Potential function
u	Scaled potential function
$u_\pm$	Scaled potential value at the $\pm$ wall
V	Electrophoretic velocity of the polymer
V_c	Longitudinal drift velocity
V_ℓ	Longitudinal velocity
v_c	Scaled longitudinal drift velocity
V_g	Electrophoretic velocity of a polymer with $g \geq 0$
$w(g_i)$	Energy distribution function (Gaussian)
β	Smoothness parameter for the energy landscape
ΔE	Standard deviation of the total energy of a chain
$\Delta g_\pm$	Net change of the chain's total free energy during a jump in the $\pm$ direction
$\Delta r_{i\alpha}$	Absolute distance between the pore and cell corner i in the α direction
Δt^2	Variance of the first passage time
$\Delta t_\pm^2$	Variance of the duration of the jumping process
Δx	Variance about the position of the center-of-mass
δ	Conformation-dependent bias factor
ϵ	Scaled electric field
θ	Orientation of the new tube segment
λ	Correlation length
μ	Electrophoretic mobility
ν	Flory's exponent
ξ	Curvilinear friction coefficient of a polymer
τ	Tube renewal time
τ_B	Brownian time
$\tau_\pm$	Mean time required for the chain to jump over a distance $\bar{a}$

References

[1] U.S. Departement of Health and Human Services and U.S. Department of Energy, *Understanding Our Genetic Inheritence, The U.S. Human Genome Project: The First Five Years* (1990).

[2] Sanger F., *Proc. Nat. Acad. Sci.* **74**, 5463 (1977).

[3] Swerdlow H. and Gesteland R., *Nucl. Acids Res.* **18**, 1415 (1990).

[4] Luckey J.A. et al., *Nucl. Acids Res.* **18**, 4417 (1990).

[5] Cohen A.S., Najarian D.R. and Karger B.L., *J. Chromatogr.* **516**, 49 (1990).

[6] Carrilho E. et al., *Anal. Chem.* **68**, 3305 (1996).

[7] Barron A.E., Blanch H.W. and Soane D.S., *Electrophoresis* **15**, 597 (1994).

[8] Ogston A.G., *Trans. Faraday Soc.* **54**, 1754 (1958).

[9] de Gennes P.G., *J. Chem. Phys.* **55**, 572 (1971).

[10] Hubert S.J., Slater G.W. and Viovy J.L., *Macromolecules* **29**, 1006 (1996).

[11] Keller A. and Odell J., *Colloid Polym. Sci.* **263**, 181 (1985).

[12] Narth K., Odell J. and Keller A. *J. Polym. Sci. B* **30**, 335 (1992).

[13] Adam M. and Delsanti M., *J. Phys. Paris* **37**, 1045 (1976).

[14] Adam M. and Delsanti M., *Macromolecules* **10**, 1229 (1977).

[15] Tsunashima Y., Nemoto N. and Kurata M., *Macromolecules* **16**, 584 (1983).

[16] Smith S.B. , Finzi L. and Bustamante C., *Science* **258**, 1122 (1992).

[17] Ashkin A., Dziedzic J., Bjorkholm J. and Chu S., *Opt. Lett.* **11**, 288 (1986).

[18] Perkins T.T., Quake S.R., Smith D.E. and Chu S., *Science* **264**, 822 (1994).

[19] Wirtz D., *Phys. Rev. Lett.* **75**, 2436 (1995).

[20] Bakajin O.B., Duke T.A.J., Chou C.F., Chan S.S., Austin R.H. and Cox E.C., *Phys. Rev. Lett.* **80**, 2737 (1998).

[21] Manneville S., Cluzel Ph., Viovy J.L., Chatenay D. and Caron F., *Europhys. Lett.* **36**, 413 (1996).

[22] Doyle P.S., Ladoux B. and Viovy J.L., *Phys. Rev. Lett.* **84**, 4769 (2000).

[23] Rief M., Fernandez J.M. and Gaub H.E., *Phys. Rev. Lett.* **81**, 4764 (1998).

[24] Ortiz C. and Hadziioannou G., *Macromolecules* **32**, 780 (1999).

[25] Oesterhelt F., Rief M. and Gaub H.E., *New J. of Phys.* **1**, 6.1 (1999).

[26] Sheng Y.J., Lai P.Y. and Tsao H.K. *Phys. Rev. E* **56**, 1900 (1997).

[27] Starkweather M.E., Muthukumar M. and Hoagland D.A., *Macromolecules* **31**, 5495 (1998).

[28] Starkweather M.E., Muthukumar M. and Hoagland D.A., *Macromolecules* **32**, 6837 (1999).

[29] Petera D. and Muthukumar M., *J. Chem. Phys.* **111**, 7614 (1999).

[30] Neelov I.M., Adolf D.B., Lyulin A.V. and Davies G.R., *J. Chem. Phys.* **117**, 4030 (2002).

[31] Aganwai U.S., *J. Chem. Phys.* **113**, 3397 (2000).

[32] Radzyner Y. and Rapaport D.C., *Phys. Rev. E* **57**, 5687 (1998).

[33] Pierleoni C. and Ryckaert J.P., *J. Chem. Phys.* **11**, 8539 (1992).

[34] Cheon M., Chang I., Koplik J. and Banavar J.R., *Europhys. Lett.* **58**, 215 (2002).

[35] Volkenstein M.V., *Configurational Statistics of Polymeric Chains*, Interscience, NY (1963).

[36] Marko J.F. and Siggia E.D., *Macromolecules* **28**, 8759 (1995).

[37] Ladoux B. and Doyle P.S., *Europhys. Lett.* **52**, 511 (2000).

[38] Rzehak R., Kienle D., Kawakatsu T. and Zimmermann W., *Europhys. Lett.* **46**, 821 (1999).

[39] Brochard-Wyart F., *EuroPhys. Lett.* **23**, 105 (1993).

[40] Tiselius C., *Trans. Faraday Soc.* **33**, 524 (1937).

[41] Grabar P. and Williams C.A., *Biochem. Biophys. Acta* **10**, 193 (1953).

[42] Righetti P.G., *Biochem. Biophys. Methods* **19**, 1 (1989).

[43] Righetti P.G., *Metabolism* **13**, 985 (1964).

[44] Rodbard D. and Chramback A., *Proc. Natl. Acad. Sci. USA* **4**, 970 (1970).

[45] Morris C.J., *Protides in the biological fluids*, H.Peeters, Elsevier, NY (1967).

[46] Flint D.H. and Harrington R.E., *Biochemistry* **11**, 4858 (1975).

[47] McDonnel M.W., Simon M.N. and Studier F.W., *J. Mol. Biol.* **110**, 119 (1977).

[48] Fangman W.L., *Nucleic Acids Res.* **5**, 653 (1978).

[49] Hervet H. and Bean C.P., *Biopolymers* **26**, 727 (1989).

[50] Stellwagen N.C., *Adv. Electrophoresis* **1**, 179 (1987).

[51] Calladine C.R., Collins C.M., Drew H.R. and Mott M.R., *J. Mol. Biol.* **221**, 981 (1991).

[52] Lumpkin O.J. and Zimm B.H., *Biopolymers* **21**, 2315 (1982).

[53] Lerman L.S. and Frisch H.L., *Biopolymers* **21**, 995 (1982).

[54] Lumpkin O.J., Déjardin P. and Zimm B.H., *Biopolymers* **24**, 1573 (1985).

[55] Slater G.W. and Noolandi J., *Phys. Rev. Lett.* **55**, 1579 (1985).

[56] Slater G.W. and Noolandi J., *Biopolymers* **25**, 431 (1986).

[57] Slater G.W. and Noolandi J., *Europhys. Lett.* **1**, 347 (1986).

[58] Slater G.W., Rousseau J. and Noolandi J., *Biopolymers* **26**, 863 (1987).

[59] Slater G.W., Rousseau J., Noolandi J., Turmel C. and Lalande M., *Biopolymers* **27**, 509 (1988).

[60] Noolandi J., Rousseau J., Slater G.W., Turmel C. and Lalande M. *Phys. Rev. Lett.* **58**, 2428 (1987).

[61] Zimm B.H. and Lumpkin O., *Macromolecules* **26**, 226 (1993).

[62] Calladine C.R., Collis C.M., Drew H.R. and Mott M.R., *J. Mol. Biol.* **221**, 981 (1991).

[63] Perkins T.T., Smith D.E., Larson R.G. and Chu S., *Science* **268**, 83 (1995).

[64] Brochard-Wyart F., *Europhys. Lett.* **30**, 387 (1995).

[65] Larson R.G., Perkins T.T., Smith D.E. and Chu S., *Phys. Rev. E* **55**, 1794 (1997).

[66] Zimm B.H., *Macromomecules* **31**, 6089 (1998).

[67] Stigter D. and Bustamante C., *Biophy. J.* **75**, 1197 (1998).

[68] Currie I.G., *Fundamental Mechanics of Fluids*, McGraw-Hill (1974).

[69] Kremer K. and Grest G.S., *J. Chem. Phys.* **92**, 5057 (1990).

[70] Grest G.S. and Kremer K., *Phys. Rev. A* **33**, 3628 (1986).

[71] Koplik J. , Banavar J.R. and Willemsen J.F., *Phys. Fluids A* **1**, 781 (1989)

[72] Allen M.P. and Tildesley D.J., *Computer Simulations of Liquids*, Clarendon, Oxford (1987).

[73] Ciccotti G. and Hoover W.G., *Molecular-Dynamics Simulation of Statistical Mechanics Systems*, North-Holland, Amsterdam (1986).

[74] Haile J.M., *A Primer on the Computer Simulation of Atomic Fluids by Molecular Dynamics*, Clemson Univ., Clemson, SC (1980).

[75] Verlet L., *Phys. Rev.* **159**, 98 (1967).

[76] Koplik J. , Banavar J.R. and Willemsen J.F., *Phys. Rev. Let.* **60**, 1282 (1988)

[77] Gear C.W., *Numerical Initial Value Problems in Ordinary Differential Equations*, Prentice-Hall, Englewood Cliffs, NJ (1971).

[78] Hockney R.W., *Methods Comput. Phys.* **9**, 136 (1970).

[79] Potter D., *Computational Physics*, Wiley, New York (1972).

[80] Swope W.C., Andersen H.C., Berens P.H. and Wilson K.R., *J. Chem. Phys.* **76**, 637 (1982).

[81] Lennard-Jones J.E. and Devonshire A.F., *Proc. R. Soc. Lond.* **A169**, 317 (1939).

[82] Bobetic M.V. and Barker J.A., *Phys. Rev.* **B2**, 4169 (1970).

[83] Barker J.A., Fisher R.A. and Watts R.O., *Mol. Phys.* **21**, 657 (1971).

[84] Maitland G.C. and Smith E.B., *Mol. Phys.* **22**, 861 (1971).

[85] Weeks J.D., Chandler D. and Anderson H.C., *J. Chem. Phys.* **54**, 5237 (1971).

[86] Quentrec B and Brot C., *J. Comput. Phys.* **13**, 430 (1975).

[87] Hockney R.W. and Eastwood J.W., *Computer Simulation Using Particles*, McGraw-Hill, New York (1981).

[88] Born M. and Von Karman Th., *Physik Z.* **13**, 297 (1912).

[89] Nosé S., *Mol. Phys.* **52**, 255 (1984).

[90] Hoover W.G., *Phys. Rev. A* **31**, 1695 (1985).

[91] Bird R.B., *Dynamics of Polymer Liquids*, Wiley, New York (1977).

[92] Dünweg B. and Kremer K., *J. Chem. Phys.* **99**, 6983 (1993).

[93] Dünweg B., *J. Chem. Phys.* **99**, 6977 (1993).

[94] Slater G.W., Hubert S.J. and Nixon G.I., *Macromol. Theory Simul.* **3**, 695 (1994).

[95] Pincus P., *Macromolecules* **9**, 386 (1976).

[96] Kovac J. and Crab C.C., *Macromolecules* **15**, 537 (1982).

[97] Fixman M. and Kovac J., *J. Chem. Phys.* **58**, 1564 (1973).

[98] Smith S.B., Cui Y. and Bustamante C., *Science* **271**, 795 (1996).

[99] Odjik T., *Macromolecules* **28**, 7016 (1995).

[100] Pépin M., *Unpublished.*

[101] Doi M. and Edwards S.F., *Journal of Chemical Society, Faraday Transaction II* **74**, 1789 (1978).

[102] Doi M. and Edwards S.F., *Journal of Chemical Society, Faraday Transaction II* **74**, 1802 (1978).

[103] Doi M. and Edwards S.F., *Journal of Chemical Society, Faraday Transaction II* **74**, 1818 (1978).

[104] Doi M. and Edwards S.F., *Journal of Chemical Society, Faraday Transaction II* **75**, 38 (1978).

[105] Klein J., *Nature* **271**, 143 (1978).

[106] Kremer K. and Grest G.S., *J. Chem. Phys.* **92**, 5057 (1994).

[107] Rotstein N.A. and Lodge T.P., *Macromolecules* **25**, 1316 (1992).

[108] Baumgärtner A. and Muthukumar M., *J. Chem. Phys.* **87**, 3082 (1987).

[109] Muthukumar M. and Baumgärtner A., *Macromolecules* **22**, 1937 (1989).

[110] Zimm B. H., *Electrophoresis* **17**, 996 (1996).

[111] Bouchaud J.P. and Georges A., *Phys. Rep.* **195**, 127 (1990).

[112] Prigogine I. and Rice S.A., *Advances in Chemical Physics, Polymeric Systems*, Ed. John Willey and Sons, Inc., New York (1996).

[113] Slater G.W. and Wu S.Y., *Phys. Rev. Lett.* **75**, 164 (1995).

[114] Noolandi J., Rousseau J., Slater G.W., Turmel C. and Lalande M., *Phys. Rev. Lett.* **58**, 2428 (1987).

[115] Duke T.A.J., Semenov A.N. and Viovy J.L., *Phys. Rev. Lett.* **69**, 3260 (1992).

[116] Arvanitidou E. and Hoagland D., *Phys. Rev. Lett.* **67**, 1464 (1991).

[117] Mayer P., Slater G.W. and Drouin G., *Appl. Theoret. Electrophoresis* **3**, 147 (1993).

[118] Rousseau J., Drouin G. and Slater G.W., *Phys. Rev. Lett.* **79**, 1945 (1997).

[119] Hubert S.J., *M.Sc. Thesis, Theoretical Study of Three Problems Related to the Electrophoresis of Polyelectrolytes*, University of Ottawa, Ottawa, Canada (1995).

[120] Doi M. and Edwards S.F., *The Theory of Polymer Dynamics*, Oxford University Press, NewYork (1986).

[121] Slater G.W., Rousseau J. and Noolandi J., *Biopolymer* **26**, 863 (1987).

[122] Lumpkin O., *Phys. Rev. E* **48**, 1910 (1993).

[123] Bouchaud J.P. and Georges A., *Physics Reports* **195**, 127 (1990).

[124] Slater G.W., *Electrophoresis* **14**, 1 (1993).

[125] Duke T.A.J., Viovy J.L. and Semenov A.N., *Biopolymers* **34**, 239 (1994).

[126] Semenov A.N., Duke T.A.J. and Viovy J.L., *Phys. Rev. E* **51**, 1520 (1995).